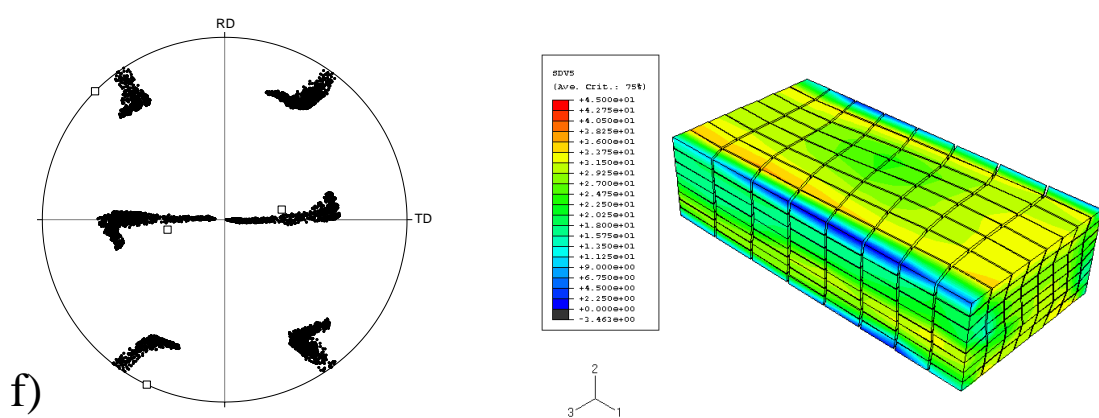
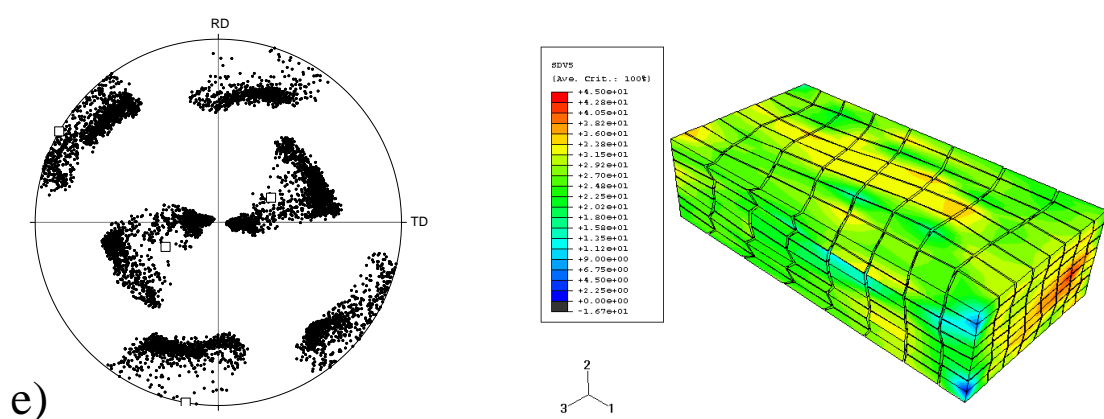
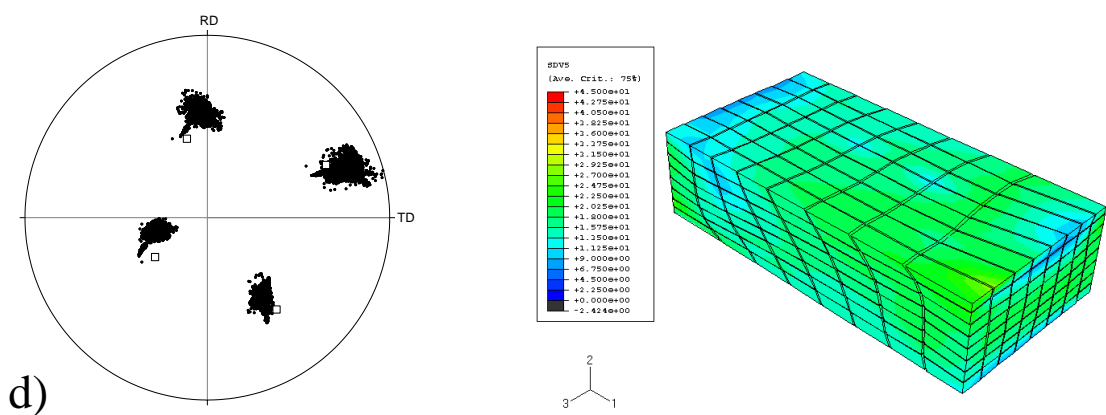


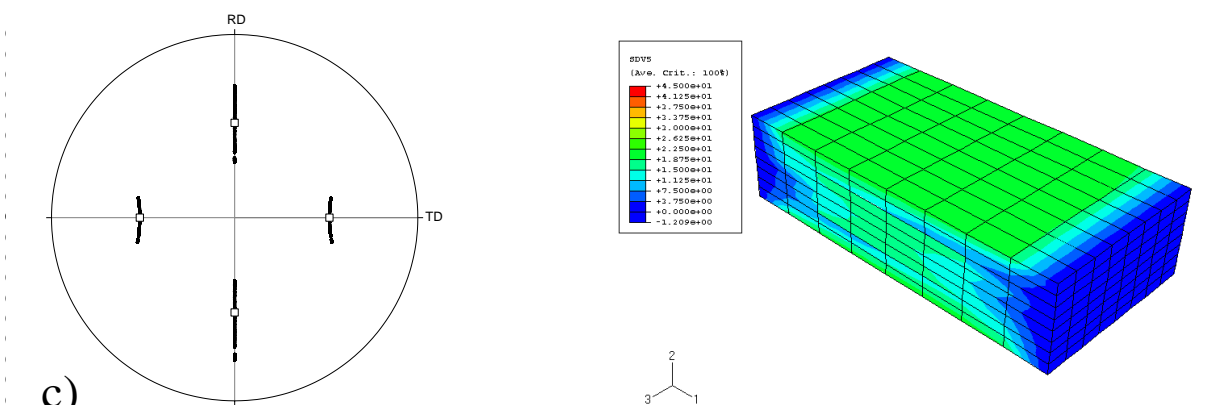
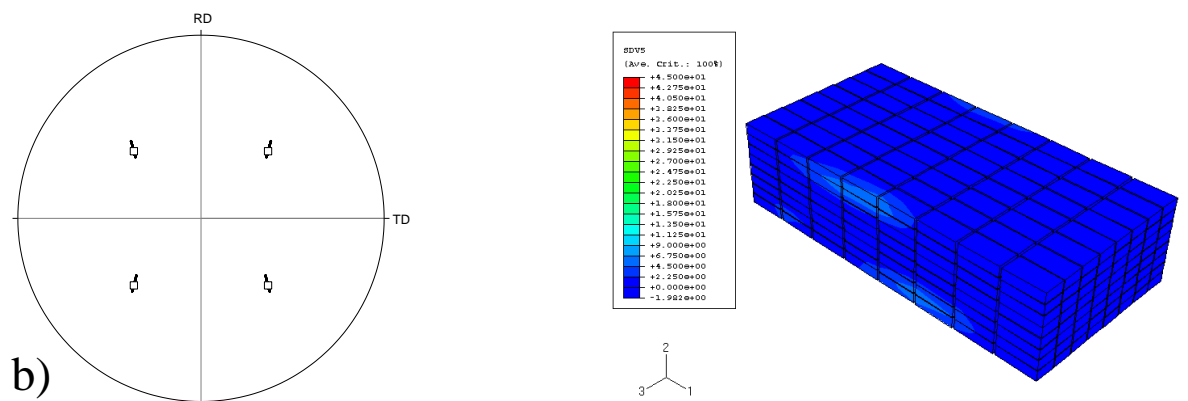
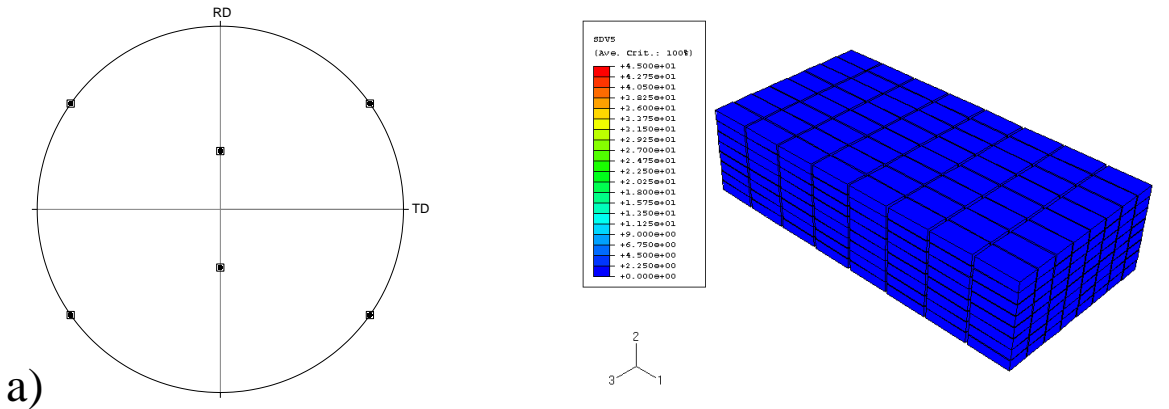
single crystals, bcc





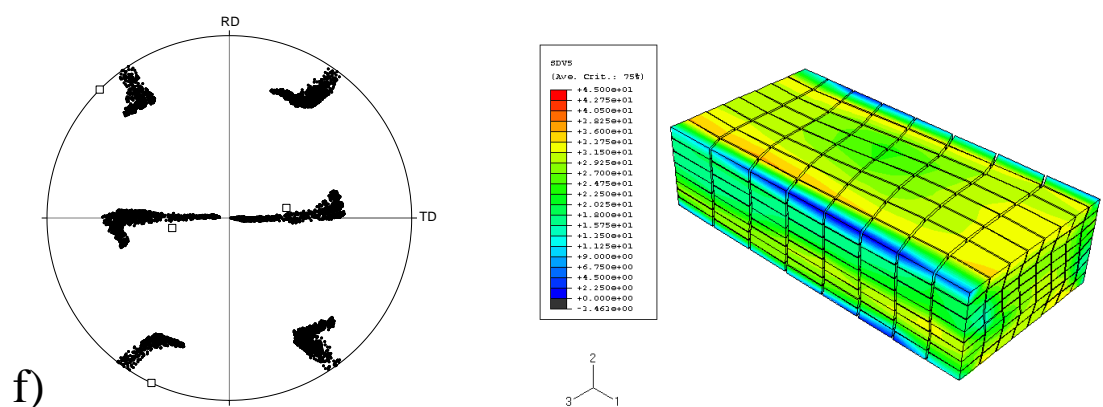
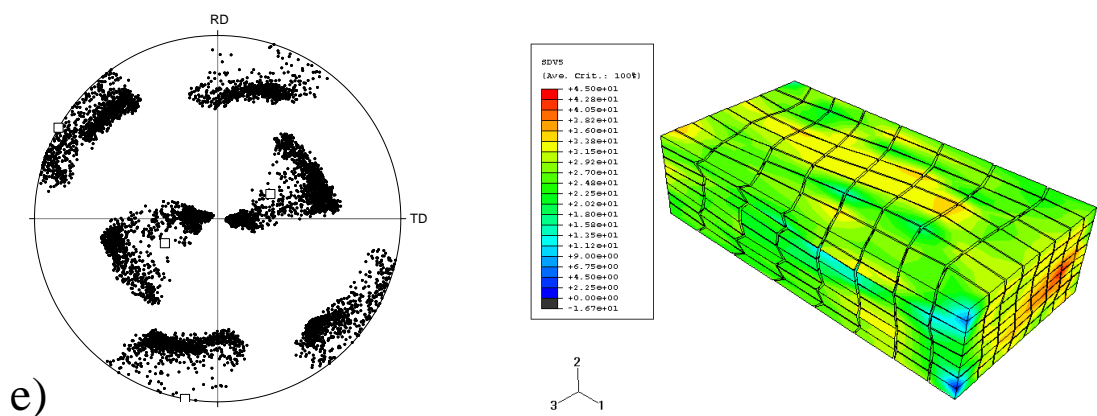
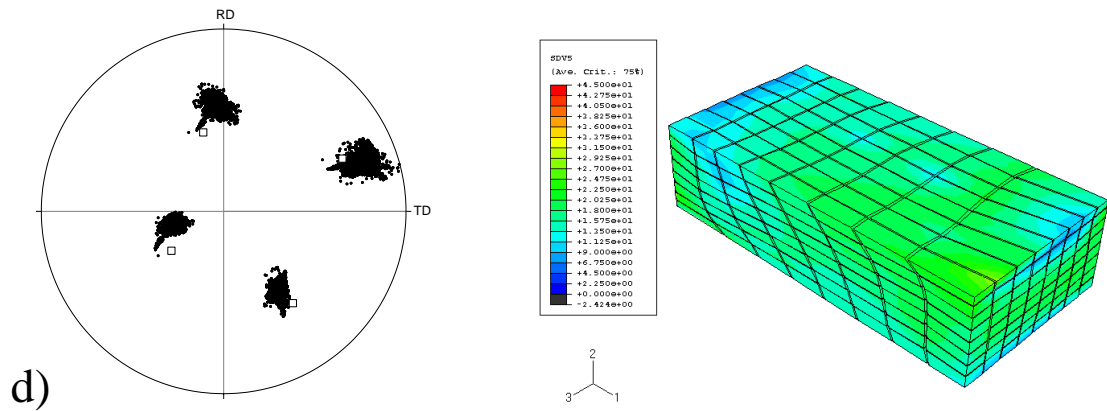
single crystals, bcc





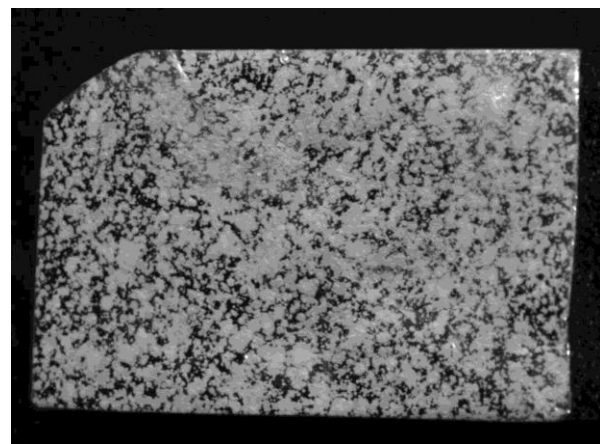
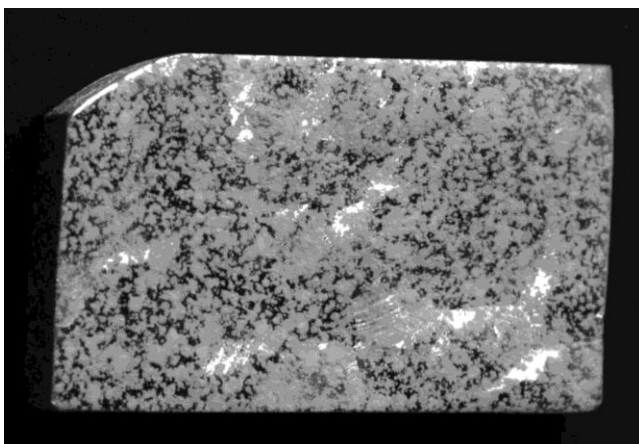
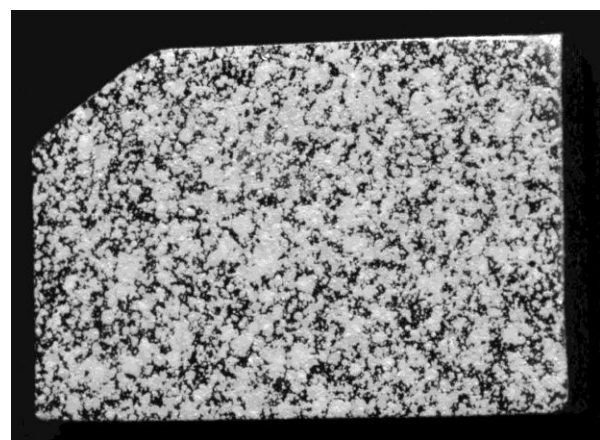
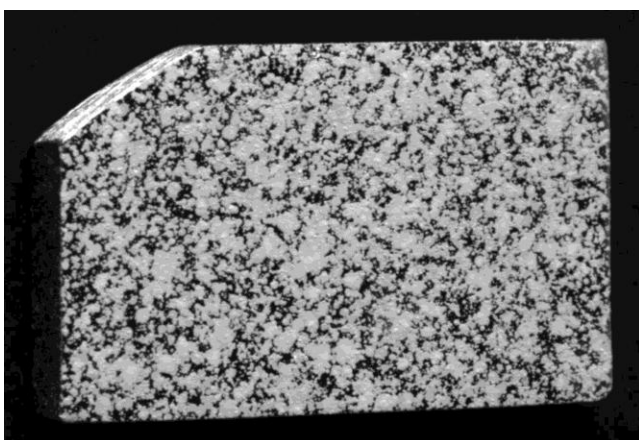
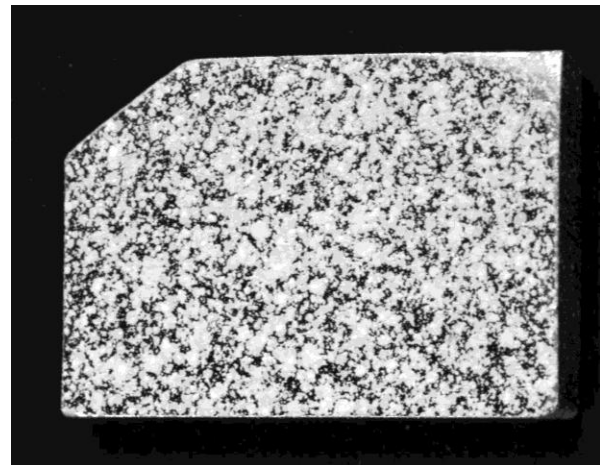
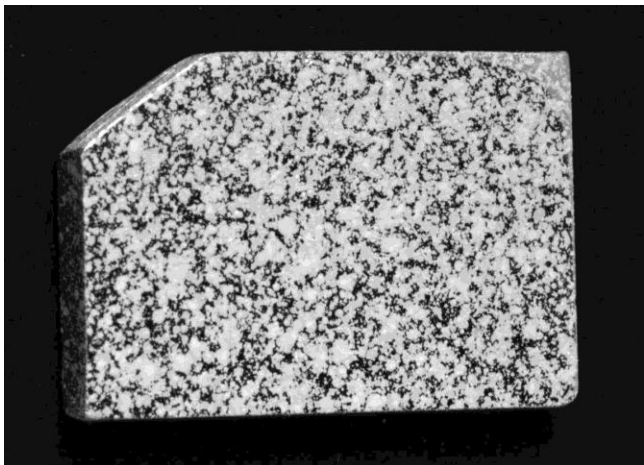
single crystals, fcc





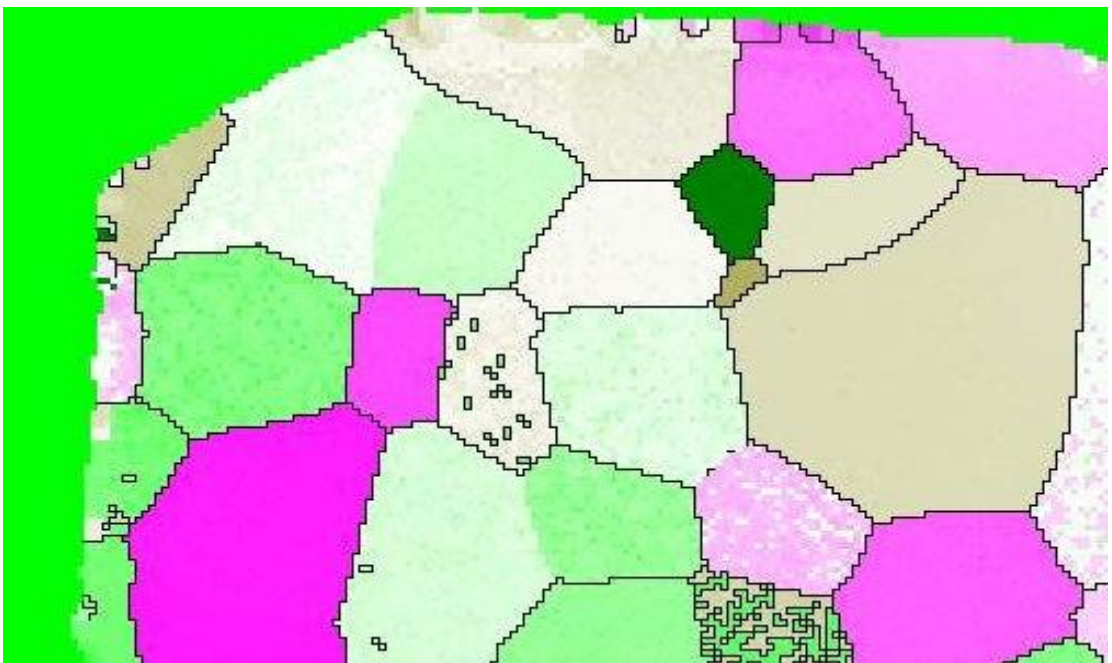
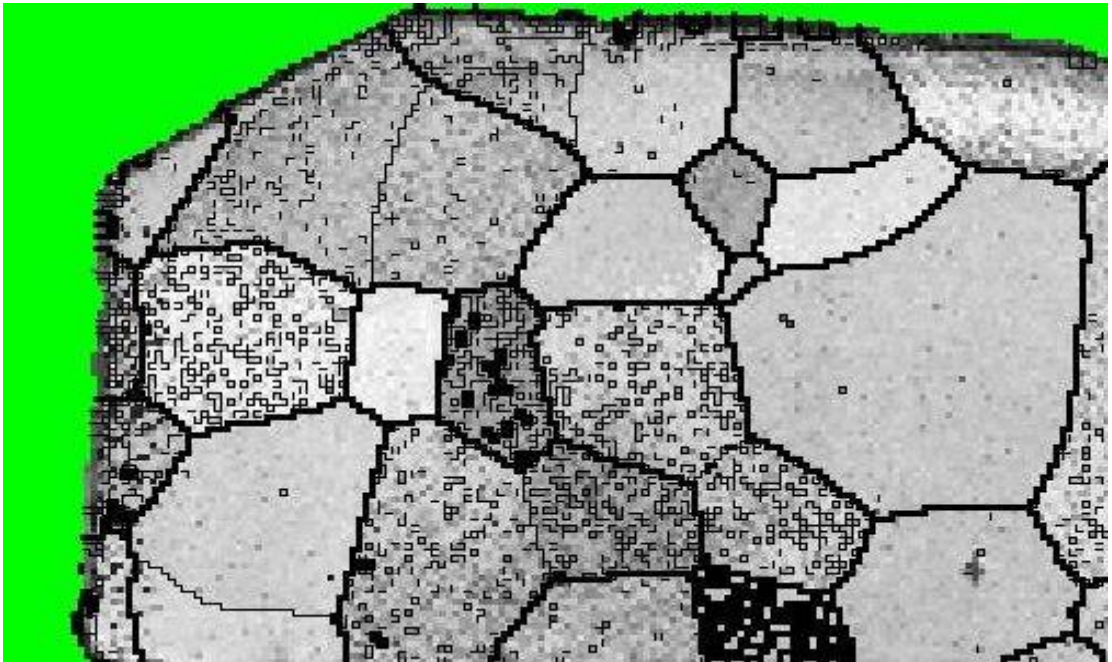
single crystals, fcc





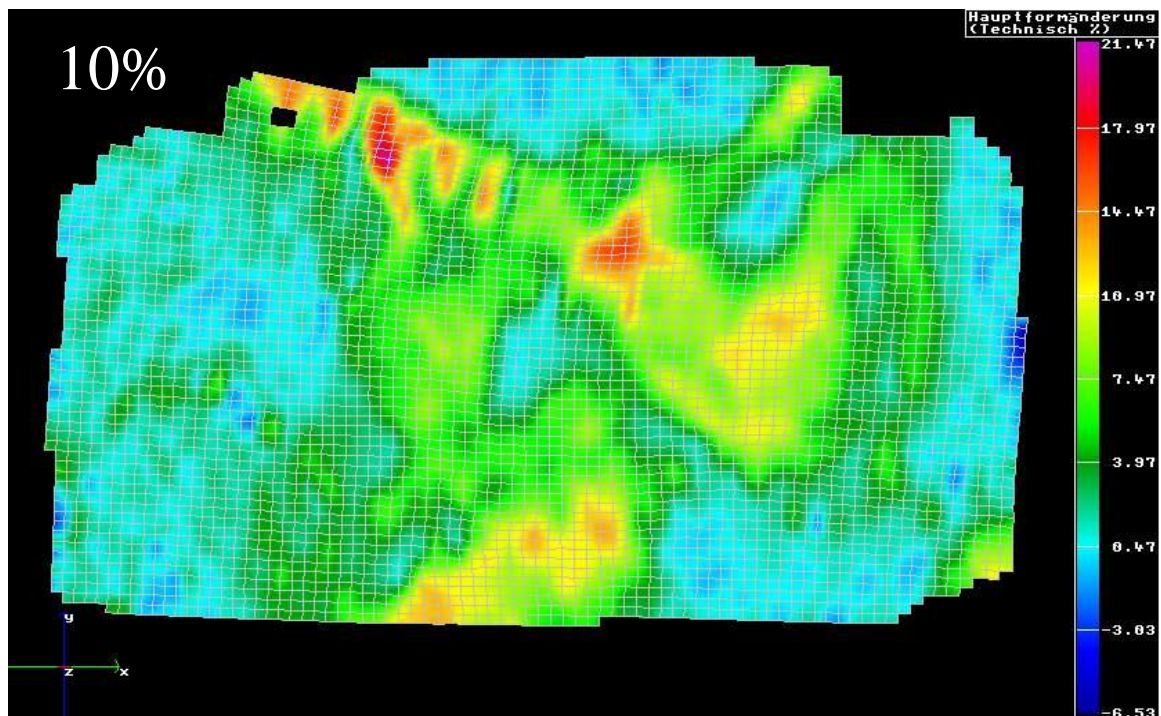
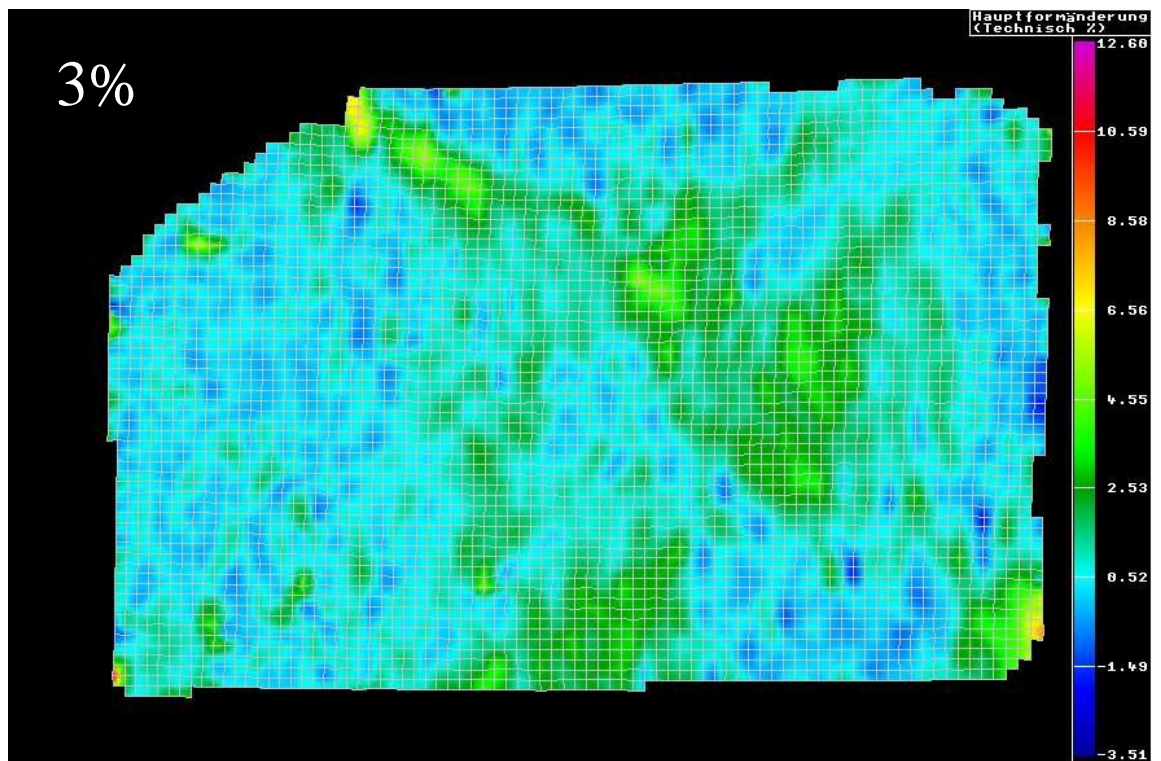
3%, 10%, 13% macroscopic strain



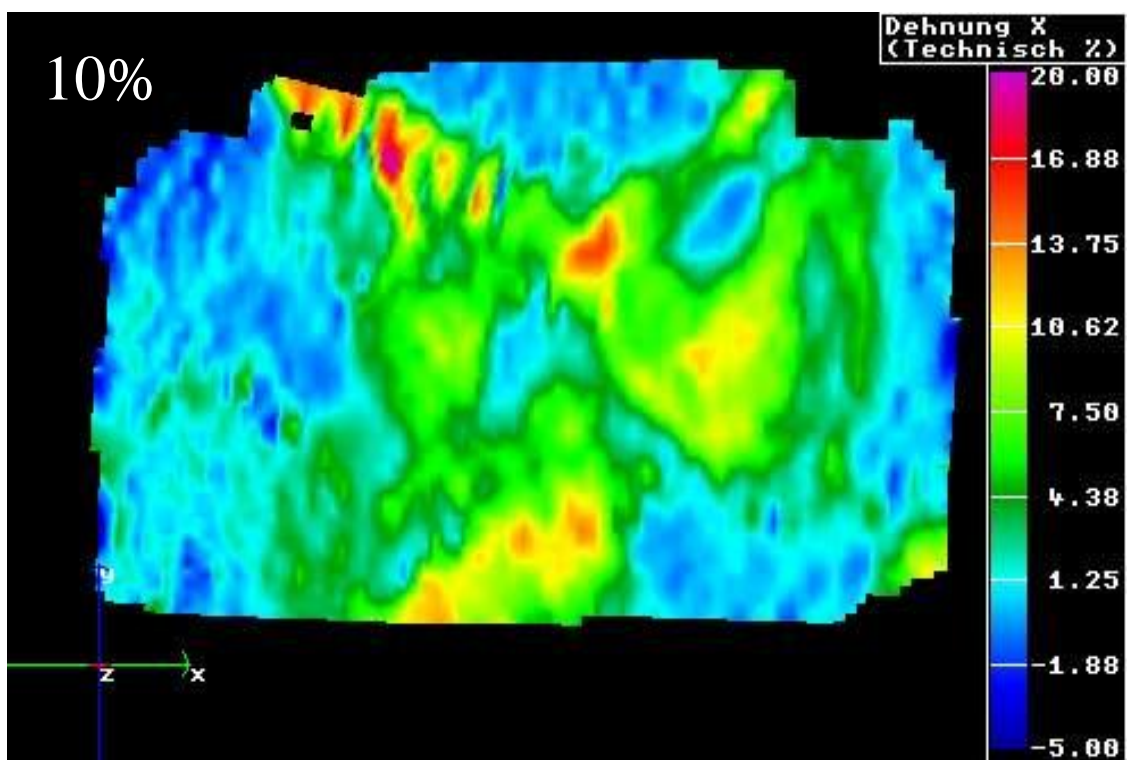
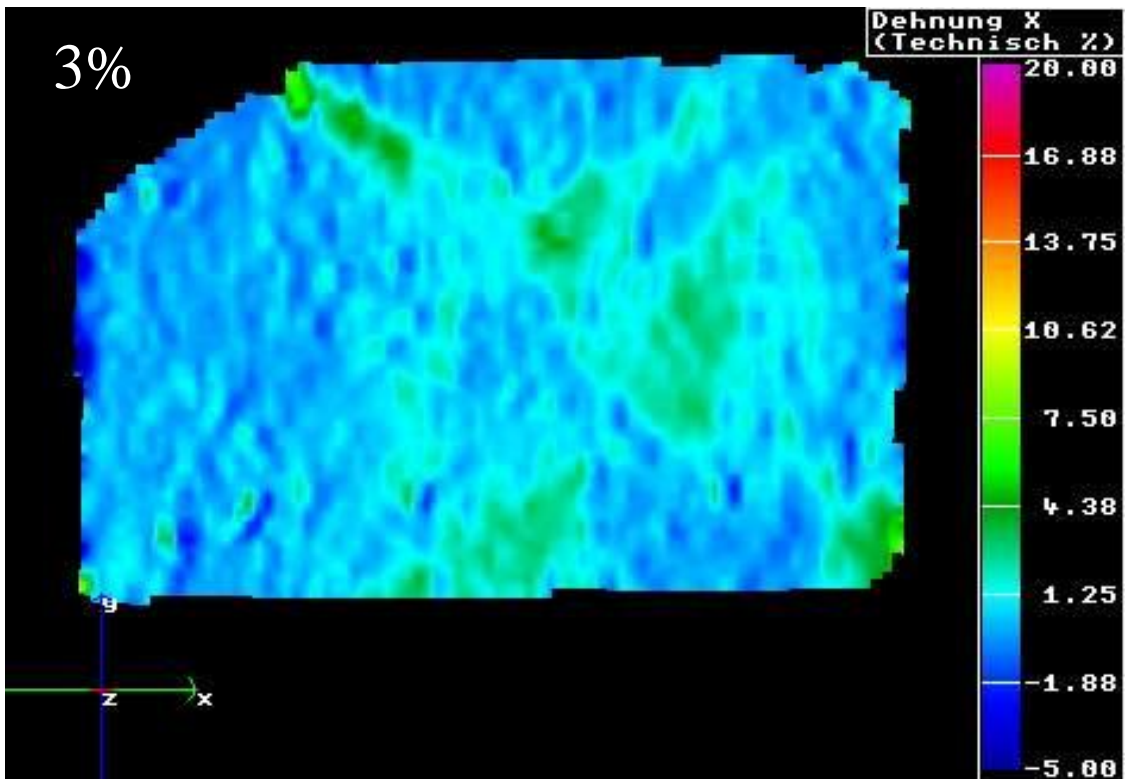


orientation mapping



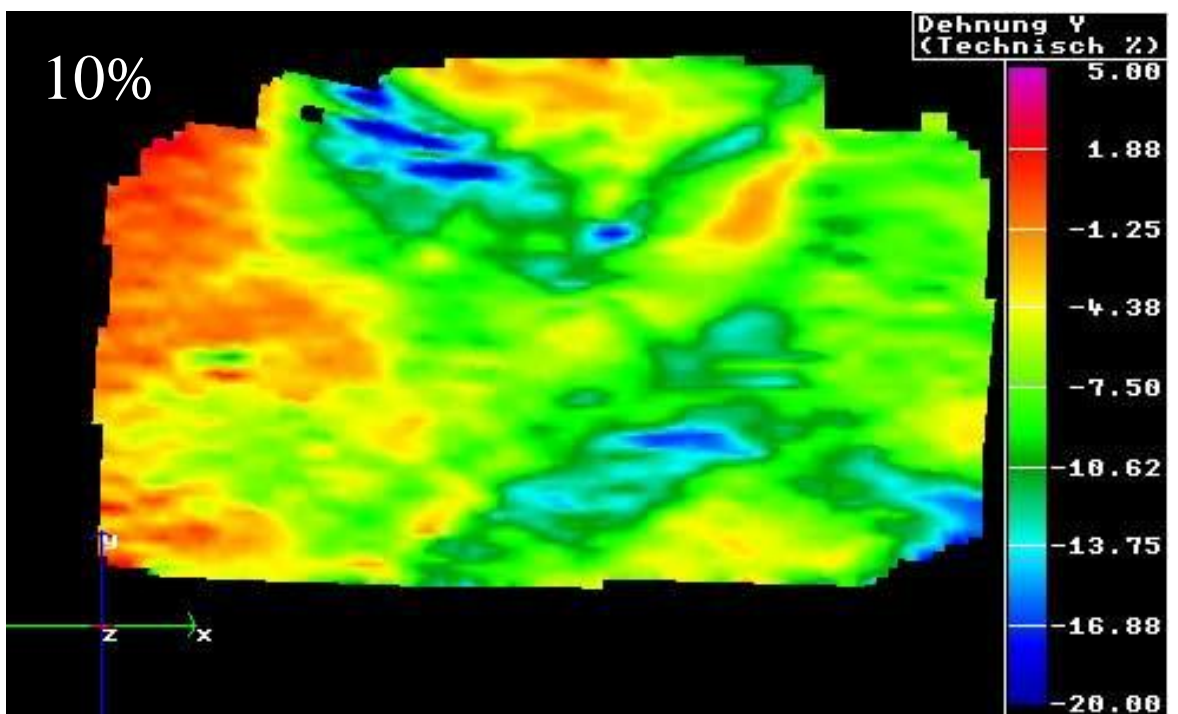
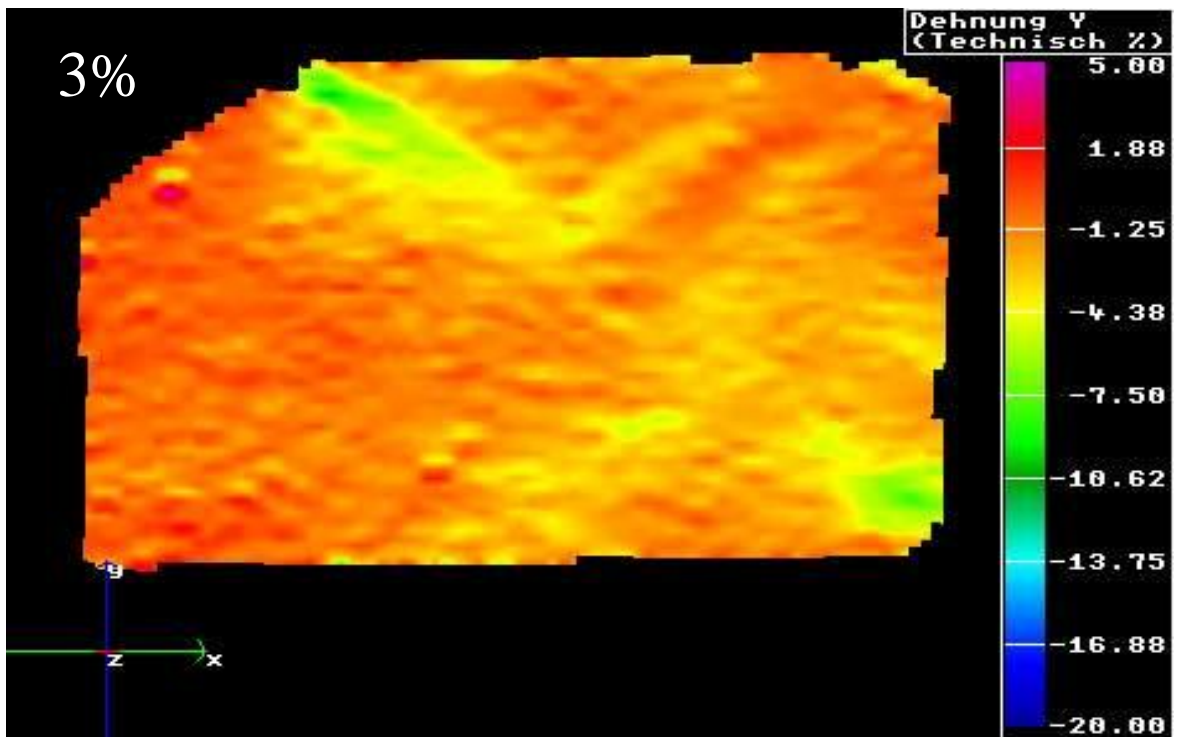


strain mapping



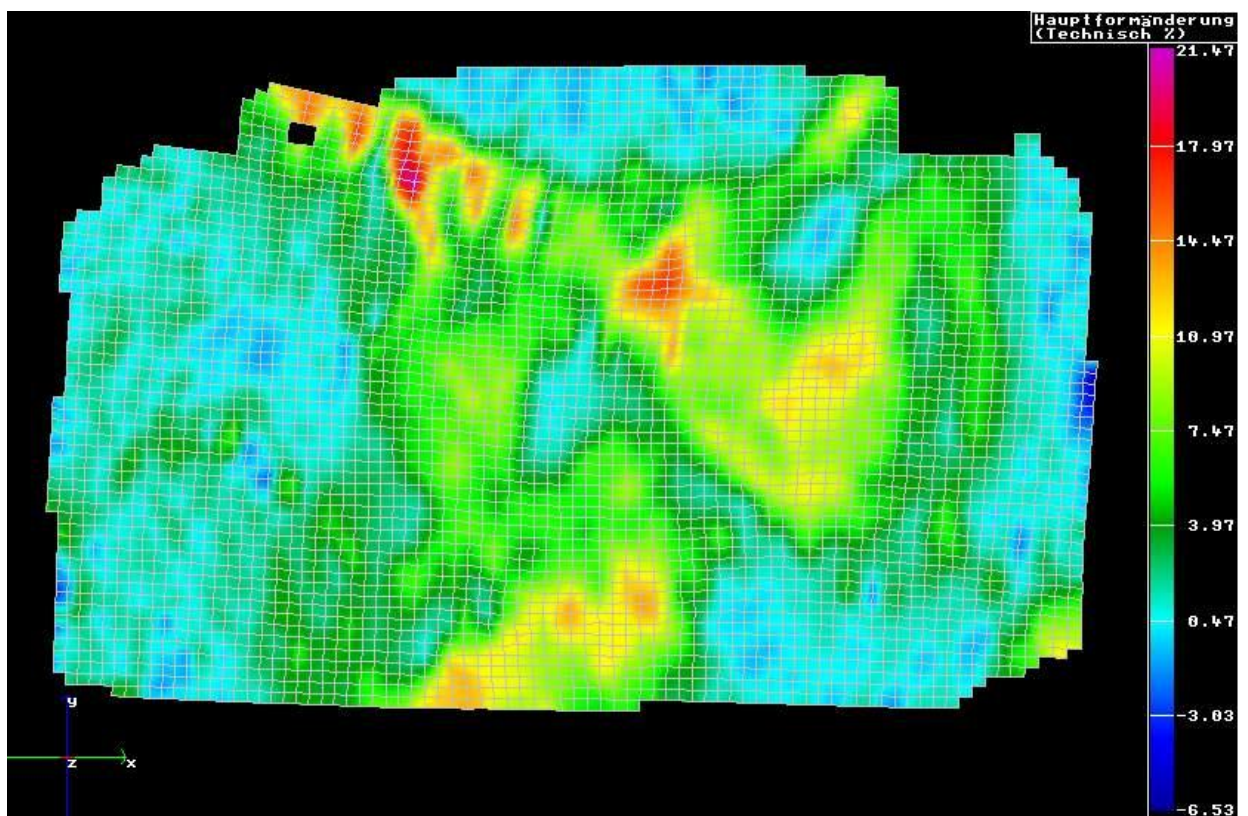
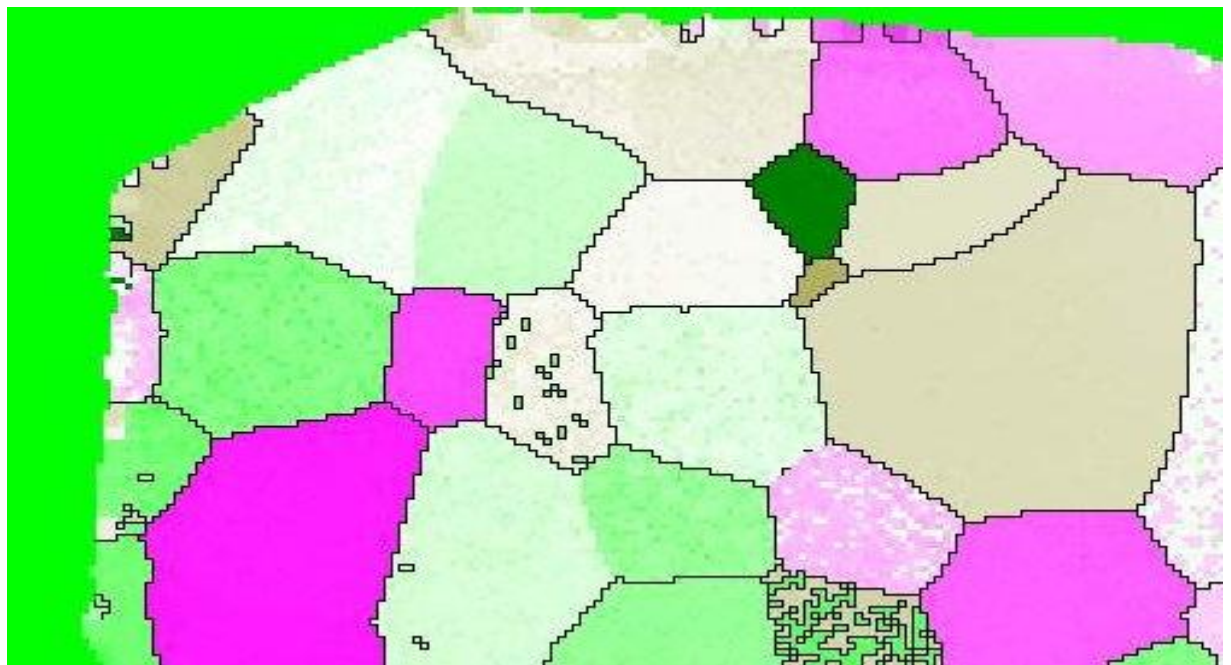
strain mapping





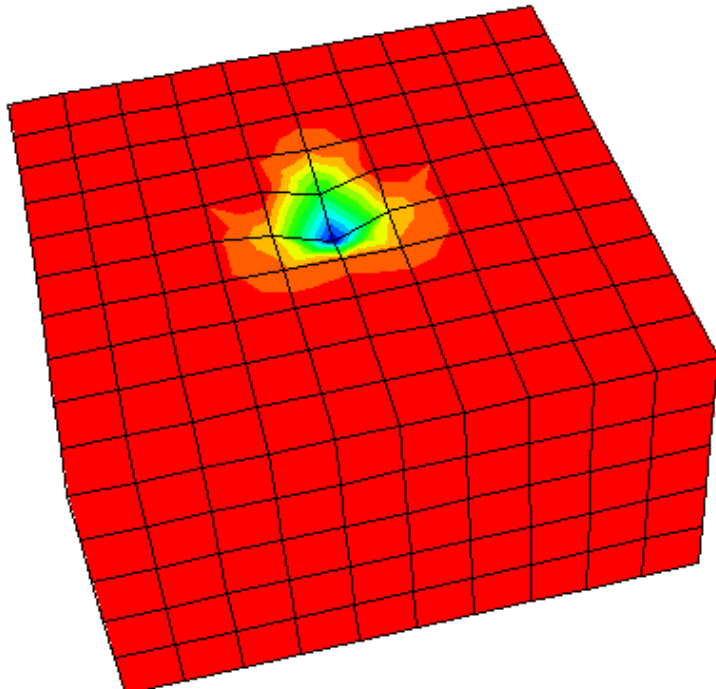
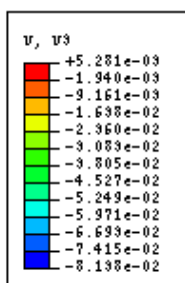
strain mapping



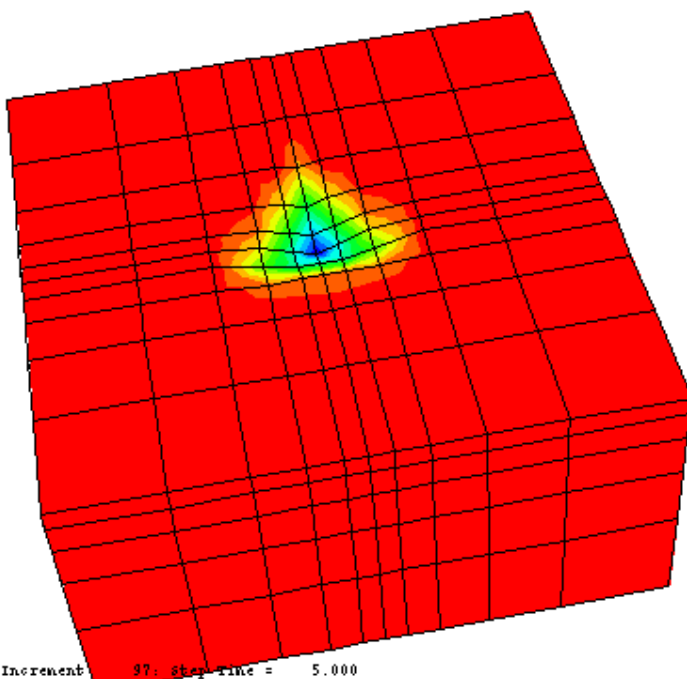
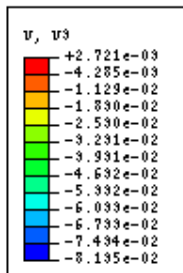


comparison (texture, strain)



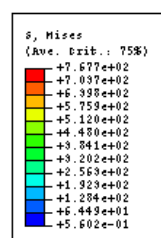


3
 2
 Step: unload Increment 115: step time = 5.000
 Primary Var: $U, U3$
 Deformed Var: U Deformation scale factor: +1.000e+00

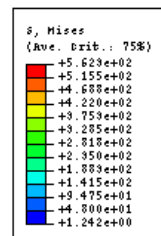


3
 2
 Step: unload Increment 97: step time = 5.000
 Primary Var: $U, U3$
 Deformed Var: U Deformation scale factor: +1.000e+00

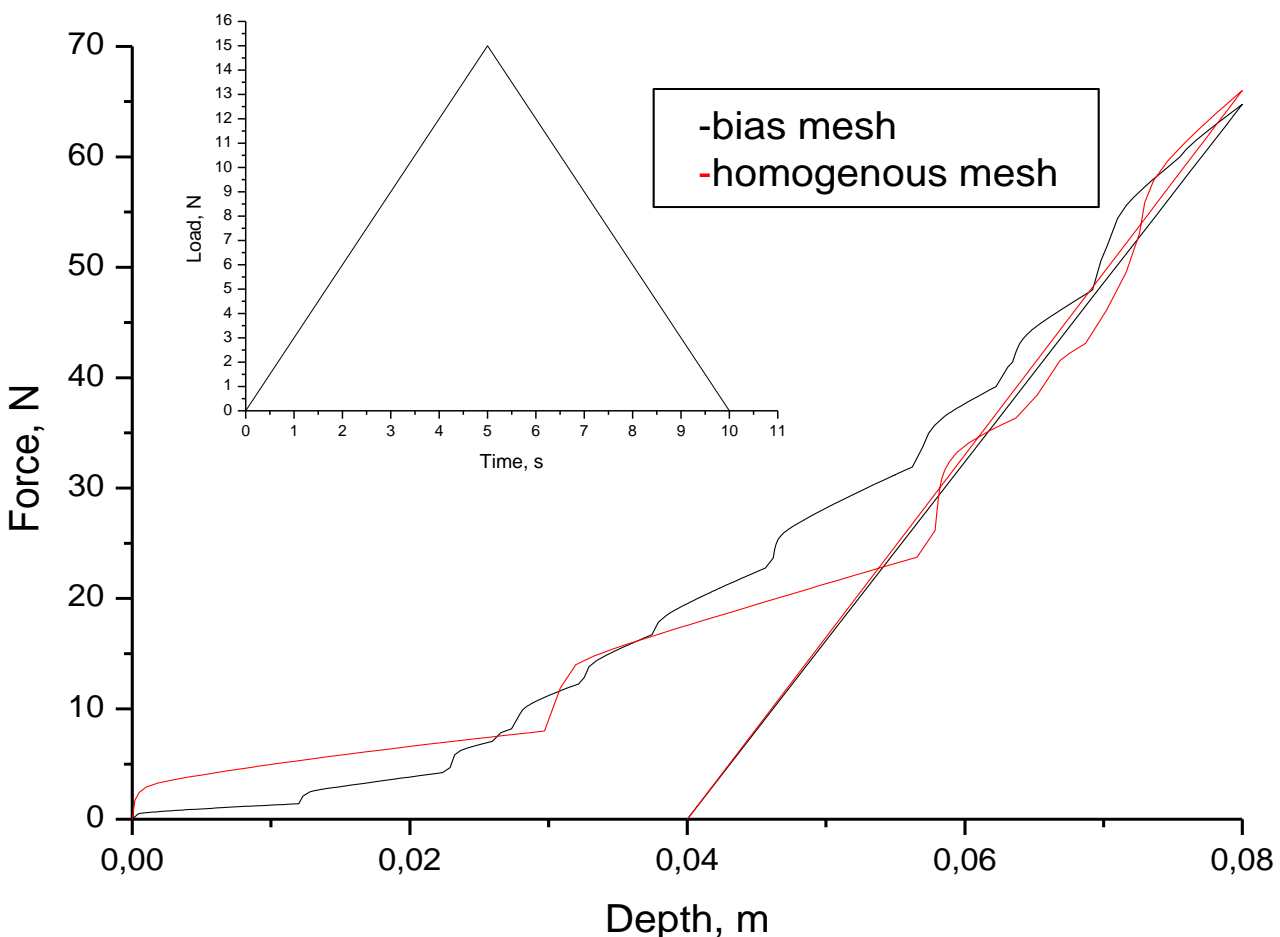




Step: load Increment 1060: Step Time = 1.344
Primary Var: σ , Mises
Deformed Var: U Deformation Scale Factor: +1.000e+00



Step: unload Increment 70: Step Time = 5.000
Primary Var: σ , Mises
Deformed Var: U Deformation Scale Factor: +1.000e+00



Three-dimensional investigation of the texture and microstructure below a nanoindent in a Cu single crystal using 3D EBSD and crystal plasticity finite element simulations

N. Zaafarani ^a, D. Raabe ^{a,*}, R.N. Singh ^b, F. Roters ^a, S. Zaefferer ^a

^a Max-Planck-Institut für Eisenforschung, Abteilung Mikrostrukturphysik und Umformtechnik, Max-Planck-Strasse 1, 40237 Düsseldorf, Germany
^b Mechanical Metallurgy Section, Materials Science Division, Bhabha Atomic Research Centre, Trombay, Mumbai 400 085, India

Received 15 October 2005; received in revised form 6 December 2005; accepted 8 December 2005

Available online 17 February 2006

Abstract

This paper reports a three-dimensional (3D) study of the microstructure and texture below a conical nanoindent in a (111) Cu single crystal at nanometer-scale resolution. The experiments are conducted using a joint high-resolution field emission scanning electron microscopy/electron backscatter diffraction (EBSD) set-up coupled with serial sectioning in a focused ion beam system in the form of a cross-beam 3D crystal orientation microscope (3D EBSD). The experiments (conducted in sets of subsequent (112) cross-section planes) reveal a pronounced deformation-induced 3D patterning of the lattice rotations below the indent. In the cross-section planes perpendicular to the (111) surface plane below the indenter tip the observed deformation-induced rotation pattern is characterized by an outer tangent zone with large absolute values of the rotations and an inner zone closer to the indenter axis with small rotations. The mapping of the rotation directions reveals multiple transition regimes with steep orientation gradients and frequent changes in sign. The experiments are compared to 3D elastic-viscoplastic crystal plasticity finite element simulations adopting the geometry and boundary conditions of the experiments. The simulations show a similar pattern for the absolute orientation changes but they fail to predict the fine details of the patterning of the rotation directions with the frequent changes in sign observed in the experiment. Also the simulations overemphasize the magnitude of the rotation field tangent to the indenter relative to that directly below the indenter tip.

© 2006 Acta Materialia Inc. Published by Elsevier Ltd. All rights reserved.

Keywords: 3D EBSD; Focused ion beam; Texture; Nanoindentation; Copper

1. Introduction and motivation

Nanoindentation is a well-established test method for the determination of mechanical properties at microstructural scales [1–3]. The mechanically relevant volume probed by this test typically lies between (30 nm)³ and (10 μm)³ depending on the indentation set-up and the material indented. Owing to its high lateral resolution, small-scale indentation is not only very useful for determining the mechanical heterogeneity of complex microstructures but also for investigating the local mechanical response of modern miniaturized electronic and engineer-

ing devices, micro-electromechanical systems (MEMS), and functional coatings [3].

Due to its complexity, small-scale indentation testing challenges modelers and experimentalists to better understand the deformation mechanisms that govern the mechanics in the indentation zone. The complexity of such tests arises from the complicated boundary and kinematic conditions, microstructural size effects, anisotropy, and heterogeneity of the deformation and stress fields as well as from the corresponding dislocation arrangements that are created below and around an indent [3–12].

There are two main benefits from an improved understanding of nanoindentation. First, the material parameters, which are commonly extracted from the force–displacement curves, could be placed on a more solid theoretical ground.

* Corresponding author. Tel.: +49 211 6792 333.

E-mail address: raabe@mpie.de (D. Raabe).

This applies in particular to the field of plasticity where a more detailed comprehension of the contact area, rate and relaxation effects, three-dimensional (3D) stress state, nanoscale friction, and material anisotropy might render the data acquisition more detailed and robust. Second, an enhanced understanding of indentation mechanics might enable one to extract and address a larger spectrum of constitutive material parameters than before. For instance it is conceivable to obtain tensorial rather than only scalar data, precise nanofriction coefficients, residual stresses, flow anisotropy, or small-scale damage effects from nanoindentations at a more quantitative scale than currently possible.

In that context this study addresses, as one particular aspect of nanoindentation, the formation of the crystallographic texture and microstructure in the deformation zone around an indent in three dimensions. For this purpose we use for the first time a novel experimental approach, namely a 3D electron backscatter diffraction (EBSD) texture and microstructure analysis. For this experiment we use a cross-beam microscope, which is a set-up of a high-resolution field emission scanning electron microscopy (SEM) instrument in conjunction with an EBSD system and a focused ion beam (FIB) microscope used for serial sectioning [13–15]. This technique allows us to map the deformation-induced lattice rotations below an indent in three dimensions. The experiment is conducted on a [111] Cu single crystal with a conical indenter using a Hysitron TriboIndenter set-up. A conical shape is used to avoid symmetries other than those of the crystal structure. The joint investigation of plastic deformation and induced lattice rotations is of great interest for an improved micromechanical understanding of indentation experiments owing to the close connection between crystallographic shear and the resulting lattice spin (the term “lattice spin” is in the following used synonymously for related terms such as crystalline reorientation, texture evolution, or induced lattice rotation).

The experimental 3D observations are compared to corresponding 3D elastic-viscoplastic crystal plasticity finite element simulations which adopt the geometry and boundary conditions of the experiments. The crystal plasticity finite element simulations are essential for the interpretation of the observed rotation fields. They allow us not only to establish the relationship between crystallographic shear and texture but also provide information about the spatial 3D distribution of the individual shear rates on the active slip systems that entail the observed lattice rotations. The latter aspect is of particular interest because the 3D distribution of the shear rate contributions of the 12 slip systems cannot currently be obtained by any other experimental or theoretical method owing to the heterogeneity of the indentation test.

To understand which contributions of the observed deformation and rotation pattern are due to isotropic mechanics as opposed to those effects that have an anisotropic crystallographic background, we also conduct simulations with a J₂ yield stress criterion (where J₂ is the

second invariant of the stress deviator as an isotropic yield criterion). This combination of isotropic and anisotropic (crystal plasticity) finite element simulations enables one to separate carefully macromechanical isotropic effects in the pattern formation from crystallographic aspects [16,17]. This approach has been successfully used before for the interpretation of crystallographic versus isotropic micromechanical aspects in the field of crystal plasticity [18,19].

2. Previous studies on deformation-induced lattice rotations during indentation

Only a few experimental studies have addressed the relationship between indentation and deformation-induced lattice rotations in the vicinity of an indent. In a set of recent papers the group of Larson et al. [20–24] obtained impressive results on the microstructure evolution below indents by using a non-destructive 3D synchrotron diffraction method. In their work they observed a systematic deformation-induced orientation pattern below [111] indents in Cu single crystals. The experimentally observed pattern was characterized by outward rotations at the rim of the indent (tangent zone of the indent) and inward rotations directly below the indent close to the indenter axis. The results were discussed in terms of Kröner's concept of geometrically necessary dislocations. Wang et al. [25] investigated the dependence of nanoindentation pile-up patterns and of lattice rotations for Cu single crystals with different orientations ([100], [110], and [111]) using a conical indenter. The 2D orientation measurements in this work were conducted around the indents at the surface with a high-resolution EBSD technique but no 3D analysis could be performed at that time.

Previous continuum-based indentation simulations aimed at elucidating the heterogeneity of the mechanics involved in such tests have been published by various groups. Most of these works, however, did not address the formation of crystallographic textures.

Besides the experiments mentioned above, Wang et al. [25] also conducted corresponding simulations using a 3D elastic-viscoplastic crystal plasticity finite element method. The group of Curtin [26,27] used coupled atomistic-continuum modeling for the investigation of nanoindentation. Smith et al. [28] conducted simulations of nanoindentation using an extended version of the quasicontinuum model, which works by embedding an interatomic force law within a finite element framework. Bolshakov and Pharr [29] have investigated the influence of material pile-up on the measurement of mechanical properties by load- and depth-sensing indentation techniques using finite element simulations of conical indentation. Fivel et al. [30] conducted 3D simulations of indent-induced plastic zones at the mesoscale using a combination of 3D discrete dislocation simulation and the finite element method. Durst et al. [31] conducted finite element simulations of spherical indentations in the elastic-plastic transition

regime. In their work they examined spherical indentations using various elastic–perfectly plastic constitutive material laws. Similar work was published by Park and Pharr [32] who investigated nanoindentation with spherical indenters by use of finite element simulations with particular reference to the elastic–plastic transition regime. Lichinchi et al. [33] conducted finite element simulations of nanoindentation of thin films. They applied the method to the investigation of the stress–strain field of thin hard coatings subjected to nanoindentation. Durst et al. [34] conducted finite element simulations of the indentation size effect in metallic materials introducing a correction for the size of the plastic zone. In another work, Durst et al. [35] published a finite element study of nanoindentation measurements on two-phase elastic–plastic materials. In this study, they used the approach to investigate the influence of the shape and the aspect ratio of particles embedded in a matrix material on the deformation behavior and hardness during depth-sensing indentation.

Very detailed atomistic simulations of the incipient stages of nanoindentation in face-centered cubic (fcc) single crystals were recently conducted by Li et al. [36] and Van Vliet et al. [37]. These studies provided excellent insights into the early stages of nucleation of slip during the beginning of indentation. The data revealed a strong influence of the crystallography on the formation of surface patterns.

3. Experimental

3.1. Material and sample preparation

A copper single crystal with a (111)-oriented surface plane was drawn from the melt and cut into a cube-shaped specimen by spark erosion. The surface plane was wet ground, diamond polished, and finally electropolished. An array of indents was placed on the (111) plane of the single crystal at a distance of 50 µm from the edge. After indentation the crystal was diamond polished along the (112) plane using a particle size of 1 µm in order to remove about 20 µm of material perpendicular to the indented (111) surface (Fig. 1). After polishing, the sample was cleaned in an ultrasonic acetone bath for 5 min. After that pure water and high-pressure air were used to clean the sample of the acetone. The serial sectioning procedure required for the 3D EBSD analysis was directly conducted in the Zeiss joint high-resolution field emission cross-beam 3D SEM/EBSD microscope by the FIB unit (Fig. 2).

3.2. Hardness testing

The nanohardness tests were performed using a Hysitron nanoindenter system (TriboIndenter). The instrument included an XYZ sample stage and a set-up combining a piezo-scanner as known from conventional atomic force microscopy (AFM) with a transducer and a conical diamond indenter tip. The XYZ stage was used for the fine

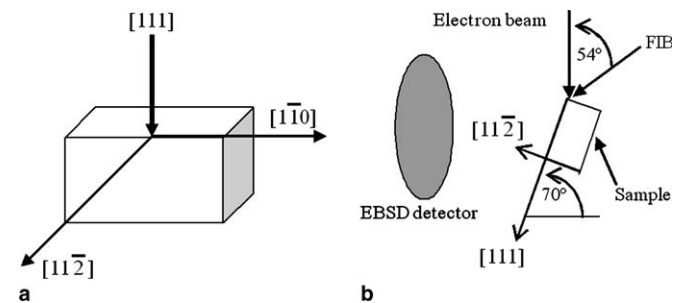


Fig. 1. Schematic showing (a) the crystal directions and (b) the arrangement of the incident secondary electron beam, the specimen, the FIB, and the EBSD detectors. Indents were made into the crystallographic (111) plane whereas serial sectioning was performed along the [112] crystallographic direction (details in Fig. 2).

positioning of the sample under the piezo-scanner and for the approach of the indenter.

The experiments were carried out with a conical indenter in order to avoid symmetries other than those of the crystal structure. The nanohardness tests were conducted in load-controlled mode. A triangular loading–unloading pattern was used with a maximum peak load of 10 mN but without any holding time at that load. Loading and unloading were conducted at the same rate of 1.82 mN/s. The displacement of the indenter was measured simultaneously to give a force–displacement curve. To calculate both hardness and Young's modulus accurately from the force–displacement data, it was necessary to know the exact geometry of the indenter tip. Since the depth of penetration in the copper single crystals was too large to be achieved in quartz, the indenter cross-sectional area function was determined by performing indentation tests at different depths on an alternative material with a known and constant Young's modulus (poly(methyl methacrylate)). Some 36 indentation tests in the form of a 6 × 6 matrix with a spacing of 20 µm between the indents and an indentation depth of about 900 nm were performed, and both hardness and Young's modulus were calculated for each of them. The surface profiles of the indented and surrounding area were determined using AFM.

3.3. Serial sectioning by FIB and 3D EBSD measurements

Our current approach to 3D EBSD was inspired by the work of Uchic et al. [13] and Zaefferer et al. [14,15] as well as by the 3D texture measurements via synchrotron radiation published by the group of Larson [20–24].

The 3D EBSD experiments were conducted using a joint high-resolution field emission SEM/EBSD set-up together with a FIB system in the form of a Zeiss cross-beam 3D crystal orientation microscope. SEM allows for the observation with SE, backscattered electrons, scanning transmission electron microscopy, EBSD, and energy dispersive X-ray analysis. The integrated scanning Ga⁺ FIB device allows for the observation with ion-induced SE as well as for sputtering (milling) for serial sectioning, transmission electron microscopy thin-foil preparation, surface

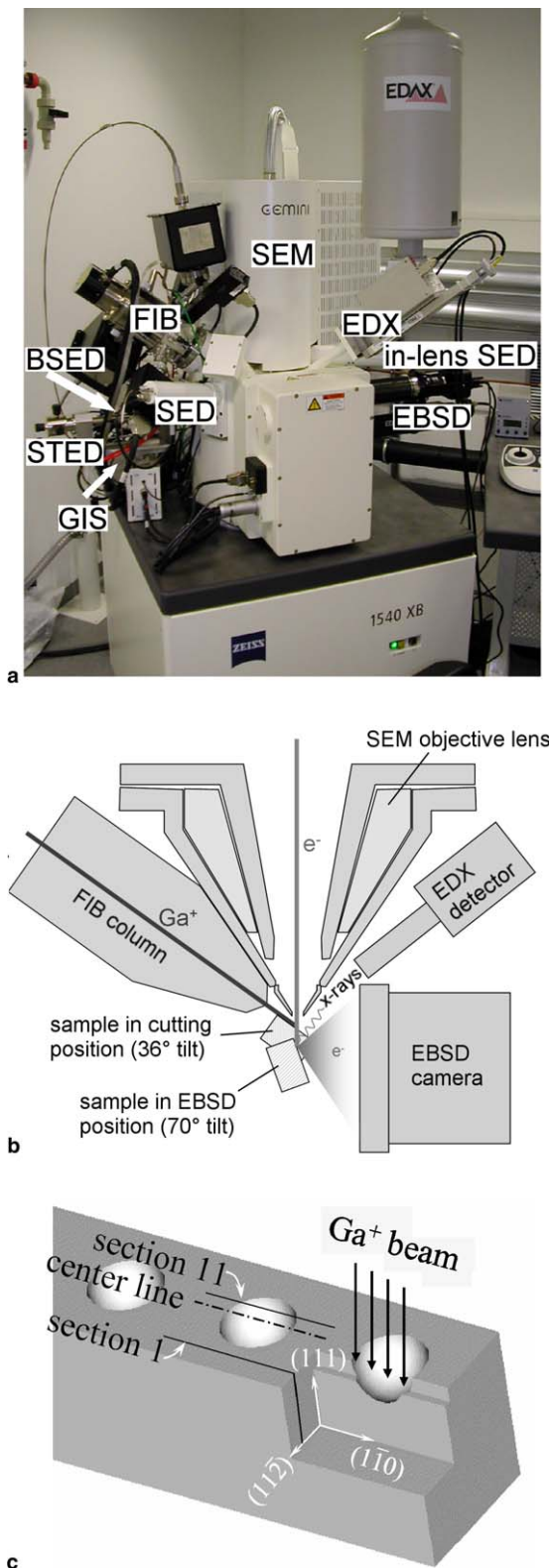


Fig. 2. (a) Joint high-resolution field emission SEM/EBSD set-up together with a FIB system in the form of a cross-beam 3D crystal orientation microscope for conducting 3D EBSD measurements by serial sectioning (Zeiss) [14,15]. (b) Schematic of the joint FIB/EBSD set-up. (c) Schematic of the FIB sectioning geometry. The exact positions of the sections where EBSD mappings were taken are given in Table 1.

structuring, and the deposition of various types of films (W, Pt, SiO₂) from organic precursor gasses.

The particular analysis method chosen in this study involved conducting highly precise and fully automated serial sectioning with the FIB and subsequently mapping the texture in each of those layers using high-resolution EBSD. This approach requires a quick and precise change between milling for serial sectioning (sample at 36°) and EBSD mapping (sample at 70°) (Fig. 2). The minimum possible spatial resolution of the 3D pixels amounts to about 50 × 50 × 50 nm³ [14,15]. The ion beam did not create noticeable damage, i.e., no serious deterioration of the EBSD pattern quality was observed after milling the copper single crystal. In order to provide protection of the free edges against diffuse FIB cutting, a tungsten layer about 1 μm thick was deposited on the surface over the indent before starting the milling process.

In total a volume of 20 μm along the [112], 30 μm along the [110], and 20 μm along the [111] direction was removed by FIB serial sectioning in front of the indent to expose gradually the volume inspected. The incident angle of the FIB was normal to the (111) plane and an ion beam current of 500 pA was used for removing the material. For the last milling step before the EBSD characterization a smaller beam current of only 100 pA was used in order to obtain less roughness and better Kikuchi pattern quality. After this final FIB polishing step the sample was tilted to the standard EBSD measurement position. The electron beam had an angle of 20° relative to the [111] direction on the (112) crystal plane. The EBSD measurements were carried out in each layer after serial sectioning at a step size of 80 nm. The whole process of alternating FIB sectioning and EBSD measurements was carried out for a set of 11 subsequent layers through the 3D deformation zone around the indent.

Table 1 shows that a set of subsequent serial sections were placed near the center plane below the actual indenter tip. For each of those planes EBSD mappings were obtained. The texture data were analyzed in terms of the misorientation angle with respect to the undeformed crystal, of the sense of the crystallographic re-rotation and the axis of rotation.

Table 1
Distance of serial sections from the center plane below the indent

Serial section plane number	Distance from center plane below the indent (μm)	Serial section plane number	Distance from center plane below the indent (μm)
1	7.22	2	5.97
3	5.24	4	1.57
5	0.876	6	0.796
7	0.641	8	0.474
9	0.318	10	0.176
11	−0.484		

4. Simulation of Cu single-crystal indentation

4.1. Introduction

Nanoindentation experiments require careful control of a set of boundary conditions, such as the surface finish, defect-free subsurface of the sample indented, accuracy of the indenter surface and shape, and precise data acquisition. These difficult experimental conditions suggest the use of a finite element approach for simulating indentation. This allows one to investigate the evolution of the material characteristics during the entire indentation process and assign the material data obtained to a specific stress-strain state of the experiment at each instant. In addition it allows one to investigate the sample interior and to modify systematically material or process parameters for conducting numerical experiments.

4.2. Constitutive model

4.2.1. Flow rule

In order to describe the flow kinematics, the finite deformation defined by the deformation gradient F is multiplicatively decomposed into two contributions, namely the elastic part of the deformation gradient F_e and the plastic part of the deformation gradient F_p . The latter quantity describes an intermediate configuration accounting only for the deformation induced by the plastic slip in the lattice, i.e., $\det|F_p|=1$. F_e captures both the stretch and the rotation of the lattice. The flow rule is used in the form

$$\dot{F}_p = L_p F_p \quad (1)$$

where the plastic velocity gradient L_p is given by

$$L_p = \sum_{\alpha} \dot{\gamma}_{\alpha} (m_0^{\alpha} \otimes n_0^{\alpha}) \quad (2)$$

in which m_0^{α} and n_0^{α} are the orthonormal vectors describing the slip direction and the slip plane normal of the slip systems α in the reference configuration, respectively, and $\dot{\gamma}_{\alpha}$ describes the shear rates on the slip systems α .

4.2.2. Hardening mechanism

The material law is based on a crystal plasticity model introduced by Kalidindi et al. [38,39] for the prediction of crystallographic texture based on the phenomenology of the fcc lattice. The hardening law on a slip system α follows:

$$\dot{\gamma}_{\alpha} = \dot{\gamma}_0 \left| \frac{\tau_{\alpha}}{s_{\alpha}} \right|^{1/m} \text{sign}(\tau_{\alpha}) \quad (3)$$

where $\dot{\gamma}_{\alpha}$ is the shear rate on the slip system subjected to the resolved shear stress τ_{α} having a slip resistance of s_{α} . $\dot{\gamma}_0$ and m are material parameters and are the reference shear rate and the rate sensitivity of slip. The influence of any other slip system β on the hardening behavior of system α is given by

$$\dot{s}_{\alpha} = \sum_{\beta} h_{\alpha\beta} |\dot{\gamma}_{\beta}| \quad (4)$$

where

$$h_{\alpha\beta} = q_{\alpha\beta} \left[h_0 \left(1 - \frac{s_{\beta}}{s_s} \right)^a \right] \quad (5)$$

In this formulation h_0 , a , and s_s are slip hardening parameters, which are assumed to be identical for all fcc slip systems owing to the underlying characteristic dislocation reactions [38,39]. The parameter $q_{\alpha\beta}$ is taken as 1.0 for coplanar slip systems α and β and 1.4 otherwise. The time integration procedure for updating the stresses at the intermediate configuration at time $T = (t + \Delta t)$ is represented by

$$\sigma^*(T) = \sigma^*[s_{\alpha}(T), F(T), F_p(t)] \quad (6)$$

$$s_{\alpha}(T) = s_{\alpha}[s_{\alpha}(t), s_{\beta}(T), \sigma^*(T)] \quad (7)$$

which are solved iteratively. The Cauchy stress σ can be determined by

$$\sigma = \frac{1}{\det|F_e|} F_e \sigma^* F_e^T \quad (8)$$

4.2.3. Determination of the constitutive parameters

A compression test for a Cu single crystal was performed in order to determine the values for the material parameters required for the model. Loading was along the [1 1 1] axis, which results in six active slip systems with the same Schmid factor of 0.2722 (Table 2).

The sample used for the compression test was a wire-cut cylinder with dimensions of 3 mm × 4.5 mm (diameter × length). The compression speed was 0.1 mm/s resulting in an average overall strain rate of $4.3 \times 10^{-4} \text{ s}^{-1}$. The strain rate could then be resolved in the shear rate over each activation plane by

$$\dot{\gamma}_{\alpha} = \frac{\dot{\varepsilon}}{6 \times S_{\text{Schmid}}} \quad (9)$$

By fitting the material parameters in the model excellent correspondence could be achieved with the experimental results (Fig. 3). The resulting constitutive material parameters are $h_0 = 200 \text{ MPa}$, $a = 1$, $s_s = 75 \text{ MPa}$, $m = 0.012$. The initial value of the slip resistance was chosen as 8 MPa and $\dot{\gamma}_0$ was taken to be 0.001 s^{-1} . The elastic constants were those for pure Cu, i.e., $C_{11} = 168 \text{ GPa}$, $C_{12} = 121.4 \text{ GPa}$, $C_{44} = 75.4 \text{ GPa}$.

4.2.4. Finite element model

The constitutive model with the time integration procedure outlined above was implemented in the finite element code MARC using the user-defined subroutine HYPELA2 for the simulation of the indentation of the Cu single crystal [40]. The mesh consisted of 1888 elements (3D quadrilateral, 8 integration points) and 2205 nodes (Fig. 4). Near the center of the model special care was taken when designing the mesh owing to the possibility of high element distortion. Because of the large difference in the elastic stiffness of the diamond indenter and the Cu sample (10:1) the indenter was assumed rigid. As a boundary condition the lower face of the modeled cylinder was kept restricted from any degree

Table 2

Active planes for a Cu single-crystal compression with [111] loading axis

Plane	(111)			(\bar{1}11)			(1\bar{1}\bar{1})			(\bar{1}\bar{1}1)		
System	A1	A2	A3	B1	B2	B3	C1	C2	C3	D1	D2	D3
Direction	01\bar{1}	\bar{1}01	1\bar{1}0	01\bar{1}	101	\bar{1}\bar{1}0	0\bar{1}\bar{1}	\bar{1}01	110	0\bar{1}\bar{1}	101	\bar{1}10
Schmid factor	0	0	0	0	0.2722	0.2722	0	0.2722	0.2722	0.2722	0.2722	0

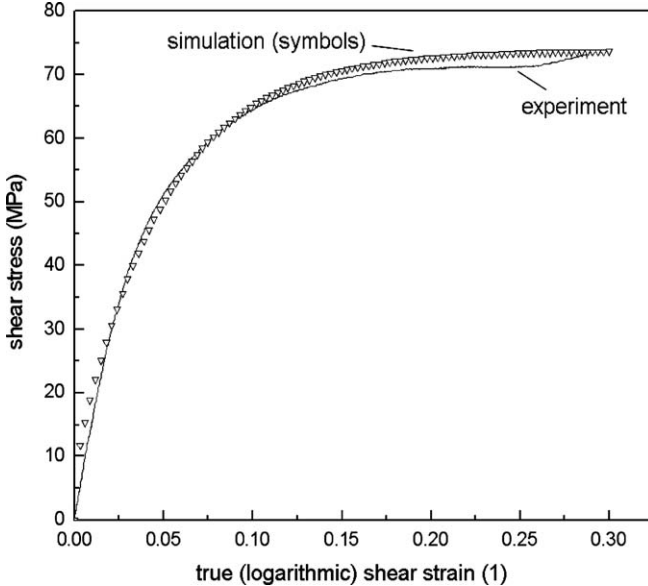


Fig. 3. Stress–strain curve for a shear test obtained from experiment and model fit. The material parameters for the fitting procedure were $h_0 = 200$ MPa, $a = 1$, $s_s = 75$ MPa, $m = 0.012$, an initial value of slip resistance s_0 of 8 MPa, and $j_0 = 0.001 \text{ s}^{-1}$ (see details in Eqs. (1)–(7)).

of freedom. All other nodes were free to move in any direction. Zero friction was assumed between indenter and sample. The initial orientation of the sample was chosen by selecting appropriate Euler angles such that the x , y , z coordinate system represents the $[1\bar{1}0]$, $[11\bar{2}]$, and $[111]$ crystal directions, respectively.

5. Results and discussion

Fig. 5 shows a micrograph of the indented matrix (Fig. 5(a)) and a close-up of one of the indents

(Fig. 5(b)). Fig. 5(c) shows the sixfold symmetry of the pile-up pattern around the (111) indent, which was earlier observed by Wang et al. [25]. Fig. 6 shows SEM images of two different serial sections along the $[11\bar{2}]$ crystal direction, one before the actual indent (Fig. 6(a)) and the other close to the indenter tip (Fig. 6(b)). The micrographs also show the protective tungsten layer that was deposited before the FIB milling process in order to prevent the erosion of the surface edge. The micrographs reveal that a substantial amount of material had to be removed by milling in order to avoid shadowing effects during the subsequent EBSD measurements. From a series of tests we observed that the optimum milling geometry had to follow a trapezoidal shape (Fig. 6(a)).

Fig. 7 shows sets of successive $(11\bar{2})$ serial sections perpendicular to the (111) indentation plane. The sections were taken at different spacings from the actual indenter tip (for geometrical details see Figs. 1 and 2). Scan 4 is far away from the indenter tip (1567 nm) and scan 10 is close to the indenter tip (176 nm) (Table 1). The color code indicates the magnitude of the orientation change relative to the initial undeformed crystal orientation. The color scheme and scaling is identical for all diagrams. The images on the left-hand side (Fig. 7(a)–(h)) were obtained from crystal plasticity finite element simulations as outlined above. The corresponding misorientation maps on the right-hand side were determined via EBSD measurements in each layer prepared by serial FIB sectioning (Fig. 7(i)–(p)). The positions of the simulation results correspond exactly to the cutting positions where the experimental texture mappings were taken. Sections that were more remote from the indent than Section 4 did not reveal a substantial microtexture pattern and are, therefore, not shown. Fig. 8(a) provides a closer view of the microtexture pattern using a different scaling from that in Fig. 7.

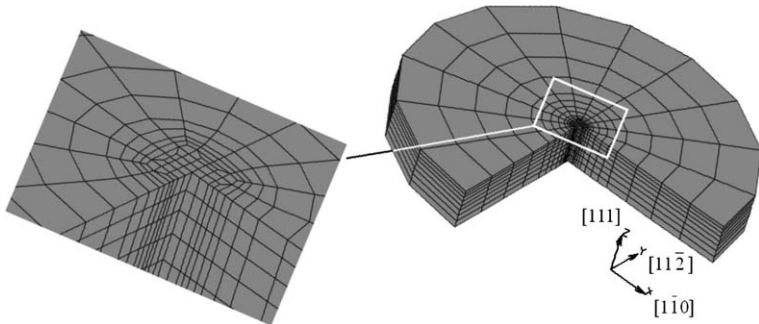


Fig. 4. FEM model. The same mesh was used for the crystal plasticity finite element simulation which considers both elastic and plastic anisotropy and also for the isotropic (J2) finite element simulation. The x , y , z coordinate system represents the $[1\bar{1}0]$, $[11\bar{2}]$, and $[111]$ crystal directions, respectively, in the case of the crystal plasticity finite element simulations.

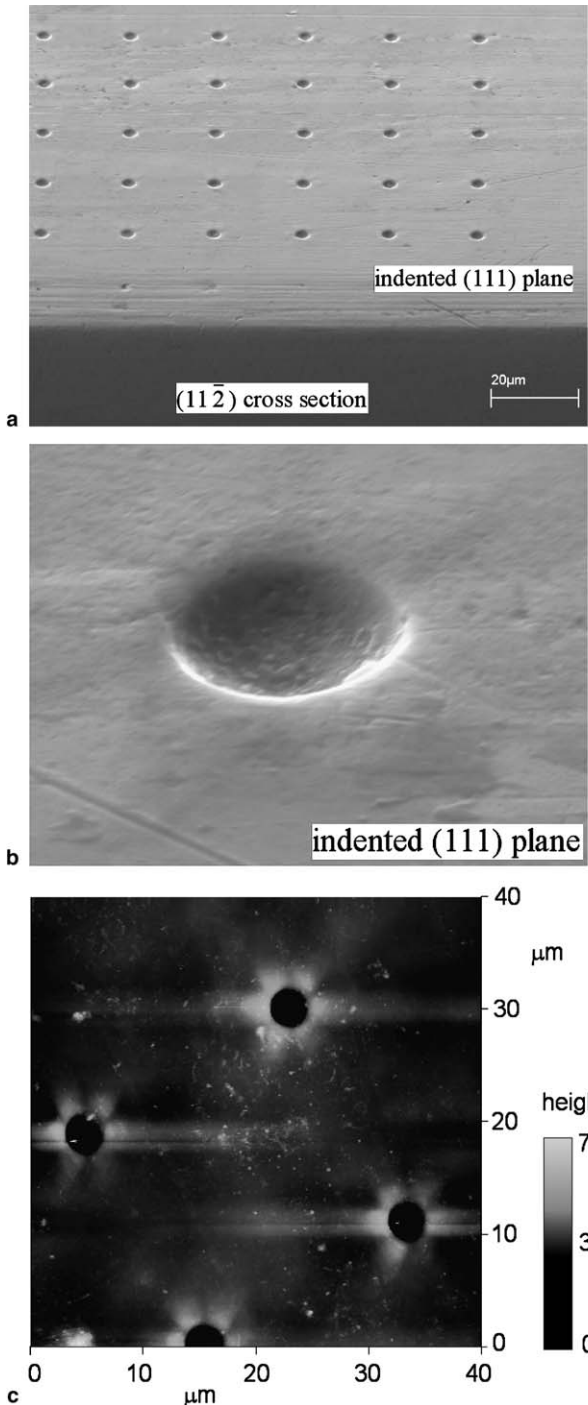


Fig. 5. SEM images of (a) the 6×6 matrix of indents and (b) a close-up of one of the indents. (c) AFM mapping of the surface roughness around the indents in the (111) plane of the copper single crystal. The AFM image reveals the sixfold pile-up symmetry around the indents characteristic of [111] indents in Cu [25].

One important result from Figs. 7 and 8 is that, although the simulations and experiments show basically similar rotation patterns, they do not reveal a one-to-one correspondence.

The crystal plasticity finite element simulations reveal a single peak behavior for the misorientation pattern in

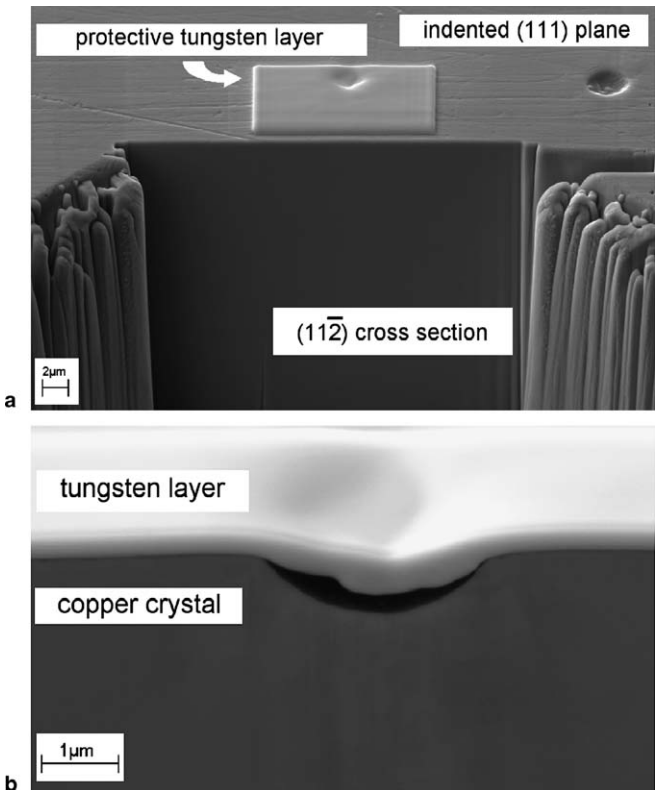


Fig. 6. SEM images of a serial section (a) before the actual indent and (b) at the indent.

Section 4, i.e., 1567 nm far away from the indenter tip (Fig. 7(a)). In sections closer to the indenter tip (scans 5 and 6; Fig. 7(b) and (c); Table 1) the simulated distribution of the deformation-induced lattice rotations shows a double-well pattern with steep maxima below the zones tangent to the indenter. Sections close to the indenter tip (scans 7–11; Fig. 7(d)–(h)) show a simulated distribution of the lattice rotations with the same dominant double-well pattern with steep reorientation maxima below the tangent zones as already simulated for Sections 5 and 6 but with additional minor rotation zones close to the indenter tip. Of particular interest are the simulation results for scan 7 (Fig. 7(d)) and 11 (Fig. 7(h)). Scan 7 shows a new very small maximum of the deformation-induced rotation in the inner tangent region close to the indenter tip. This pattern can be referred to as an inner double-well pattern (see also the image on the right-hand side of Fig. 9(b)). Scan 11 shows a new maximum in the deformation-induced rotation pattern that appears exactly at the position of the indenter tip. The lateral arrangement of the orientation changes allows one to differentiate coarsely between six different characteristic regions (Fig. 8(b)). Regions 1 and 6 do not reveal large orientation changes (below 4° in the experiment). Regions 2 and 5 are characterized by large strains and correspondingly by large orientation changes (up to 16° in the experiment). Regions 3 and 4 reveal smaller lattice rotations (below 14° in the experiment). The experimental data obtained for scans 6–9 reveal particularly

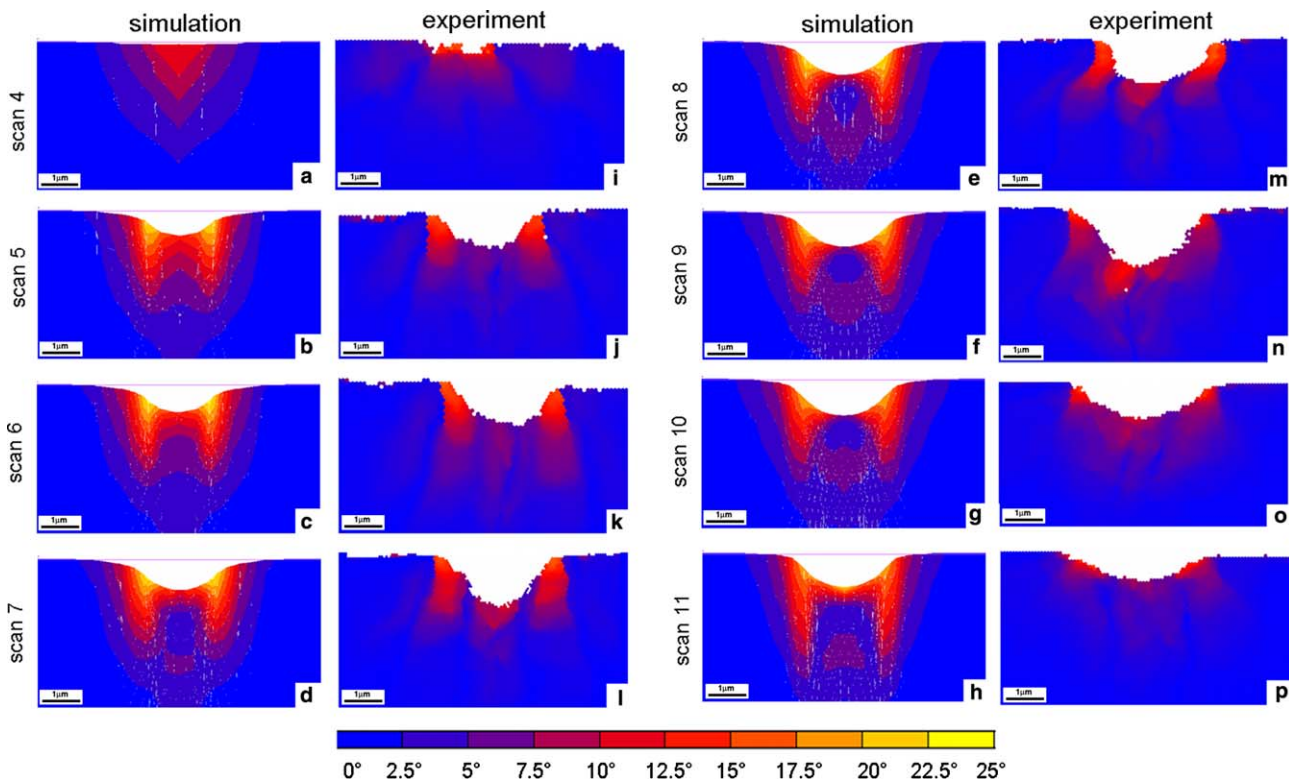


Fig. 7. Rotation maps for a set of successive $(11\bar{2})$ sections perpendicular to the (111) indentation plane (surface plane perpendicular to the plane presented) with different spacing to the actual indent. Scan 4 is far away from the indenter tip (1567 nm) while scan 10 is close to it (176 nm) (see details in Figs. 1 and 2 and Table 1). The images on the left-hand side (a–h) were obtained from viscoplastic crystal plasticity simulations. The corresponding maps on the right-hand side (i–p) were determined via EBSD measurements in succeeding planes prepared by serial FIB sectioning. The color code shows the magnitude of the orientation change relative to the initial crystal orientation without indicating the rotation axis or rotation direction. Scaling is identical for all diagrams.

steep orientation gradients in part over a length of less than 100 nm in the transition area between regions 2 and 3 and regions 4 and 5, respectively (Figs. 7 and 8(a)).

Although showing a similar deformation-induced lattice rotation pattern in terms of the magnitude of the rotations

as the simulations (Fig. 7(a)–(h)), the experimental results (Fig. 7(i)–(p)) reveal also some differences. First, the EBSD experiments generally reveal a smaller magnitude of the maximum occurring lattice rotations as compared to the simulations. While the simulations are characterized by

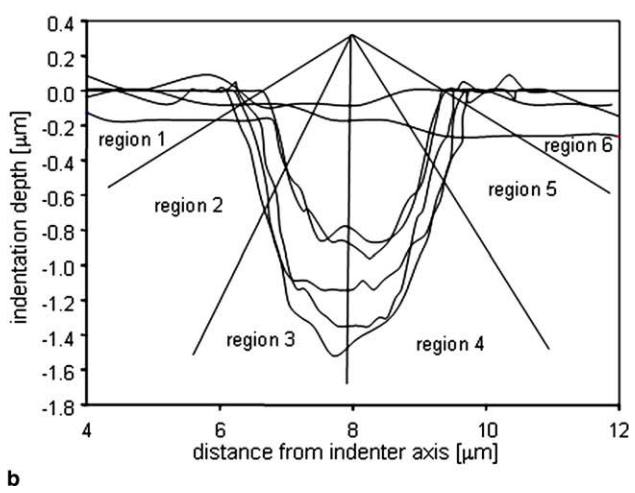
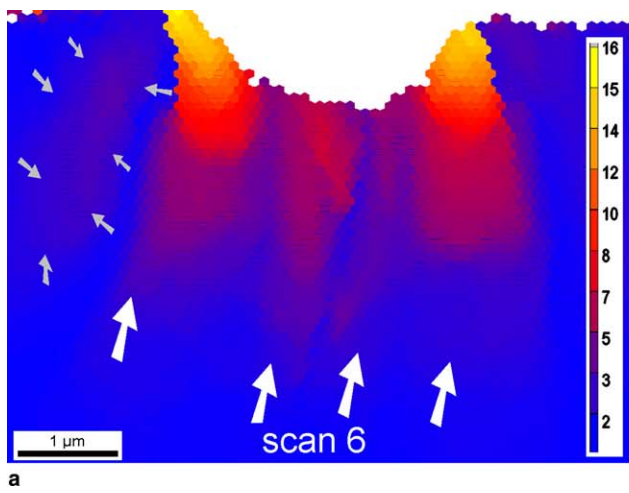


Fig. 8. (a) Closer view of the experimentally observed pattern of the absolute values of the deformation-induced crystalline lattice rotations in degrees in the vicinity of the indent using a different scaling from that in Fig. 7. The rotation axis and rotation direction are not indicated (see Figs. 12–14 for this information). (b) From the distribution of the shear rates and lattice rotations six different deformation zones can be roughly identified. The diagrams are $(11\bar{2})$ sections.

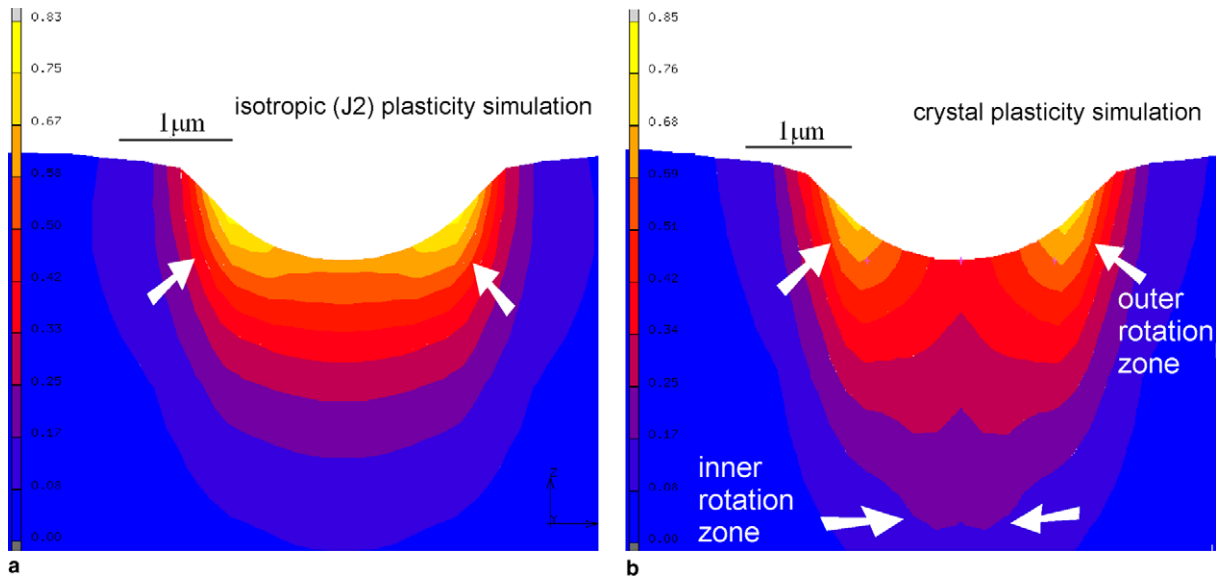


Fig. 9. Von Mises equivalent strain distribution in the middle section directly below the indenter tip obtained from two different types of finite element simulations (same mesh in both cases, see Fig. 4). (a) Finite element simulation with an isotropic plastic constitutive J2 model (no preferred directions; J2: second invariant of the stress deviator as an isotropic yield criterion). (b) Finite element simulation with an anisotropic crystal plasticity constitutive model, as explained in Section 4, in the crystallographic $(\bar{1}\bar{1}2)$ plane.

maximum misorientations of up to 25° relative to the starting orientation, the experiments show smaller values of the maximum occurring misorientations of only 16° . A second

difference between simulation and experiment is that practically all sections obtained from the experiments reveal a pronounced inner pattern (i.e., close to the indenter tip;

Slip Plane	(111)			$(\bar{1}\bar{1}1)$		
	011	$\bar{1}01$	$\bar{1}10$	011	101	110
Slip Direction	011	$\bar{1}01$	$\bar{1}10$	011	101	110
Schmid factor	0	0	0	0	0.2722	0.2722
center of indent (110) upper surface						
Shear strain on slip system	0.375	0.376	0.320	0.093	0.740	0.847

Slip Plane	$(\bar{1}\bar{1}1)$			$(\bar{1}\bar{1}1)$		
	011	$\bar{1}01$	110	011	101	$\bar{1}10$
Slip Direction	011	$\bar{1}01$	110	011	101	$\bar{1}10$
Schmid factor	0.2722	0	0.2722	0.2722	0.2722	0
center of indent (110) upper surface						
Shear strain on slip system	0.719	0.094	0.852	0.747	0.754	0.125

Fig. 10. Distribution of the shear strains on all 12 slip systems as extracted from the crystal plasticity finite element simulation in the indented (111) plane. Six systems carry the largest portion of the deformation (the amount of shear is given in the bottom rows). The Schmid factors are calculated for the simplified assumption of compression along the $[111]$ axis.

see white arrows in Fig. 8(a)) of orientation changes within the larger outer double-well pattern tangent to the indent that dominated the predicted rotation pattern. In general it seems that the experimentally observed rotation patterns are characterized by a more rapid change in the rotation field among neighboring material portions than the simulations. This point will be discussed below in more detail when analyzing also the direction of the deformation-induced rotations. A third obvious difference between simulation and experiment is that the experimental data are less symmetric than the predicted ones since the experimentally observed rotation patterns appear somewhat distorted at least in some sections.

Concerning the deviation in the magnitude of the simulated and experimentally observed orientation changes, two aspects have to be considered. The first is that owing to edge effects and milling-induced curvature, the EBSD method misses mapping the microstructure that is closest to the actual interface between the indented material and the surface of the indenter. These zones are the ones where the rotation rates should be highest according to the simulated deformation and rotation patterns. This means that the interface layers with the largest deformation-induced rotations were probably not completely mapped by the experiment. This might amount to a layer of 100–200 nm at most and would explain the difference in the magnitude of the rotations observed between the experiment and simulation. The second aspect is the fact that the crystal plasticity finite element simulation method used in the current work does not take into account gradient terms at a slip system level in the constitutive description. This means that the predicted rotation rates are presumably exaggerated. The reason for this assumption is that the consideration of gradient terms in a crystal plasticity constitutive environment exerts a penalty term against high local rotation rates of the lattice. This applies in particular when neighboring material portions have less of a tendency to follow that

rotation. In such a case (which is typical of an indentation boundary condition) such rapid changes in the local texture evolution require a rapid corresponding accumulation of geometrically necessary dislocations for the accommodation of the resulting mismatch in the lattice spin among neighboring material portions [20–24,41–45]. The observation that the experimentally observed rotation patterns show at least four (if not more, see faint maximum on the left-hand side of Fig. 8(a), small gray arrows) characteristic misorientation peaks much more clearly than the simulations can be discussed in terms of Fig. 9. This figure shows the von Mises equivalent strain distribution in the middle section directly below the indenter tip as obtained from two different types of finite element simulations. The simulation result in Fig. 9(a) shows finite element simulations with an isotropic plastic constitutive model without any preferred crystallographic directions. The result in Fig. 9(b) shows simulations with the anisotropic crystal plasticity constitutive model as introduced above ((112) section). Both types of simulations were conducted using the same mesh (Fig. 4). The comparison between the isotropic and the anisotropic case clearly reveals that the main outer double-well pattern where the deformation (and hence also the crystalline rotation) is accumulated in the shear zones tangent to the indent is not a purely crystalline phenomenon but occurs also in the isotropic case (see arrows in Fig. 9(a)). The crystal plasticity simulation shows the same outer double-well strain pattern as the isotropic simulation, but it reveals additionally a second inner double-well pattern (see arrows at the bottom of Fig. 9(b)). This means that the inner portion of the strain pattern, which supposedly gives rise to a corresponding rotation pattern (Figs. 7 and 8) has a clearly crystallographic origin, i.e., it must be due to the crystalline discreteness of the plastic slip.

Fig. 10 provides a more detailed view of the simulated distribution of the plastic deformation around the indent. It reveals for each of the 12 slip systems the accumulated

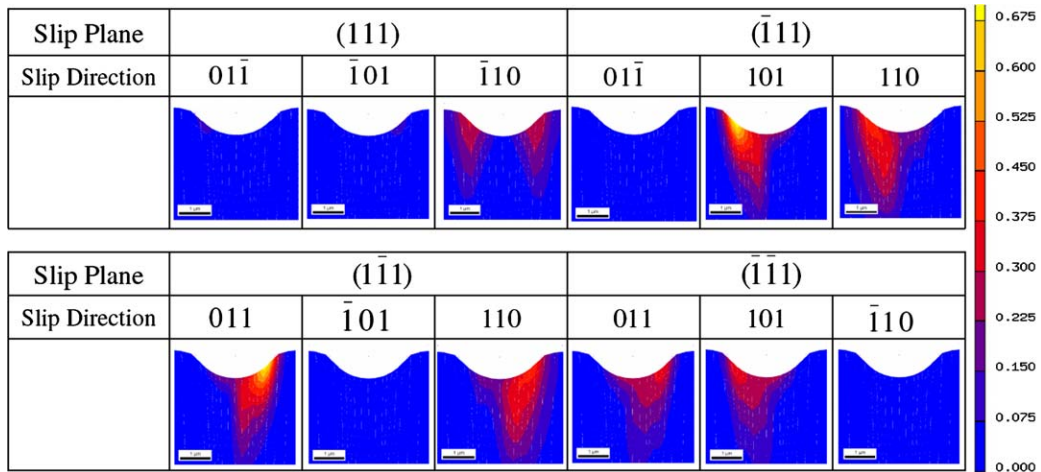


Fig. 11. Distribution of the shear strains on the 12 slip systems, predicted by the crystal plasticity finite element simulation. View in the crystallographic (112) plane below the indenter tip.

shear strain as predicted by the crystal plasticity finite element simulation. The result shows that six slip systems carry the largest portion of the overall plastic deformation (see the amount of shear in the two bottom rows). These dominant systems are the $(\bar{1}11)[101]$, $(\bar{1}11)[110]$, $(1\bar{1}1)[011]$, $(1\bar{1}1)[110]$, $(\bar{1}\bar{1}1)[011]$, and $(\bar{1}\bar{1}1)[101]$ slip systems. This result of the simulation is quite obvious and matches earlier observations [25]. It is in accord with the maximum orientation factors on these systems for the simplified assumption of compression along the $[111]$ axis. The result also matches and explains the sixfold symmetric pile-up pattern faintly visible in Fig. 5(b) (SEM) and more clearly in Fig. 5(c) (AFM) around the indent.

It is worth noting that a second set of slip systems pertaining to the indented (111) plane, namely $(111)[01\bar{1}]$, $(111)[\bar{1}01]$, and $(111)[\bar{1}10]$, also contribute significantly to the total deformation when compared to the strain provided by the six dominant systems listed above. The fact that the orientation factors of these slip systems are zero in the table is of course due to the simplifying assumption of uniaxial compression that was made to calculate them. The amounts of shear listed in the table, in contrast, stem from the actual crystal plasticity finite element simulation, which imposes the correct boundary conditions locally. One special feature of this second group of slip systems is the high symmetry of the shear they contribute (two peaks of shear are visible on either side of the indenter axis).

Fig. 11 shows the distribution of the shear strains on all 12 slip systems as extracted from the crystal plasticity finite element simulation in the crystallographic $(11\bar{2})$ plane. As already observed from the top view in the (111) plane in Fig. 10, the dominant slip systems that essentially carry the strain in the $(11\bar{2})$ plane are the $(\bar{1}11)[101]$, $(\bar{1}11)[110]$, $(1\bar{1}1)[011]$, $(1\bar{1}1)[110]$, $(\bar{1}\bar{1}1)[011]$, and $(\bar{1}\bar{1}1)[101]$ systems. Minor shear activity can be observed on the $(111)[\bar{1}10]$ slip system. An equivalent shear contribution on two other systems, $(111)[01\bar{1}]$ and $(111)[\bar{1}01]$, also exists with a similar pattern as observed for the $(111)[\bar{1}10]$ slip system, but it cannot be seen in this crystallographic section (see the same systems also in Fig. 10). The shear distribution on the main slip systems $(111)[101]$, $(\bar{1}11)[110]$, $(1\bar{1}1)[011]$, $(1\bar{1}1)[110]$, $(\bar{1}\bar{1}1)[011]$, and $(\bar{1}\bar{1}1)[101]$ prevails also in the deeper regions far below the indenter tip where a change in the rotation sign was observed (Figs. 7 and 8).

The subdivision of the deformation pattern into six different characteristic regions suggested as a coarse subdivision in Fig. 8 is also helpful for discussing the sense and axis of the deformation-induced lattice rotations. Fig. 12 shows the lattice rotations about the crystallographic $[1\bar{1}0]$ axis presented in the $(11\bar{2})$ plane (Fig. 12(a)) and in the $(1\bar{1}0)$ plane (Fig. 12(b)) as predicted by the crystal plasticity finite element simulation. Both figures reveal the same rotation pattern as observed above, but they include the rotation direction. They both show one outer pair of zones with large lattice rotations tangent to the

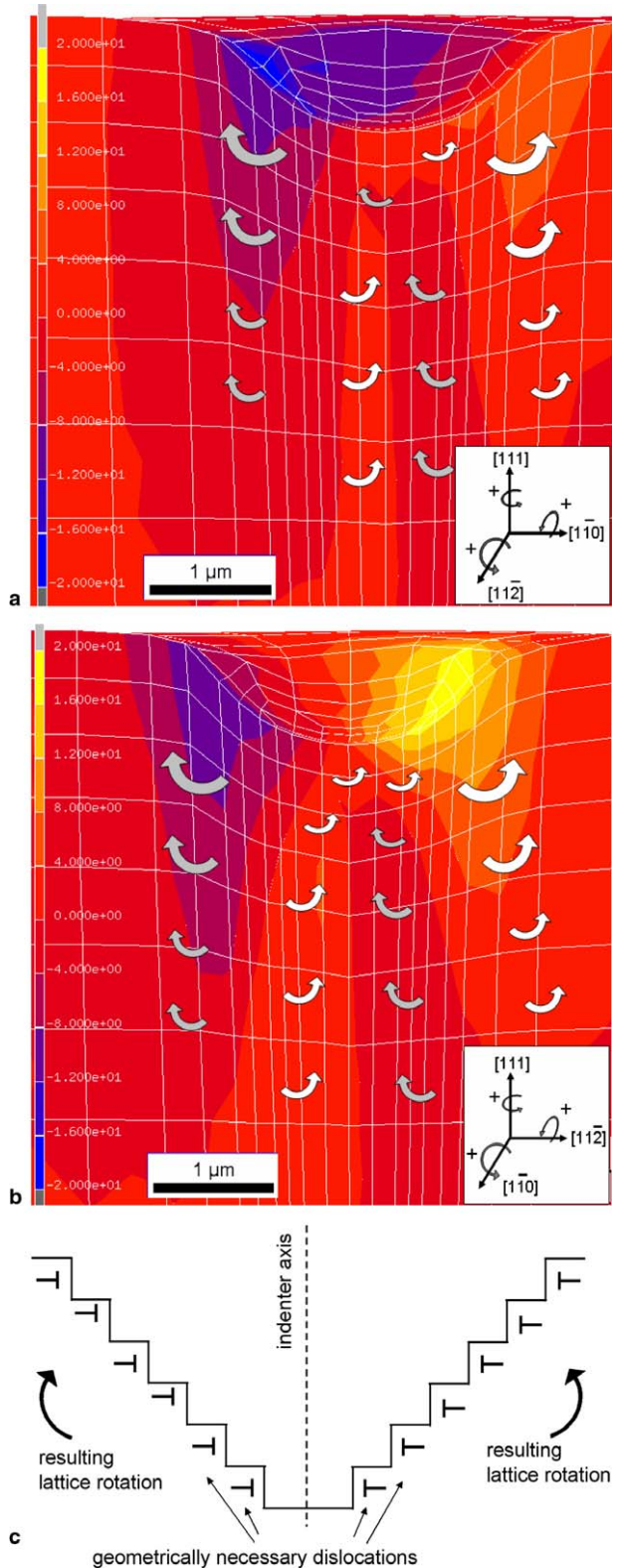


Fig. 12. 3D presentation of the simulated rotations (crystal plasticity finite element model) about the crystallographic $[1\bar{1}0]$ axis presented (a) in the $(11\bar{2})$ plane and (b) in the $(1\bar{1}0)$ plane. The planes presented are center planes, i.e., they both contain the indenter axis as a common zone axis. Scaling is the same for (a) and (b), i.e., from -20° to $+20^\circ$. (c) Schematic of the arrangement of the net geometrically necessary dislocations explaining the rotation direction in the outer tangent zones.

indenter surface and a second inner pair of zones with smaller lattice rotations close to the tip of the indenter. Different from the images discussed above which only revealed the absolute amount of the rotations, the simulation results in Fig. 12 show that in the tangent regime the $[1\bar{1}0]$ rotations point away from the indenter axis while in the inner zone the rotations point towards the indenter tip. This means that a transition regime exists between the outer and the inner deformation zone that is characterized by steep gradients and, in particular, by a change in the sign of the rotation direction.

The predicted profile with large rotations in the tangent zones (regions 2 and 5; large symbols in Fig. 12(a) and (b)) can be qualitatively understood in terms of the mass that must be displaced by the indenter from the bulk towards the surface. This large-scale displacement naturally creates the rotation angle confirmed by the 3D EBSD measurements (Fig. 13) and by the crystal plasticity simulations (Fig. 12). Another more detailed picture matching this tangent rotation field is the pattern of the net amount of geometrically necessary dislocations that has to be created for compatibility reasons in the tangent zones (Fig. 12(c)).

Although both approaches allow one to reconstruct basically the induced rotation pattern in the outer tangent zones (regions 2 and 5), the counter-rotations observed in the inner deformation zone close to the indenter axis are not a necessary consequence of this explanation.

Fig. 13 shows the rotation angles and the rotation directions in the $(11\bar{2})$ plane in scan 9 (see details in Table 1). This $(11\bar{2})$ section is placed 318 nm before the actual indenter tip. The upper row shows the rotations in that plane for the $[1\bar{1}0]$ rotation axis. The image on the left-hand side shows the $[1\bar{1}0]$ rotations scaled to $\pm 8^\circ$. The center image shows the same data scaled to $\pm 20^\circ$ for better comparison with the crystal plasticity finite element simulations on the right-hand side in the same row. The images in the bottom row show the rotations in the $(11\bar{2})$ plane in scan 9, but for the $[11\bar{2}]$ rotation axis. The image on the left-hand side shows the $[11\bar{2}]$ rotations scaled to $\pm 8^\circ$. The center image shows the same data scaled to $\pm 20^\circ$ for comparison with the simulations on the right-hand side in the same row.

The experimental maps of the rotation directions about the $[1\bar{1}0]$ and $[11\bar{2}]$ rotation axes (images on the left-hand

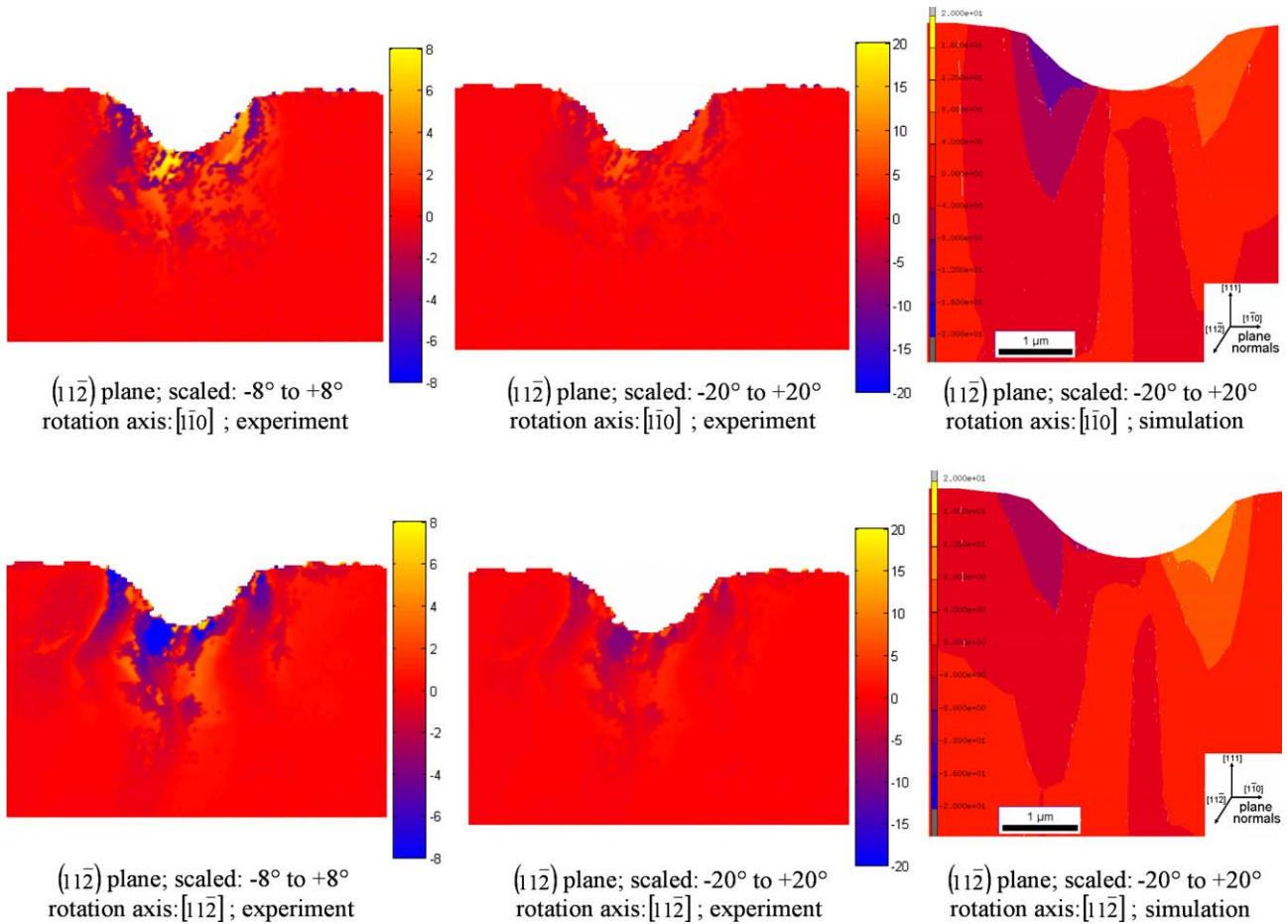


Fig. 13. Rotation angles and rotation directions in the $(11\bar{2})$ plane for scan 9 (see Table 1). This $(11\bar{2})$ section is 318 nm before the indenter tip. Top row: rotations in the $(11\bar{2})$ plane for the $[1\bar{1}0]$ rotation axis; left: $[1\bar{1}0]$ rotations scaled to $\pm 8^\circ$; center: same data scaled to $\pm 20^\circ$ for better comparison with the simulations; right: $[1\bar{1}0]$ rotations from crystal plasticity finite element simulations scaled to $\pm 20^\circ$. Bottom row: rotations in the $(11\bar{2})$ plane for the $[11\bar{2}]$ rotation axis; left: $[11\bar{2}]$ rotations scaled to $\pm 8^\circ$; center: same data scaled to $\pm 20^\circ$ for better comparison with the simulations; right: $[11\bar{2}]$ rotations from crystal plasticity finite element simulations scaled to $\pm 20^\circ$.

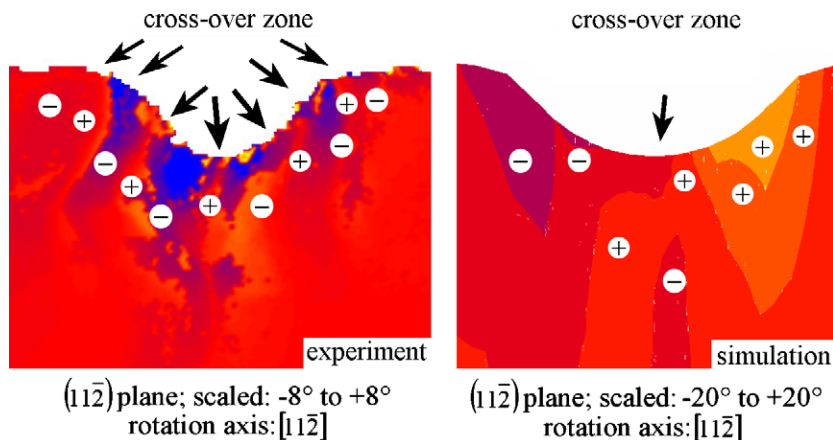


Fig. 14. Detail from Fig. 13 (bottom row; $[1\bar{1}\bar{2}]$ rotations in $(11\bar{2})$). The experimentally observed rotation pattern reveals a larger number of cross-over zones, where the sign of the rotation direction changes, when compared to the simulated results (note the difference in scaling). The signs indicate positive or negative rotation direction about the $[1\bar{1}\bar{2}]$ axis.

side in Fig. 13) basically show a similar deformation-induced rotation pattern as discussed above in the context of the absolute values of the deformation-induced rotations (Figs. 7–9). Also the experimentally observed patterns of the rotation directions reveal some basic similarities to those predicted by the crystal plasticity finite element method (images on the right-hand side in Fig. 13).

The possible reason for differences in the absolute magnitude of the rotation angles has been discussed above in terms of rim and edge effects. Besides this discrepancy, another main difference in the rotation direction field between experiment and simulation is that the experiments reveal a larger number of changes in the sign of the rotation direction along the contact zone between sample and indenter. This applies to both $[1\bar{1}0]$ and $[11\bar{2}]$ rotation axes. The difference is particularly apparent in the map of the $[1\bar{1}\bar{2}]$ rotations in the $(11\bar{2})$ plane scaled to $\pm 8^\circ$ (Fig. 13, bottom row, left). Fig. 14 shows a detail from Fig. 13 (bottom row; $[1\bar{1}\bar{2}]$ rotations in $(11\bar{2})$), which reveals that the experimentally observed rotation pattern shows a higher number of cross-over zones, where the sign of the rotation direction changes, when compared to the simulated results.

This applies in particular to the rapid changes in the sign of the rotation direction along the outer tangent zones. In these areas far away from the indenter tip the predicted rotation pattern also reveals gradients in the orientation field, but no frequent switches in sign are observed as in the experiments. This comparison shows that the viscoplastic crystal plasticity finite element simulation of nanoindentation presented in this work is obviously not capable of capturing the fine details of the deformation-induced rotation patterning observed in the experiment, at least not when it comes to the direction of rotation. The results shown in Fig. 9 (comparison of the equivalent strain field obtained from an isotropic simulation and from an anisotropic simulation) emphasize that the details of the deformation field must indeed be linked to crystallographic

aspects. Therefore, one may hope to obtain better simulation results with regard to steep gradients in the rotation field by incorporating more detailed constitutive descriptions in the crystal plasticity finite element model. Owing to our experimental data these model variants should in particular include two aspects. These are (i) gradient effects at the single slip level and (ii) dislocation patterning effects. The first aspect is obvious owing to the gradient mechanics associated with nanoindentation [8–11]. The second aspect seems to be of relevance because we assume that the pronounced patterning of the deformation-induced rotation field both in terms of the absolute orientation changes (e.g., Figs. 7 and 8) and of the rotation direction (Figs. 12–14) can only be fully understood by taking into account short-range dislocation patterning aspects, which would impede the formation of the smooth rotation fields predicted by our current simulations.

6. Conclusions

We have presented a 3D analysis of the deformation-induced rotation pattern below a conical nanoindent in a $[111]$ Cu single crystal using a 3D EBSD experimental method and a 3D elastic-viscoplastic crystal plasticity finite element method for the simulations. The main conclusions are as follows.

- A new microscopy approach using a combined SEM/FIB was for the first time applied to the 3D EBSD analysis of nanoindentation. Particular attention was placed on studying deformation-induced lattice rotations.
- The experiments and simulations reveal pronounced deformation-induced 3D patterning of the lattice rotations below and around the indent.
- The simulated pattern is characterized by an outer tangent zone with large rotations and an inner zone closer to the indenter axis with smaller rotations. The rotations in the tangent regime point away from the indenter axis

- while in the inner zone the rotations point towards the indenter tip. This leads to a transition regime between the outer and the inner rotation zone that is characterized by steep orientation gradients and a change in the sign of the rotation direction (cross-over zone).
- The experimentally observed pattern is characterized by similar features in the overall rotation distribution to the simulations. In particular, the crystal plasticity finite element simulations reveal a similar pattern formation in terms of the absolute rotation rates as the experiments. However, when analyzing details of the axis–angle relationship of the rotations the experiments clearly reveal a higher frequency of cross-over zones, where the sign of the rotation direction changes, than the simulations. Some of these cross-over zones are not captured at all by the simulations.
 - The crystal plasticity finite element simulations provide details of the shear distribution in the deformation zone on the different slip systems. The main shear contribution is carried by those six slip systems that would also be expected from a maximum orientation factor analysis for the simplifying case of uniaxial compression along ⟨111⟩.
 - The isotropic (J2 flow criterion) finite element simulations only reveal an outer pronounced deformation zone, but the inner deformation zone is not predicted, which underlines its crystallographic origin. This observation emphasizes that corresponding simulations of nanoindentation must take the crystallographic nature of the plastic slip into account.

Acknowledgements

We gratefully acknowledge the kind financial support of the Deutscher Akademischer Austauschdienst (DAAD, German Academic Exchange Service; www.daad.org) for N.Z. and of the Alexander von Humboldt Stiftung (AvH, Alexander von Humboldt Foundation, www.humboldt-foundation.de) for R.N.S. The authors are also grateful to the Deutsche Forschungsgemeinschaft (DFG, German Research Foundation, www.dfg.de), which funded this study under the framework of the Gottfried Wilhelm Leibniz award. Detailed discussions on this topic during the last two years with Dr. Ben Larson and Dr. Wenge Yang from the Oak Ridge National Laboratory, USA, are gratefully acknowledged.

References

- [1] Pharr GM, Oliver WC, Brotzen FR. *J Mater Res* 1992;7:613–7.
- [2] Oliver WC, Pharr GM. *J Mater Res* 1992;7:1564–83.
- [3] Fischer-Cripps AC. Nanoindentation. Springer mechanical engineering series. 2nd ed. Berlin: Springer; 2004.
- [4] Nix WD. *Mater Sci Eng A* 1997;234–236:37–44.
- [5] Choi Y, Van Vliet KJ, Li J, Suresh S. *J Appl Phys* 2003;94:6050–8.
- [6] Suresh S, Giannakopoulos AE. *Acta Mater* 1998;46:5755–67.
- [7] Gouldstone A, Koh H-J, Zeng K-Y, Giannakopoulos AE, Suresh S. *Acta Mater* 2000;48:2277–95.
- [8] Fleck NA, Muller GM, Ashby MF, Hutchinson JW. *Acta Metall Mater* 1994;42:475–87.
- [9] Fleck NA, Otoyo H, Needleman A. *Int J Solids Struct* 1992;26: 1613–36.
- [10] Gao H, Huang Y, Nix WD, Hutchinson JW. *J Mech Phys Solids* 1999;47:1239–636.
- [11] Evers LP, Parks DM, Brekelmans WAM, Geers MGD. *J Mech Phys Solids* 2002;50:2403–24.
- [12] Viswanathan GB, Lee E, Maher DM, Banerjee S, Fraser HL. *Acta Mater* 2005;53:5101–15.
- [13] Groeber M, Haley B, Uchic M, Ghosh S. In: Ghosh S, Castro J, Lee JK, editors. Proceedings of NUMIFORM. AIP Publishers; 2004. p. 1712.
- [14] Zaefferer S. *Mater Sci Forum* 2005;495–497:3–12.
- [15] Konrad J, Zaefferer S, Raabe D. *Acta Mater* 2006; in press.
- [16] Raabe D, Klose P, Engl B, Imlau KP, Friedel F, Roters F. *Adv Eng Mater* 2002;4:169–80.
- [17] Raabe D, Roters F. *Int J Plasticity* 2004;20:339–61.
- [18] Raabe D, Sachtleber M, Zhao Z, Roters F, Zaefferer S. *Acta Mater* 2001;49:3433–41.
- [19] Sachtleber M, Zhao Z, Raabe D. *Mater Sci Eng A* 2002;336:81–7.
- [20] Yang W, Larson BC, Pharr GM, Ice GE, Tischler JZ. *MRS Symp Proc* 2003;779:W5.34.1.
- [21] Larson BC, Yang W, Ice GE, Budai JD, Tischler JZ. *Nature* 2002;415:887–90.
- [22] Barabash RI, Ice GE, Larson BC, Pharr GM, Chung KS, Yang W. *Appl Phys Lett* 2001;79:749.
- [23] Ice GE, Larson BC. *Adv Eng Mater* 2000;2:643.
- [24] Larson BC, personal communication and lectures at the Plasticity 2005 conference in Kauai (Hawaii, USA) and at the MRS 2005 spring conference in San Francisco.
- [25] Wang Y, Raabe D, Klüber C, Roters F. *Acta Mater* 2004;52:2229–38.
- [26] Shilkrot LE, Curtin WA, Miller RE. *J Mech Phys Solids* 2002;50: 2085–2106.
- [27] Miller RE, Shilkrot LE, Curtin WA. *Acta Mater* 2004;52:271–84.
- [28] Smith GS, Tadmor EB, Bernstein N, Kaxiras E. *Acta Mater* 2001;49:4089–101.
- [29] Bolshakov A, Pharr GM. *J Mater Res* 1998;13:1049–58.
- [30] Fifel MC, Robertson CF, Canova GR, Boulanger L. *Acta Mater* 1998;46:6183–94.
- [31] Durst K, Göken M, Pharr GM. *Z Metallkd* 2002;93:857–61.
- [32] Park YJ, Pharr GM. *Thin Solid Films* 2004;447:246–50.
- [33] Lichinchi M, Lenardi C, Haupt J, Vitali R. *Thin Solid Films* 1998;312:240–8.
- [34] Durst K, Backes B, Göken M. *Scripta Mater* 2005;52:1093–7.
- [35] Durst K, Göken M, Vehoff H. *J Mater Res* 2004;19:85–93.
- [36] Li J, Van Vliet K, Ting Z, Yip S, Suresh S. *Nature* 2002;418: 307–310.
- [37] Van Vliet K, Li J, Ting Z, Yip S, Suresh S. *Phys Rev B* 2003;67:104105.
- [38] Kalidindi SR, Bronkhorst CA, Anand L. *J Mech Phys Solids* 1992;40:537–69.
- [39] Kalidindi SR, Anand L. *Metall Trans A* 1993;24:989–92.
- [40] MSC. Marc user manual, vol. D. MSC Software Corporation; 2001.
- [41] Ma A, Roters F, Raabe D. *Acta Mater* 2006; in press.
- [42] Raabe D, Zhao Z, Park SJ, Roters F. *Acta Mater* 2002;50:421–40.
- [43] Meissonnier FT, Busso EP, O'Dowd NP. *Int J Plasticity* 2001;17:601–40.
- [44] Arsenlis A, Parks DM, Becker R, Bulatov V. *J Mech Phys Solids* 2004;52:1213–46.
- [45] Evers LP, Brekelmans WAM, Geers MGD. *J Mech Phys Solids* 2004;52:2379–401.



Pergamon

Acta Materialia 50 (2002) 421–440



www.elsevier.com/locate/actamat

Theory of orientation gradients in plastically strained crystals

D. Raabe ^{a,*}, Z. Zhao ^a, S.-J. Park ^b, F. Roters ^a

^a Max-Planck-Institut für Eisenforschung, Max-Planck-Str. 1, 40237 Düsseldorf, Germany

^b Department of Materials Science and Engineering, Seoul National University, Seoul, South Korea

Received 13 December 2000; received in revised form 14 August 2001; accepted 14 August 2001

Abstract

We suggest a theory of in-grain orientation gradients in plastically strained metals. It is an approach to explain why initially uniformly oriented crystals can—under gradient-free external loadings—build up in-grain orientation gradients during plastic deformation and how this phenomenon depends on intrinsic factors (crystal orientation) and extrinsic factors (neighbor grains).

The intrinsic origin (orientation dependence) of in-grain orientation gradients is investigated by quantifying the change in crystal reorientation upon small changes in initial orientation. This part of the approach is formulated by applying a divergence operator to reorientation rate vector fields (in the present paper calculated by using strain-rate homogenization Taylor–Bishop–Hill theory). The obtained scalar divergence function (but not the reorientation vector field itself) quantifies the kinematic stability of grains under homogeneous boundary conditions as a function of their orientation. Positive divergence (source in the reorientation rate vector field) characterizes orientations with diverging non-zero reorientation rates which are kinematically unstable and prone to build up orientation gradients. Zero divergence indicates orientations with reorientation rate identity with the surrounding orientations which are not prone to build up orientation gradients. Negative divergence (sink in the reorientation rate vector field) characterizes orientations with converging non-zero reorientation rates which are kinematically stable and not prone to build up orientation gradients. Corresponding results obtained by use of a crystal plasticity finite element formulation are in good agreement with the reorientation field divergence function derived by homogenization theory.

The extrinsic origin of in-grain orientation gradients (influence of grain–neighbor interaction) is addressed using a crystal plasticity finite element bicrystal model. The simulations show that a significant dependence of orientation gradients on the neighbor crystals occurs for grains with high positive divergence. The build-up of orientation gradients in grains with close to zero or negative divergence is in body centered cubic crystals less sensitive to the presence of neighbor orientations than in face centered cubic crystals (Goss and cube orientation). © 2002 Published by Elsevier Science Ltd on behalf of Acta Materialia Inc.

Keywords: Texture; Theory & modeling; Structural behaviour; Mesostructure

* Corresponding author. Tel.: +49-211-6792-340/278; fax: +49-211-6792-333.

E-mail address: raabe@mpie.de (D. Raabe).

1. Introduction

1.1. Phenomenology and terminology of orientation gradients

Plastic deformation of poly- and single crystals can lead to individual orientation changes of the grains and, as a consequence, to the development of deformation textures. However, initially uniformly orientated crystals do often not rotate as units but subdivide into portions with a range of different orientations. We refer to this phenomenon, which was already in 1940 observed and discussed by Barrett and Levenson [1], to the formation of orientation gradients, meaning spatial continuous or discontinuous variations of crystal orientation within the original grain borders.

Orientation gradients do not only form in the trivial case of externally imposed strain gradients (e.g. bulk torsion or rolling operations with non-zero friction) but also under gradient-free external loadings. They are in the literature also referred to as localized orientation gradients [2], grain fragmentation [3], deformation banding [4–6] orientation splitting [7], grain subdivision [4,8], or lattice curvature [8–11].

Beaudoin et al. [2], Raabe [3], Leffers [4], and Lee et al. [5,6] provided theoretical approaches to explain the formation of a non-uniform orientation spread within a grain. Using many elements per grain Beaudoin et al. [2] observed in their 3D crystal plasticity simulations heterogeneous deformations within individual grains which lead to the development of domains which were separated by boundaries of high misorientation. Similar investigations using crystal plasticity finite element methods were also conducted by other authors (e.g. [1,12–21]). Raabe [3], Leffers [4], and Lee et al. [5,6] gave arguments for the formation of orientation gradients on the basis of modified homogenization models.

The term lattice curvature was typically used by authors who underlined the mechanical aspects of continuous in-grain orientation gradients [8–10], mainly referring to the formation of geometrically necessary dislocations.

Quantitative experimental work on this subject

was essentially conducted using orientation imaging techniques via analysis of Kikuchi diffraction patterns in the scanning electron microscope (SEM) (e.g. [22–38]) and in the transmission electron microscope (TEM) (e.g. [37–41] [42–48]). Earlier experimental work about orientation gradients was based on analysis of X-ray Bragg diffraction pole figures, Kossel diffraction patterns, electron channeling patterns, etch pits, and orientation sensitive etching methods.¹

The above described phenomena can occur in single crystals as well as in grains of polycrystals. From the quoted literature some common features of in-grain orientation gradient phenomena can be identified: Orientation gradients were found

1. to occur under homogeneous boundary conditions, i.e. they take place even if no gradients are exerted by external loading (the internal load is usually less well known) (e.g. [2,6,11,23]);
2. to depend on the strain path (e.g. [11]);
3. in many cases to depend on the initial orientation and on the orientation path of the strained crystal (e.g. [3,11,19,24,30,31,33]);
4. in many cases to depend on the neighbor grains (e.g. [1,2,12–19]);
5. to be closely connected with a change in glide system activity in the different in-grain portions with different orientations (e.g. [11,24,41,47,48]) (such in-grain domains of different orientation have in these works been referred to as *differently deforming regions*);
6. in many cases to occur already at low strains and build up further throughout deformation (e.g. [1,3,7,24]);
7. to undergo continued refinement in the spatial scale of subdivision with increasing total strain and to occur at different spatial scales within the same crystal (e.g. [12,24,30–32]).

In order to avoid confusion we will use the expression *orientation gradient* (here always meaning *in-grain* orientation gradient) as a rep-

¹ Since this is no overview paper on experimental methods, we quote only a selected set of papers and refer the interested reader to the RISØ-overview of Hughes [47].

representative term for the various phenomena listed above in the ensuing sections of the paper.

1.2. Aims of an orientation gradient theory

Besides the basic scientific challenge to elucidate the origin of orientation gradients, five main practical reasons can be given for the formulation of an orientation gradient theory. First, due to the complexity of existing results and details observed so far theory is required to better understand and structure the underlying principles of orientation gradients. Second, the key idea of our approach, namely the use of the reorientation rate vector field divergence as an intrinsic measure of orientation gradients can be formulated as a concise scalar function in orientation space using for instance spherical harmonics. Third, our formulation is tractable for subsequent integration into other frameworks dealing with the orientation dependence of recrystallization or strain hardening phenomena. Fourth, theoretical concepts help to separate important from less important microstructural information in the context of orientation gradients. Fifth, complete experimental instead of theoretical characterization of in-grain orientation gradient phenomena throughout orientation space is not possible due to the huge number of crystal orientations and boundary conditions to be considered.

1.3. Basic theoretical approach

The present work aims at explaining why uniform crystals can build up orientation gradients during plastic deformation and how this phenomenon depends on crystal orientation (*intrinsic* dependence) and on the interaction with neighbor grains (*extrinsic* dependence). The intrinsic origin of orientation gradients is investigated on the basis of the geometrical stability of grains with respect to small changes in starting orientation. The orientation dependence of orientation gradients is in the intrinsic approach, i.e. without consideration of neighbor interaction, formulated by applying a divergence operator to reorientation rate vector fields in orientation space. This scalar divergence function then quantifies stability of grains under homogeneous boundary conditions as a function of

orientation and strain state. Extrinsic reasons for orientation gradients are addressed by calculating the influence of grain–neighbor interaction directly using a crystal plasticity finite element approach.

1.4. Plan of the paper

The plan of the paper is as follows: In Section 2 we introduce the reorientation field divergence as a scalar function in Euler space for quantifying the intrinsic origin of orientation gradients and formulate it for fcc and bcc crystals for the plane strain case. In Section 3 we check the consistency of these predictions by use of crystal plasticity finite element simulations. In Section 4 we investigate the influence of neighborhood on the formation of orientation gradients using a crystal plasticity finite element bicrystal model. Section 5 provides a discussion of the predictions, compares the findings with experimental data from the literature, and explains differences found between the fcc and the bcc structure.

2. Divergence of crystal reorientation fields as intrinsic measure for orientation gradients

2.1. Concept and calculation method

The theoretical approach we suggest in this paper for the explanation of the formation of in-grain orientation gradients under homogeneous external boundary conditions is based on strain rate homogenization modeling and on crystal plasticity finite element modeling. It aims at explaining why initially uniformly oriented crystals can under homogeneous boundary conditions form in-grain orientation gradients during plastic straining and how this phenomenon depends on crystal orientation (*intrinsic* dependence) and on grain–neighbor interaction (*extrinsic* dependence). In contrast to some of the above quoted works the present investigation does not make any predictions about the spatial arrangement, size, or shape of in-grain orientation gradients but provides a more general geometrical approach for calculating what the potential tendency of a particular grain is to form orientation gradients within its original

borders as a function of its initial orientation, its neighbor grains, and the strain state.

The intrinsic origin of orientation gradients is investigated on the basis of the kinematic stability of grains with respect to small changes in starting orientation. This follows a suggestion of Kocks [49] who stated that orientation gradient effects may proceed from a variation in slip system activation throughout a grain entailing microscopic initial variation in slip and hence in the plastic rotation leading to local domains with different orientation. We will extend this approach and show that the tendency to build up orientation gradients can be formulated in terms of the *orientation dependence* of such in-grain variations in slip system selection and the resulting in-grain spread of the reorientation rate. A consequence of this model is that one can quantify the orientation dependence of the phenomenon by calculating the dependence of reorientation rate upon tiny changes in the initial host orientation.

It will be shown that it is a strong function of the grain orientation itself whether such initial variations entail in-grain orientation gradients during plastic straining or not. As was found earlier and as will be shown below the reorientation rate vector *itself* is not an adequate measure of future orientation gradients.

The orientation dependence of in-grain orientation gradients is in the intrinsic approach, i.e. without consideration of neighbor interaction, formulated by applying a divergence operator to reorientation rate vector fields in orientation space. Such fields are generated by mapping the reorientation rate vectors obtained (in the present case) from strain-rate homogenization theory for each orientation throughout orientation space (see e.g. [11,49–51]). This scalar divergence function then quantifies kinematic stability of grains under homogeneous boundary conditions as a function of orientation and strain state.

It is obvious that such a divergence analysis of reorientation paths is a general approach for quantifying orientational instabilities. It should be noted though that the analysis of orientation stability is not necessarily a non-linear problem, since many homogenization models are linear. However, the here suggested divergence approach for the analy-

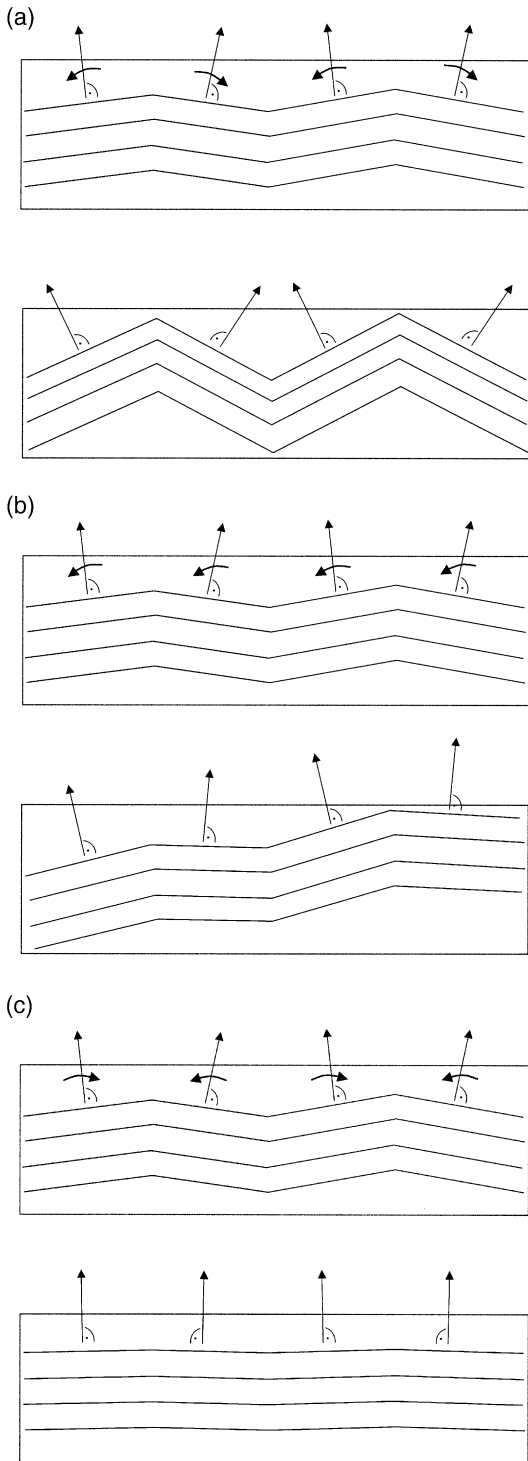
sis of orientational stability is generally independent on the underlying deformation model or experiment. Its starting point is simply a theoretically derived or experimentally observed reorientation field in orientation space (not in real space).

Fig. 1 describes the principle of our approach (intrinsic case). The size of the different grain regions is purely schematic. Fig. 1(a) shows a grain in the initial state with some small initial orientation variation and after straining with a larger orientation variation. This is a case where the initial orientation variation becomes stronger during straining, due to different slip system activation in the different regions. This is a case where reorientation vectors of different regions in the same grain are non-zero and point in opposite directions (arrows). Mathematically this corresponds to a positive divergence of the reorientation field (source in the reorientation vector field) characterizing kinematically unstable orientations which have an intrinsic tendency to build up orientation gradients.

Fig. 1(b) shows a case where reorientation vectors of different regions in the same grain are non-zero and identical. This means the entire grain rotates homogeneously with the same reorientation vector. In this case the initial orientation fluctuation remains unchanged, but the bulk grain undergoes bulk reorientation. Mathematically this corresponds to zero divergence of the reorientation field (reorientation identity of the different orientation segments) characterizing orientations which do not have an intrinsic tendency to build up orientation gradients.

Fig. 1(c) shows a case where reorientation vectors of different regions in the same grain are non-zero and point towards each other, or more general, towards the same stable orientation. In this case the initial orientation fluctuation becomes smaller. Mathematically this corresponds to negative divergence of the reorientation field (sink in the reorientation vector field) indicating orientations which do not have an intrinsic tendency to build up orientation gradients.

For obtaining an intrinsic function of grain fragmentation which depends solely on crystal orientation and which is independent of neighbor grain interaction we calculated reorientation fields by



Taylor–Bishop–Hill strain-rate homogenization theory. Calculations were conducted for body centered cubic (bcc) crystal structure with 12 $\{110\} < \bar{1}\bar{1}1 >$ slip systems and 48 slip systems ($12 \times \{110\} < \bar{1}\bar{1}1 >$, $12 \times \{1\bar{1}2\} < \bar{1}\bar{1}1 >$, $24 \times \{12\bar{3}\} < \bar{1}\bar{1}1 >$) as well as for face centered cubic (fcc) crystal structure with $12 \times \{1\bar{1}1\} < \bar{1}10 >$ slip systems and 18 slip systems ($12 \times \{1\bar{1}1\} < \bar{1}10 >$, $6 \times \{1\bar{1}0\} < \bar{1}10 >$), exerting homogeneous external plane strain conditions with relaxation of longitudinal and transverse shear constraints at the grain level (pancake model) (see overviews in [55–57]). Finally we applied a divergence operator to the obtained reorientation vector field. The resulting scalar divergence function was developed in the form of spherical harmonics using a series expansion degree of 34 and then plotted in orientation space.

Since the approach suggested in this paper essentially takes a geometrical view at the development of crystal orientations it is only capable of addressing observations (1)–(6). Observations (7) cannot be explained in the present framework since this would require to include dislocation dynamics

Fig. 1. (a) Grain in the initial state with some small initial orientation variation and after straining with a larger orientation variation. This is a case where the initial orientation variation becomes stronger during straining, due to different slip system activation in the different regions. This is a case where reorientation vectors of different regions in the same grain are non-zero and point in opposite directions (arrows). Mathematically this corresponds to a positive divergence of the reorientation field (source in the reorientation vector field) indicating orientations which have a tendency to form orientation gradients. (b) Case where reorientation vectors of different regions in the same grain are non-zero and identical. The entire grain rotates homogeneously with the same reorientation vector. In this case the initial orientation fluctuation remains unchanged, but the grain undergoes bulk reorientation. Mathematically this corresponds to zero divergence of the reorientation field (reorientation identity with the surrounding orientations) indicating orientations which do not have a tendency to form orientation gradients. (c) Case where reorientation vectors of different regions in the same grain are non-zero and point towards each other, or more general, towards the same stable orientation. In this case the initial orientation fluctuation becomes smaller. Mathematically this corresponds to negative divergence of the reorientation field (sink in the reorientation vector field) indicating orientations which do not have a tendency to form orientation gradients.

based effects [9,52–54] which are not part of this investigation.² On the other hand it is likely that, due to the dominance of the reorientation field for the formation of orientation gradients [11,50,51], explicit incorporation of dislocation dynamics effects would lead to an overall damping force, i.e. to slower rotations, rather than to entirely different results. In other words, this paper concentrates on the *kinematic origin* of orientation gradients, i.e. on the role of changes in slip system selection and the resulting reorientation changes as a function of orientation.

2.2. Results for body centered cubic crystal structure (intrinsic, reorientation field divergence)

Fig. 2 shows the reorientation field divergence of a bcc polycrystal with 12 slip systems, derived by using the pancake model. The figure is in the form of φ_1 =constant sections in Euler-space to show the divergence along relevant plane strain deformation and shear texture fibers and components.³ The intensity lines show areas with positive divergence above +1. The diagram shows high divergence around the rotated cube ($\{001\}<110>$, $\varphi_1 = 0^\circ$, $\phi = 0^\circ$, $\varphi_2 = 45^\circ$) and the Goss ($\{011\}<100>$, $\varphi_1 = 0^\circ$, $\phi = 45^\circ$, $\varphi_2 = 0^\circ$) texture components as well as along the ζ -fiber. This is only in part in accord with experimental experience. Whilst orientations around Goss and

² Attempts were made to calculate microtextures from discrete dislocation dynamics [54]. However, such approaches are computationally too time-consuming for formulating a theory of orientation gradients.

³ For bcc materials these are the α_{bcc} -fiber (fiber axis $<110>$ parallel to the rolling direction including major components $\{001\}<110>$, $\{112\}<110>$, and $\{111\}<110>$), γ -fiber (fiber axis $<111>$ parallel to the normal direction including major components $\{111\}<110>$ and $\{111\}<112>$), η -fiber (fiber axis $<001>$ parallel to the rolling direction including major components $\{001\}<100>$ and $\{011\}<100>$), ζ -fiber (fiber axis $<011>$ parallel to the normal direction including major components $\{011\}<100>$, $\{011\}<211>$, $\{011\}<111>$, and $\{011\}<011>$), ϵ -fiber (fiber axis $<011>$ parallel to the transverse direction including major components $\{001\}<110>$, $\{112\}<111>$, $\{111\}<112>$, and $\{011\}<100>$), and θ -fiber (fiber axis $<001>$ parallel to the normal direction including major components $\{001\}<100>$ and $\{001\}<110>$).

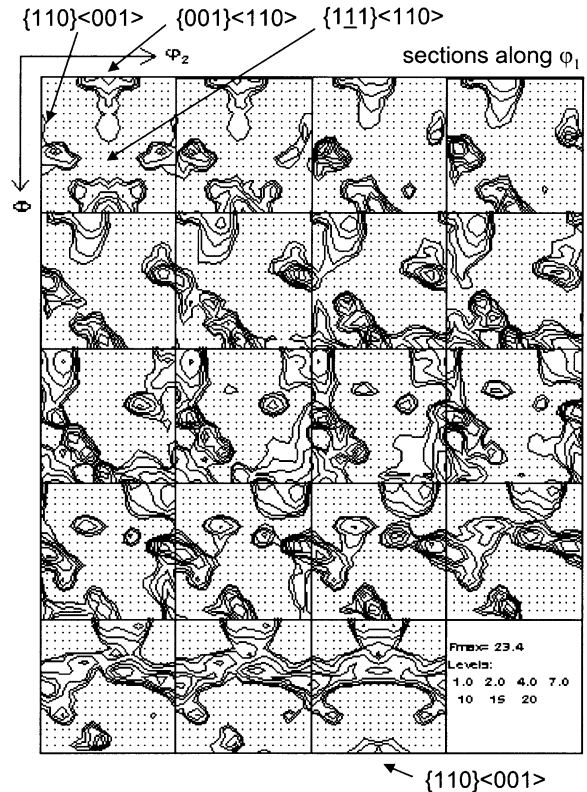


Fig. 2. Reorientation rate vector field divergence of a bcc polycrystal with 12 slip systems; pancake model; φ_1 =constant sections in Euler space; intensity lines show areas with divergence above 1.

the ζ -fiber are indeed known to form strong orientation gradients under plane strain conditions, the rotated cube orientation $\{001\}<110>$ is known as a very stable component without building up pronounced in-grain orientation gradients during plane strain deformation (see experiments in [30,31,33,58]). Section 5 will provide a more detailed comparison with experimental data.

Fig. 3(a) shows the reorientation field divergence for 48 slip systems (bcc, pancake model). It reveals high divergence around the Goss component and an absolute maximum at the RZ_{bcc} component ($\varphi_1 = 34^\circ$, $\phi = 84^\circ$, $\varphi_2 = 45^\circ$). Fig. 3(b) shows in the form of a $\varphi_2 = 45^\circ$ -section some details of the divergence between 0.1 and 1. It can be seen that some orientations around the γ -fiber and on the α -fiber reveal small positive divergence.

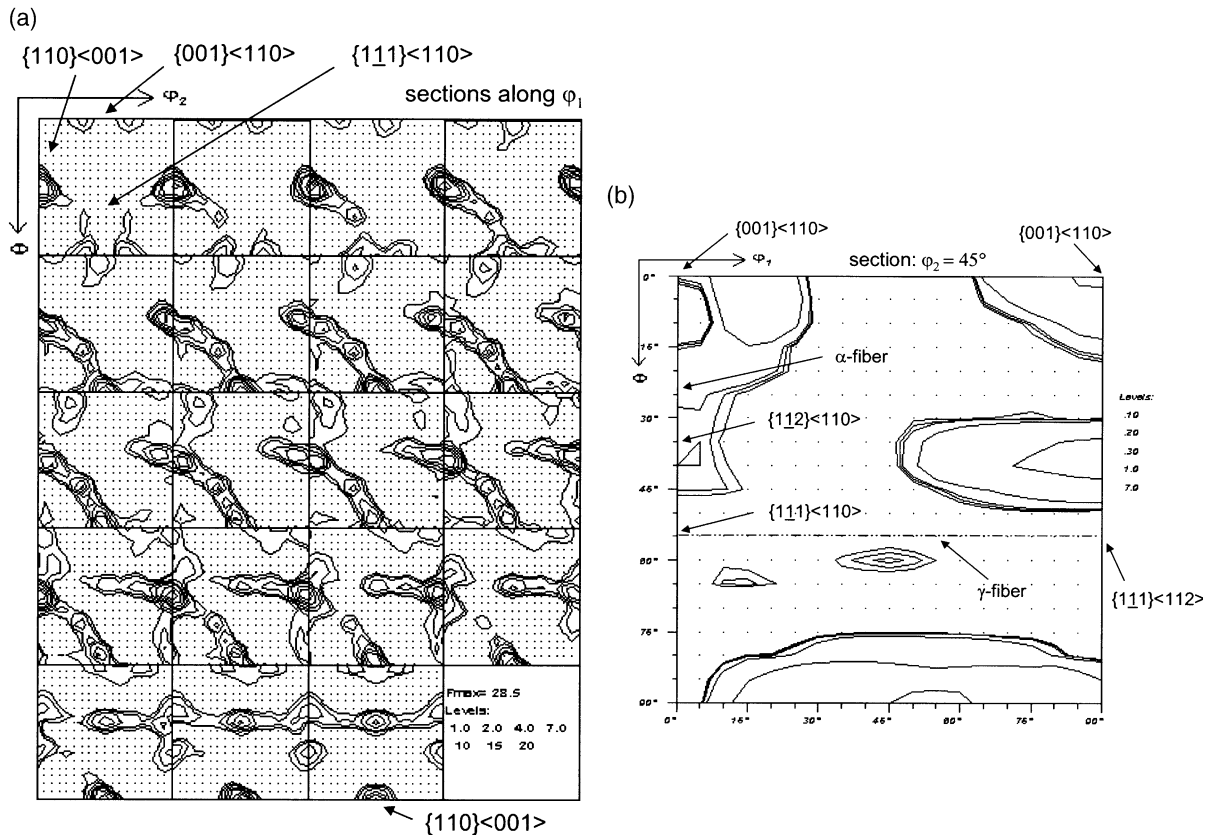


Fig. 3. (a) Reorientation rate vector field divergence of a bcc polycrystal with 48 slip systems; pancake model; ϕ_1 =constant sections in Euler space; intensity lines show areas with divergence above +1. (b) Details of the divergence function shown in (a) between 0.1 and 1.

2.3. Results for face centered cubic crystal structure (intrinsic, reorientation field divergence)

Fig. 4 shows the reorientation field divergence of a fcc polycrystal with 12 slip systems, calculated by using the pancake model. The figure is in the form of ϕ_2 =constant sections to show relevant components of typical fcc plane strain deformation and shear textures.⁴

⁴ For fcc materials these are the α_{fcc} -fiber (fiber axis $<011>$ parallel to the normal direction including major components $\{011\}<100>$, $\{011\}<2\bar{1}1>$, $\{011\}<1\bar{1}1>$, and $\{011\}<0\bar{1}1>$) and the β -skeleton line (less symmetric fiber including major components $\{211\}<111>$ (Cu-component), $\sim\{123\}<634>$ (S-component) and $\{011\}<211>$ (Brass-component)).

The results show strong divergence close to the $\{001\}<110>$ component. This is equivalent to the divergence observed around the Goss component for the bcc structure because of the 90° rotation relationship about the transverse direction between the fcc and the primary 12 bcc slip systems. Significant divergence appears in the vicinity of the Brass component ($\{110\}<112>$) and towards higher angles on the α_{fcc} -fiber. According to the predictions the Goss and the cube orientation should reveal a relatively weak intrinsic tendency to build up orientation gradients. This is in contradiction to experimental observations. In the following sections we will show, that these deviations are essentially due to the influence of the neighbor grains which are not included in this section. Calculations on the basis of 18 slip systems reveal

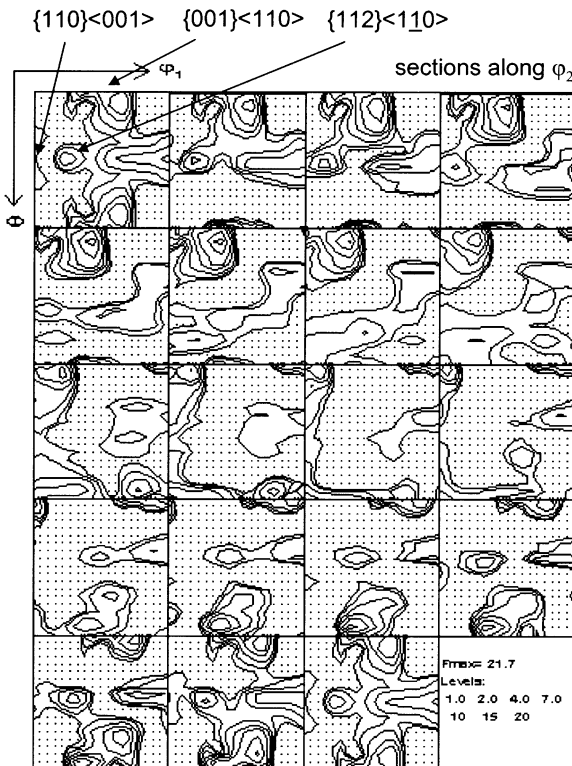


Fig. 4. Reorientation rate vector field divergence of a fcc polycrystal with 12 slip systems; pancake model; φ_2 =constant sections in Euler space; intensity lines show areas with divergence above +1.

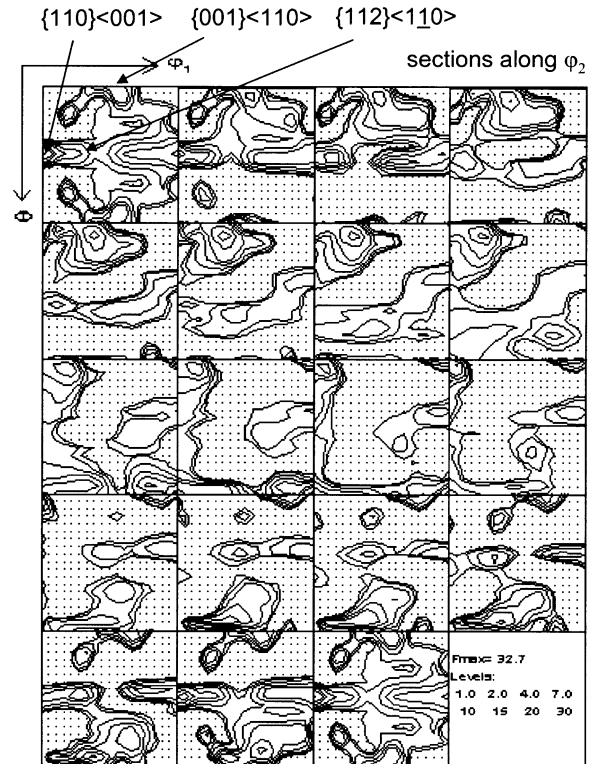


Fig. 5. Reorientation rate vector field divergence of a fcc polycrystal with 18 slip systems; pancake model; φ_2 =constant sections in Euler space; intensity lines show areas with divergence above +1.

similar divergence behavior (Fig. 5). The maximum on the α_{fcc} -fiber is shifted from the Brass towards the Goss component.

3. Verification of the reorientation field divergence theory using a crystal plasticity finite element method

3.1. Concept and calculation method

The results obtained from the divergence calculations presented in the preceding section are influenced by the homogenization model used for the calculation of the reorientation fields. Various approaches can be used for the calculation of the reorientation field, for instance crystal plasticity

finite element, Taylor–Bishop–Hill, or self-consistent models.

This section presents crystal plasticity finite element calculations showing predictions of orientation gradients of selected single crystal orientations under external (not necessarily internal) plane strain boundary conditions. The results are compared with the predictions made in the previous section. In order to simulate external plane strain conditions the free surface of the crystals was constrained to preserve orthorhombic symmetry during plastic straining.

Mesh configuration was conducted via ABAQUS/CAE [59] using a 3-dimensional linear element type with eight nodes and eight integration points. The total number of elements was 512 ($8 \times 8 \times 8$). An implicit crystal plasticity procedure proposed by Kalidindi et al. [60] was implemented

and used for the time integration of the constitutive equations. Calculations were carried out using the finite element program ABAQUS in conjunction with the user defined material subroutine UMAT [59]. Simulations were based on 48 slip systems ($12 \times \{110\} <111>$, $12 \times \{112\} <111>$, $24 \times \{123\} <111>$) in case of bcc crystals and on 12 $\{111\} <110>$ slip systems in case of fcc crystals. For selected bcc and fcc grain orientations plane strain compression to 50% thickness reduction was simulated (thickness reduction is given as $\Delta d/d_0$, where d is the thickness).

3.2. Results for body centered cubic crystal structure (intrinsic, FEM)

Fig. 6(a) shows the accumulated misorientations in gray scale coding (with light values indicating large misorientations) for a bcc grain with initial rotated cube orientation, $\{001\} <110>$, after 50% plane strain deformation. The projected orientation distribution is given in the form of $\{111\}$ pole figures. The open squares show the initial orientation (which was the same at all integration points). The black dots show the orientations of all integration points after deformation. It is remarkable, that neither bulk rotation nor orientation gradients occur. This behavior corresponds to the case described in Fig. 1(c). The prediction is in very good accord with the reorientation divergence model using 48 slip systems [Fig. 3(a,b)].

Fig. 6(b) shows the results for the inverse Brass component ($\{112\} <110>$, $\varphi_1 = 0^\circ$, $\phi = 35^\circ$, $\varphi_2 = 45^\circ$). It can be seen that the initially uniform grain has split up into two different orientation

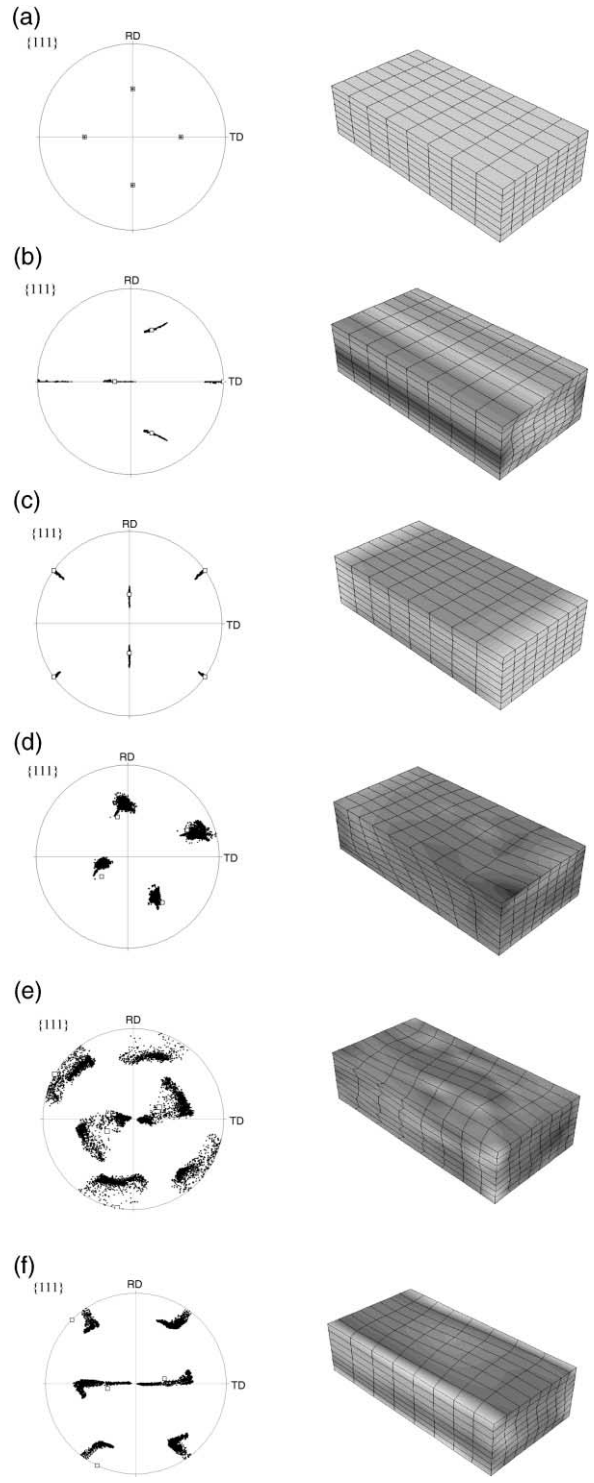


Fig. 6. Accumulated misorientations in gray scale coding (light values indicate large misorientations) for a bcc grain (48 slip systems) after 50% plane strain deformation. The texture is given in the form of $\{111\}$ pole figures. The open square shows the initial orientation (which was the same at all integration points) and the black dots show the orientations after deformation. The starting orientations were (a) 45° rotated cube orientation ($\varphi_1 = 0^\circ$, $\phi = 0^\circ$, $\varphi_2 = 45^\circ$); (b) inverse Brass orientation ($\varphi_1 = 0^\circ$, $\phi = 35^\circ$, $\varphi_2 = 45^\circ$); (c) Goss orientation ($\varphi_1 = 0^\circ$, $\phi = 45^\circ$, $\varphi_2 = 0^\circ$); (d) less symmetric orientation ($\varphi_1 = 0^\circ$, $\phi = 18^\circ$, $\varphi_2 = 73^\circ$); (e) RZ_{bcc} orientation ($\varphi_1 = 34^\circ$, $\phi = 84^\circ$, $\varphi_2 = 45^\circ$); (f) 90° rotated Goss orientation ($\varphi_1 = 0^\circ$, $\phi = 90^\circ$, $\varphi_2 = 45^\circ$).

branches, related to each other by a rotation about the longitudinal direction, corresponding to a crystal $\langle 110 \rangle$ axis. The mutually misoriented volume portions are connected by orientational transition bands. This behavior corresponds to the case described by Fig. 1(a). The reorientation divergence model also predicts a positive though weak divergence value matching this result [see Fig. 3(b) around $\phi = 35^\circ$, $\varphi_1 = 0^\circ$].

Fig. 6(c) shows the results for the Goss orientation. The grain has split into two different sharp orientation branches, related to each other by a rotation about the transverse direction $\langle 01\bar{1} \rangle$. As in the previous case a transition zone mediates between the orientation fragments. This result is in excellent accord with the prediction of the reorientation divergence model, which revealed a maximum divergence close to the Goss component [Fig. 3(a)].

Fig. 6(d) shows the results for the less symmetric orientation $\varphi_1 = 0^\circ$, $\phi = 18^\circ$, $\varphi_2 = 73^\circ$, which was chosen because it is known to be unstable and tends to rotate towards the α_{bcc} -fiber under plane strain conditions. It can be seen that the crystal, though building up minor orientation gradients, nearly rotates in one piece and does not split into different orientation branches with dissimilar orientation paths. This behavior corresponds to the case described by Fig. 1(b). The result is in excellent accord with the reorientation divergence model, which predicts a very small value for this component.

Fig. 6(e) shows the results for the RZ_{bcc} orientation, $\varphi_1 = 34^\circ$, $\phi = 84^\circ$, $\varphi_2 = 45^\circ$, which was chosen because it was identified as the absolute maximum in the reorientation divergence model (Fig. 3). The pole figure obtained by the crystal plasticity finite element simulation confirms a very strong tendency of the originally uniformly oriented grain to form orientation gradients. The pole figure shows a scattered array of orientation fragments after straining, which reveal accumulated orientation changes of up to 45° from their initial orientation prior to deformation.

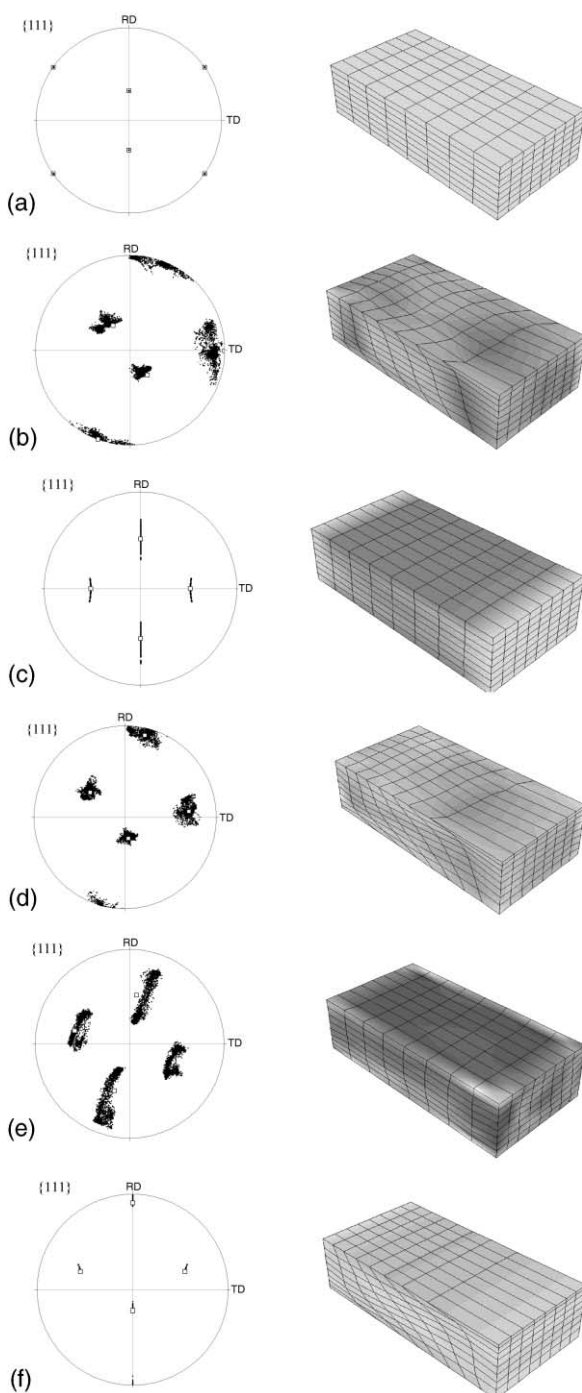
Fig. 6(f) shows the results for the rotated Goss orientation ($\langle 110 \rangle \langle 110 \rangle$, $\varphi_1 = 0^\circ$, $\phi = 90^\circ$, $\varphi_2 = 45^\circ$), which splits strongly during straining. This is in excellent accord with the reorientation field

divergence model, which shows a local maximum close to the rotated Goss orientation. Since the component is itself unstable under plane strain conditions, it rotates into this maximum and then starts to split up and form orientation gradients as predicted in the previous section.

3.3. Results for face centered cubic crystal structure (intrinsic, FEM)

Fig. 7(a) shows the accumulated misorientations in gray scale coding (using light values for large misorientations) for a fcc grain with initial Goss orientation after 50% reduction in thickness. The orientation distribution is given in the form of $\{111\}$ pole figures. The open squares show the initial orientation (which was the same at all integration points). The black dots show the orientations of all integration points after deformation. For the Goss orientation neither bulk rotation of the entire crystal nor in-grain orientation gradients have occurred during plastic straining. This behavior corresponds to Fig. 1(c). It is in very good accord with the reorientation divergence model using 12 slip systems (Fig. 4). The Goss orientation in fcc crystals with 12 slip systems is under plane strain conditions kinematically similar to the rotated cube orientation in bcc crystals with 48 slip systems [Fig. 6(a)]. The similarity is due to the 90° transverse rotation relationship which exists between the two texture components on the one hand and the 12 fcc $\{110\} \langle 111 \rangle$ slip systems and the 12 primary bcc $\{111\} \langle 110 \rangle$ slip systems on the other hand [61]. As will be discussed in the next section the stability of the bcc rotated cube orientation and of the fcc Goss orientation are influenced differently by grain neighbor interaction. It turns out that the fcc Goss orientation is strongly affected by neighbor grains.

Fig. 7(b) shows the results for the Brass component ($\langle 110 \rangle \langle 112 \rangle$, $\varphi_1 = 35^\circ$, $\phi = 45^\circ$, $\varphi_2 = 0^\circ$). It can be seen that the initially uniform grain has changed its overall orientation and at the same time built up strong orientation gradients inside its borders. The reorientation divergence model shown in Fig. 4 is in excellent accord with this observation since it predicts a pronounced positive divergence matching the finite element result (see Fig. 4



between $\varphi_1 = 30^\circ$ and 35° at $\phi = 45^\circ$ in the $\varphi_2 = 0^\circ$ section).

Fig. 7(c) shows the results for the 45° rotated cube orientation. It can be observed that the grain has formed pronounced orientation gradients resulting in two different orientation branches, related to each other by a $<011>$ crystal rotation axis parallel to the transverse direction. A transition zone preserving the original bulk orientation remains between the orientation fragments [11]. This result is in very good accord with the prediction of the reorientation divergence model, which showed a pronounced positive value of the divergence at the rotated cube orientation in the first section of Fig. 4.

Fig. 7(d) shows the result for the less symmetric S orientation ($\{123\}<6\bar{3}4>$, $\varphi_1 = 60^\circ$, $\phi = 32^\circ$, $\varphi_2 = 65^\circ$) which was already well investigated using crystal plasticity simulations by Beaudoin et al. [2]. It can be seen that the crystal, though undergoing substantial formation of orientation gradients, rotates as an entity and does not break up into completely different orientation branches with dissimilar orientation paths. This behavior corresponds to the case described by Fig. 1(b). The result corresponds very well to the reorientation divergence model which predicts a rather small value for this component.

Fig. 7(e) shows the results for the RZ_{fcc} orientation ($\varphi_1 = 32^\circ$, $\phi = 85^\circ$, $\varphi_2 = 85^\circ$), which was chosen because it was identified as the absolute maximum in the reorientation divergence model for an fcc material with 12 slip systems (Fig. 4). The pole figure obtained by the crystal plasticity finite element simulation indeed confirms a very strong tendency to build up strong orientation

Fig. 7. Accumulated misorientations in gray scale coding (light values indicate large misorientations) for a fcc grain (12 slip systems) after 50% plane strain deformation. The texture is given in the form of $\{111\}$ pole figures. The open square shows the initial orientation (which was the same at all integration points) and the black dots show the orientations after deformation. The starting orientations were (a) Goss orientation ($\varphi_1 = 0^\circ$, $\phi = 45^\circ$, $\varphi_2 = 0^\circ$); (b) Brass orientation ($\varphi_1 = 35^\circ$, $\phi = 45^\circ$, $\varphi_2 = 0^\circ$); (c) 45° rotated cube orientation ($\varphi_1 = 45^\circ$, $\phi = 0^\circ$, $\varphi_2 = 0^\circ$); (d) S orientation ($\varphi_1 = 60^\circ$, $\phi = 32^\circ$, $\varphi_2 = 65^\circ$); (e) RZ_{fcc} orientation ($\varphi_1 = 32^\circ$, $\phi = 85^\circ$, $\varphi_2 = 85^\circ$); (f) Copper orientation ($\varphi_1 = 90^\circ$, $\phi = 35^\circ$, $\varphi_2 = 45^\circ$).

gradients within the originally uniformly oriented grain. Some of the orientation fragments reveal accumulated orientation changes which are much larger than in all other investigated fcc crystals.

Fig. 7(f) shows the results for the Copper orientation ($\{112\} < 111 >$, $\varphi_1 = 90^\circ$, $\phi = 35^\circ$, $\varphi_2 = 45^\circ$) which forms only weak orientation gradients during straining. This is in good accord with the reorientation divergence model (Fig. 4).

4. Influence of neighbor grains on the tendency to form in-grain orientation gradients

4.1. Concept and calculation method

This section is concerned with the simulation of the influence of the plastic interaction between a grain and its neighbor grains on its tendency to form orientation gradients. This *extrinsic* effect on orientation gradients is investigated by exposing different bicrystal arrangements to external plane strain loading using the crystal plasticity finite element method sketched above. Boundary conditions were assigned to the free surface to constrain the entire assembly to an orthorhombic shape in the course of plastic straining (Fig. 8). Mesh configuration was carried out using ABAQUS/CAE [59]. The element number in the 3D model was 512 ($8 \times 8 \times 8$) elements with 64 of them ($4 \times 4 \times 4$) in the center part. A 3D solid linear element type with eight nodes and eight integration points was employed. An implicit procedure proposed by Kalidindi et al. [60] was used as constitutive crystal plasticity model. The scheme was implemented in the finite element program ABAQUS via the material subroutine UMAT [59].

Different crystal orientations, characterized by different reorientation rate and reorientation divergence, were assigned to the center and surrounding crystal, respectively. The compound was then exposed to 50% thickness reduction, like the single crystals discussed above.

4.2. Results for body centered cubic crystal structure (extrinsic, FEM)

Fig. 9(a) shows an example of a deformed bicrystal consisting of two grains with bcc crystal

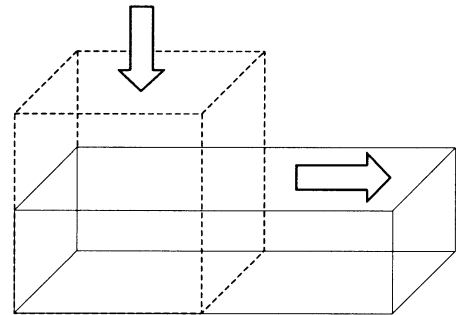
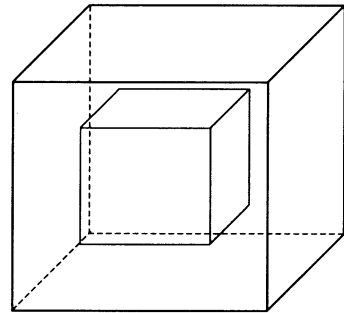


Fig. 8. The bicrystal set-up and displacement conditions used in the crystal plasticity finite element simulations. To simulate the influence of plastic neighbor interaction among the grains, i.e. the extrinsic component of grain fragmentation, different bicrystal arrangements were investigated under external plane strain loading. The free surface was constrained to preserve orthorhombic symmetry.

structure with $12 \times \{110\} < 111 >$, $12 \times \{112\} < 111 >$, and $24 \times \{123\} < 111 >$ slip systems. The center grain has Goss orientation, $\{011\} < 100 >$, and the surrounding grain has rotated cube orientation, $\{001\} < 110 >$. The gray scale quantifies the accumulated misorientation at each integration point (with light values indicating large misorientations). The figure shows that the two grains reveal very little interaction. The shape changes of both individual crystals follow the exerted plane strain deformation state. The texture changes in both individual crystals, given in $\{111\}$ pole figures [Fig. 9(a)], are similar to those observed already in the corresponding single crystals [Fig. 6(a,c)]. This homogeneous plastic co-deformation of both grains can be attributed to two points which are known from grain interaction

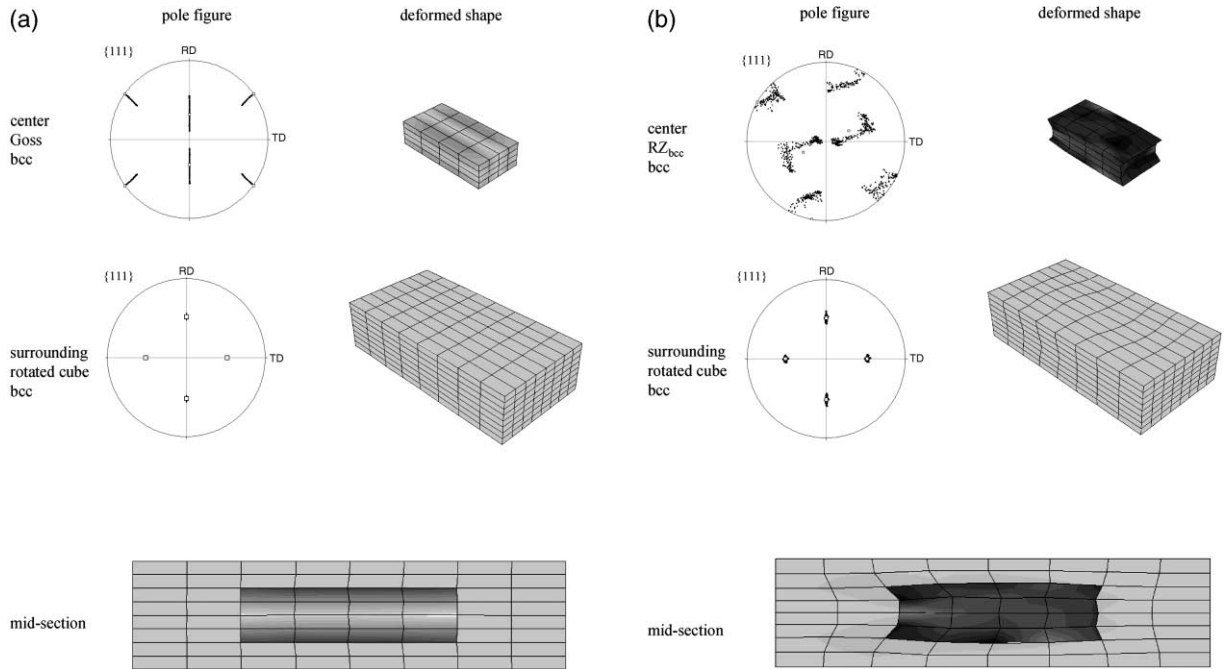


Fig. 9. (a) Example of a bcc bicrystal (48 slip systems), where the center grain has Goss orientation and the surrounding grain has 45° about normal rotated cube orientation. (b) Example of a bcc bicrystal (48 slip systems), where the center grain has RZ_{bcc} orientation and the surrounding grain has 45° about normal rotated cube orientation.

homogenization theory. First, both grains obviously have small shear tendency under plane strain deformation conditions. A grain is characterized by a large shear tendency when the required amount of shear on its slip systems (Taylor factor) can be lowered by dropping some of the external shape prescriptions at the cost of compatibility with the neighbor grains. Allowing for the partial relaxation of shear constraints means for orientations with large shear tendency that less slip is required for fulfilling the remaining non-relaxed constraints. Small shear tendency, as in Fig. 9(a), occurs when little or no deformation energy can be saved by dropping external constraints and shearing into a neighbor grain [57]. A second factor is that both grains reveal similar kinetic hardness, i.e. both individual crystals undergo nearly identical thickness reduction. It is an important fact that irrespective of the obvious strain and stress compatibility of the two grains the Goss crystal reveals the formation of strong orientation gradients.

Fig. 9(b) shows a different example of a bcc

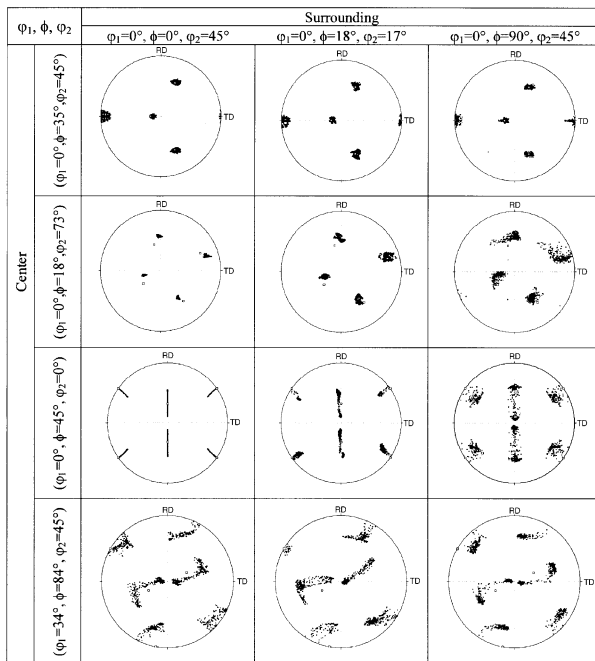
bicrystal. The center grain has RZ_{bcc} orientation and the surrounding grain has again {001}<110> orientation. In this case compatibility in shape change is not given among the two interacting crystals. The pole figures show that the interaction leads to a stronger orientation spread in the {001}<110> component when compared to the corresponding single crystal [Fig. 6(a,e)]. Table 1 summarizes some pole figures obtained from the bicrystal results for the bcc crystal structure. The data show the rotated cube ($\varphi_1 = 0^\circ$, $\phi = 0^\circ$, $\varphi_2 = 45^\circ$) component, an orientation close to the rolling texture fiber ($\varphi_1 = 0^\circ$, $\phi = 18^\circ$, $\varphi_2 = 17^\circ$), and the rotated Goss orientation ($\varphi_1 = 0^\circ$, $\phi = 90^\circ$, $\varphi_2 = 45^\circ$) as surrounding grains and the inverse Brass component ($\varphi_1 = 0^\circ$, $\phi = 35^\circ$, $\varphi_2 = 45^\circ$), another orientation close to the rolling texture fiber ($\varphi_1 = 0^\circ$, $\phi = 18^\circ$, $\varphi_2 = 73^\circ$), the Goss orientation ($\varphi_1 = 0^\circ$, $\phi = 45^\circ$, $\varphi_2 = 0^\circ$), and the RZ_{bcc} orientation ($\varphi_1 = 34^\circ$, $\phi = 84^\circ$, $\varphi_2 = 45^\circ$) as center grains.

The textures show the influence of neighbor

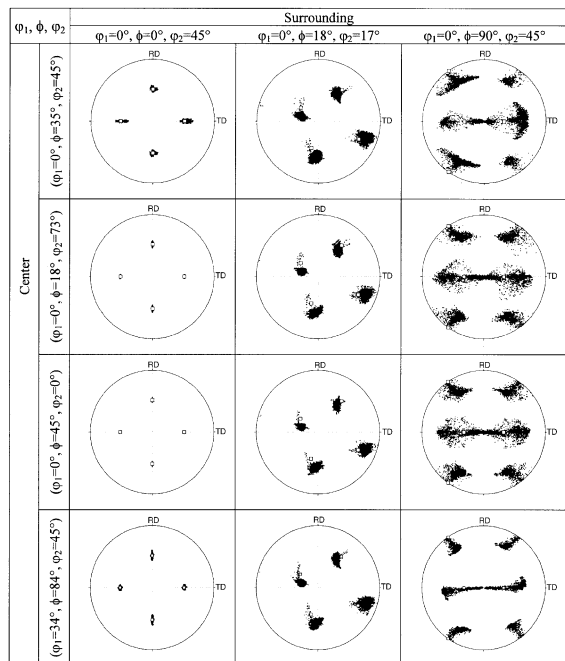
Table 1

(a) Some pole figures obtained from 3D bicrystal finite element results for bcc crystal structure. The textures show the influence of neighbor interaction on the resulting orientation gradients for different bicrystal combinations. This table shows the pole figures for the center grains (see Figs. 8 and 9). (b) Some pole figures obtained from bicrystal finite element results for bcc crystal structure. The textures show the influence of neighbor interaction on the resulting orientation gradients for different bicrystal combinations. This table shows the pole figures for the surrounding grains (see Figs. 8 and 9)

(a)



(b)



interaction on the resulting orientation gradients for different bicrystal combinations. Table 1(a) shows the pole figures for the center grains and Table 1(b) for the surrounding grains. Comparing these data with the pole figures given in Fig. 6 for the single grains⁵ suggests that a significant dependence of the tendency to form orientation gradients on the neighbor crystals occurs particularly for grains with high positive divergence. Examples are the RZ_{bcc} orientation and the Goss orientation. Both texture components revealed very high diver-

gence of their reorientation rate vector field [Fig. 3(a)]. The bicrystal finite element results confirm these predictions and show at the same time that their orientation spread depends considerably on changes in the neighbor orientations. The tendency to form orientation gradients within grains with close to zero or negative divergence reveals much smaller sensitivity to the orientation of the neighbor grain. For instance the Inverse Brass orientation [Table 1(a)] and the 45° rotated cube component [Table 1(b)] show less changes in the orientation spread when their neighbor grains are changed.

⁵ The single grains (Figs. 6 and 7) have a constrained surface to preserve orthorhombic symmetry during straining. They must not be confused with single crystals.

4.3. Results for face centered cubic crystal structure (extrinsic, FEM)

Fig. 10(a) shows an example of a deformed bicrystal consisting of two grains with fcc crystal structure using $12 \times \{111\} <110>$ slip systems. The center grain has RZ_{fcc} orientation and the surrounding grain has Goss orientation. The gray scale quantifies the accumulated misorientation at each integration point (light values indicate large misorientations). The figure shows that the two grains reveal very little plastic interaction, i.e. nearly no mutual distortion takes place and both individual crystals follow the external plane strain state. The texture changes in both individual crystals, given in $\{111\}$ pole figures [Fig. 10(a)], are similar to those observed in the single crystals [Fig. 7(a,d)]. In the bicrystal arrangement the Goss orientation reveals a larger scatter than as a single crystal. In contrast, the RZ_{fcc} oriented center grain in the bicrystal reveals weaker orientation gradients than as a single crystal. Like in the bcc case

this homogeneous co-deformation of the two grains can—when translated into homogenization theory—be understood in terms of their small shear tendency under plane strain deformation conditions and in terms of their similar Taylor factors.

Fig. 10(b) shows a different example of an fcc bicrystal. The center grain has Brass orientation and the surrounding grain has again Goss orientation. In this case the two interacting crystals do not preserve self-similar shapes as the couple in Fig. 10(a). Since the Goss orientation alone deforms symmetrically the strong shape distortion observed at the interface of the two grains can be attributed to the strong shear tendency of the Brass orientation. The two pole figures show that the interaction leads to a significantly stronger formation of orientation gradients in the Goss component when compared to the corresponding single crystal [Fig. 7(a)] and to the bicrystal in Fig. 10(a). In contrast, the orientation scatter in the deformed Brass orientation in the bicrystal is much smaller than in the corresponding single crystal [Fig. 7(b)].

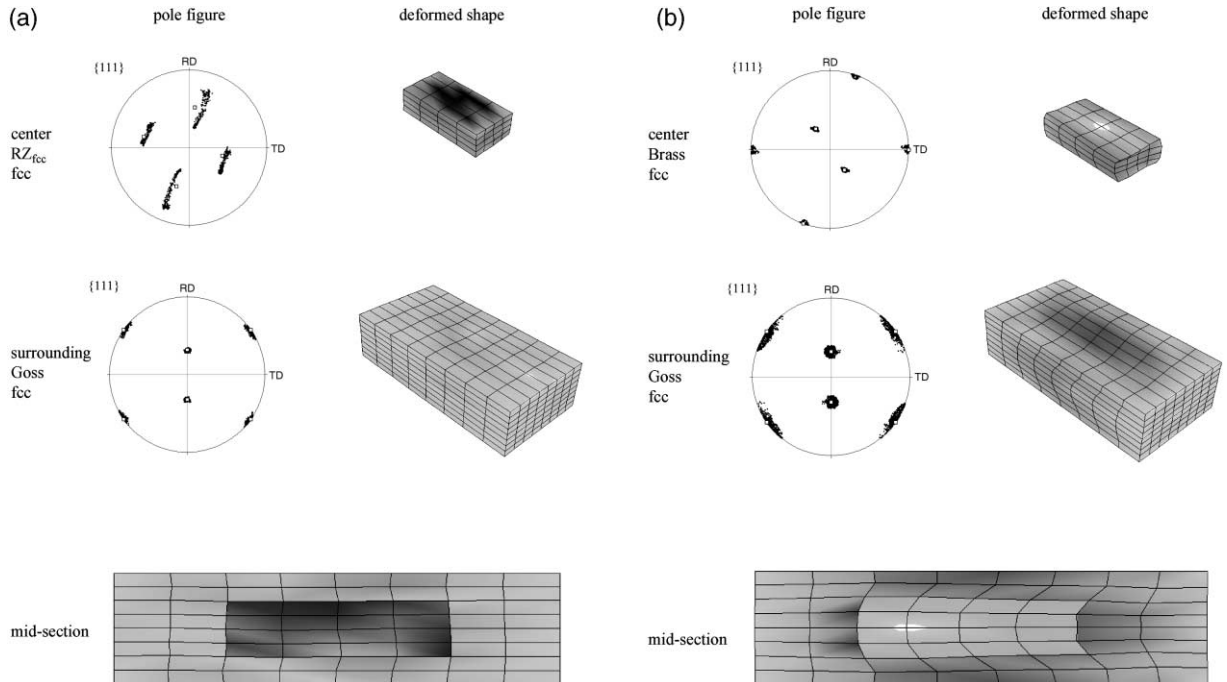


Fig. 10. (a) Example of an fcc bicrystal (12 slip systems), where the center grain has RZ_{fcc} orientation and the surrounding grain has Goss orientation. (b) Example of a bcc bicrystal (12 slip systems), where the center grain has Brass orientation and the surrounding grain has Goss orientation.

The simulations show that a bicrystal where one grain has a much larger intrinsic tendency to form orientation gradients than the other one tends to distribute the overall orientation scatter over both crystals rather than concentrating it in one crystal (namely in the one which tends to form larger orientation gradients in the intrinsic case).

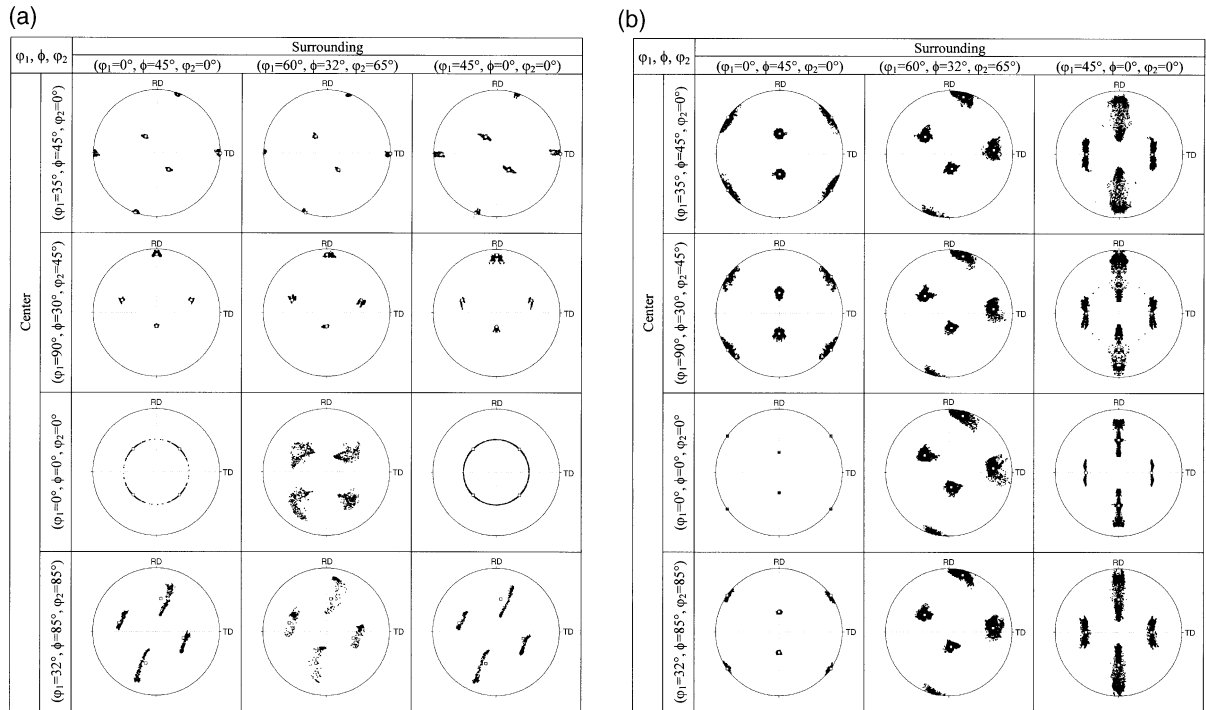
Beyond the examples given in Fig. 10(a,b) and Table 2 summarizes the pole figures of further fcc bicrystal arrangements. The data show the Goss orientation ($\varphi_1 = 0^\circ, \phi = 45^\circ, \varphi_2 = 0^\circ$), the S orientation ($\varphi_1 = 60^\circ, \phi = 32^\circ, \varphi_2 = 65^\circ$), and the rotated cube component ($\varphi_1 = 45^\circ, \phi = 0^\circ, \varphi_2 = 0^\circ$) as surrounding grains and the Brass component

($\varphi_1 = 35^\circ, \phi = 45^\circ, \varphi_2 = 0^\circ$), the Copper orientation ($\varphi_1 = 90^\circ, \phi = 30^\circ, \varphi_2 = 45^\circ$), the cube component ($\varphi_1 = 0^\circ, \phi = 0^\circ, \varphi_2 = 0^\circ$), and the RZ_{fcc} orientation ($\varphi_1 = 32^\circ, \phi = 85^\circ, \varphi_2 = 85^\circ$) as center grains.

The textures show the influence of neighbor interaction on the resulting orientation gradients for different bicrystal combinations. Table 2(a) shows the pole figures for the center grains and Table 2(b) for the surrounding grains. The data suggest that both, orientations with positive and also with close-to-zero divergence reveal a significant dependence of their tendency to form in-grain orientation gradients on the neighbor crystals.

Table 2

(a) Some pole figures obtained from 3D bicrystal finite element results for fcc crystal structure. The textures show the influence of neighbor interaction on the resulting orientation gradients for different bicrystal combinations. This table shows the pole figures for the center grains (see Figs. 8 and 10). (b) Some pole figures obtained from bicrystal finite element results for fcc crystal structure. The textures show the influence of neighbor interaction on the resulting orientation gradients for different bicrystal combinations. This table shows the pole figures for the surrounding grains (see Figs. 8 and 10)



This is a different result than obtained for the bcc crystal structure [see Table 1(a,b)] which revealed less neighborhood dependence for crystals with small reorientation divergence. For instance the fcc Goss orientation and the fcc cube orientation turn out to show a strong dependence on the orientation of the neighbor grains (Fig. 10).

5. Discussion

Some of the presented predictions can be compared to experimental observations of orientation gradients in different texture components and crystal structures deformed under plane strain conditions. In case of the bcc crystal structure particularly the 45° rotated cube component, $\{001\}<110>$, is well known for its small in-grain orientation gradients even after large plane strain deformation. Particularly the EBSP (electron back scatter diffraction) method has provided detailed data about orientation gradients in this texture component. Raabe et al. reported that the orientation scatter in $\{001\}<110>$ grains typically remains in the small angle grain boundary regime below 15° maximum in-grain misorientation (e.g. [3,30,31,33,58,62]). Similar observations for $\{001\}<110>$ grains in polycrystalline specimens were made by Dillamore et al. [63,64]. Earlier work on that subject was conducted by Hu on deformed $\{001\}<110>$ oriented iron–silicon single crystals [65,66]. Hu reported that $\{001\}<110>$ oriented single crystals do not change their initial orientation during rolling deformation and reveal a uniform microstructure without orientation gradients after straining. From a simple though sufficiently realistic Schmid-type analysis Hu concluded that the slip systems activated for the plane strain deformation of a $\{001\}<110>$ oriented grain are $(101)[111]$, $(101)[\bar{1}\bar{1}1]$, $(011)[\underline{1}\underline{1}1]$, $(011)[\bar{1}\bar{1}1]$. These systems have little mutual elastic interaction and it is assumed that such conditions also promote weak strain hardening. The various experimental observations about in-grain orientation gradients in the rotated cube orientation are in excellent agreement with the predictions [Fig. 3(a,b), 6(a), 9(a,b)]. Particularly Fig. 9(a,b) and Table 1(b) demonstrate that the reluctance of

this texture component against the formation of orientation gradients is not much affected by grain–neighbor interaction.

Apart from the rotated cube orientation which is in the bcc structure a good example for very weak orientation gradients stronger orientation scatter has been frequently found for $\{111\}<\text{uvw}>$ and $\{112\}<110>$ oriented grains (e.g. [30,31,33,58,67–72]). These studies reported that such grains reveal small cell sizes, high stored dislocation densities, and microstructural inhomogeneities such as shear bands which provide strong local misorientations. For the $\{111\}<\text{uvw}>$ grains the correspondence between experiment and predictions is less well pronounced. Fig. 3(b) shows local maxima of the reorientation field divergence not exactly on the $\{111\}<\text{uvw}>$ orientation fiber but in its immediate vicinity.

Another orientation which has been intensely investigated in the bcc structure is the Goss component, due to its importance in the fields of shear texture, recrystallization, and secondary recrystallization (e.g. [33,61,62,71,72]). It was essentially found that the Goss orientation is in the bcc lattice stabilized by shear strain. Under plane strain deformation it is not stable and splits up to rotate towards $\{001\}<110>$ and $\{111\}<112>$, respectively, building up strong orientation gradients. The remaining transition zones between such orientation branches can preserve the Goss orientation and for instance provide later highly potential nucleation sites. The strong tendency of the Goss orientation to form such in-grain orientation gradients was correctly predicted both, by the divergence approach [Fig. 3(a)] and by the finite element approach [Fig. 6(c)].

Similar arguments as for the rotated cube orientation in the bcc lattice apply for the Goss component in the fcc lattice. Under ideal plane strain conditions it can essentially be deformed by four symmetric slip systems. Its small tendency to build up orientation gradients is not only found in the reorientation field divergence approach (Fig. 4, first section) but also in the single crystal simulations [Fig. 7(a)]. However, the fcc Goss component significantly differs from the bcc rotated cube orientation with respect to its stability under the influence of neighbor grains. Comparing Tables

1(b) (bcc) and 2(b) (fcc) shows that the fcc Goss orientation builds up larger in-grain orientation gradients when co-deformed with the Brass or the Copper texture components than the bcc rotated cube component. This difference which is also well known from experiment can be attributed to the fact that (in this investigation) the fcc orientations deform by use of 12 slip systems while the bcc orientations use 48 systems. In other words the bcc crystals have more degrees of freedom in the displacement and hence deform more like a continuum when compared to the fcc crystals. Bcc crystals can therefore obviously better accommodate changes in the local boundary conditions. This might also explain why the rotated cube orientation is in cold rolled bcc alloys typically much more pronounced relative to the other texture components (see typical bcc α - and γ -fibers) than the Goss orientation in the textures of cold rolled fcc alloys (see typical bcc α - and β -fibers).

Besides the complicated fcc Goss orientation also other fcc texture components have been well investigated with respect to orientation gradients. For instance many experiments confirm the present predictions of a relatively small tendency to build up pronounced orientation gradients in the fcc Brass orientation. In contrast the cube orientation and the S orientation were reported to form larger orientation gradients (e.g. [5–7,22–27,41, 48,73,74]). However, the present results for the Goss and the cube orientation underline that their deformation and rotation paths are in experiments more governed by their neighborhood rather than by their (rather weak theoretical) intrinsic tendency to form gradients.

The prediction and experimental observation of orientation gradients is not only a problem of fundamental interest in the field of crystal kinematics but is also important in the context of hardening and recrystallization. Although the fields of texture and dislocation theory have not yet been fully merged since the first works of Nye [8], Kröner [9], and Ashby [10] in this domain the occurrence of orientation gradients clearly implies the generation of corresponding in-grain populations of geometrically necessary dislocations. These may contribute in a statistical, mechanically equilibrated and thus scalar manner or even in a tensorial

fashion to the overall hardening. In either context the present work suggests that in grains with a strong kinematical tendency to form in-grain orientation gradients the effect of geometrically necessary *hardening* should be taken into account. It can be anticipated that this will have a damping influence on the formation of orientation gradients since it provides a certain penalty term opposing further curvature. Vice versa this means that a theory of hardening—when considering geometrically necessary dislocations—must be formulated as an orientation dependent theory.

Similar arguments apply for the phenomenology of primary static recrystallization. It is a common observation that nucleation can only take place in areas with large stored elastic energy (thermodynamic instability criterion) and large orientation gradients (kinetic instability criterion). On the basis of the present approach the latter criterion implies that recrystallization nucleation must be considered as a highly orientation dependent problem (see e.g. [33]).

6. Conclusions

We introduced a theory of orientation gradients in plastically strained crystals. The aim was to explain why uniform crystals can—under gradient-free external loadings—build up in-grain orientation gradients during straining and how this phenomenon depends on the crystal orientation (intrinsic dependence) and on the neighbor grains (extrinsic dependence). The intrinsic origin of orientation gradients was explained in terms of the dependence of the crystal reorientation rate vector on variations in initial orientation. The dependence was quantitatively formulated by applying a divergence operator to reorientation rate vector fields calculated by strain-rate homogenization theory. The predictions were confirmed by crystal plasticity finite element simulations. The extrinsic influence on in-grain orientation gradients was addressed by investigating the effects of grain–neighbor interaction on the subdivision of crystals using a crystal plasticity finite element bicrystal model. The main conclusions are:

1. Orientation dependence of orientation gradients (intrinsic dependence)

The *divergence* of reorientation rate vector fields can be used to quantify the intrinsic tendency for the formation of in-grain orientation gradients as a function of crystal orientation and strain state. The divergence analysis method is independent on the underlying deformation model or experiment. Its starting point can be any theoretical or experimental reorientation field in orientation space. The method makes no prediction about the spatial arrangement of orientation gradients. Positive divergence indicates orientations with diverging non-zero reorientation rates which are unstable and form orientation gradients. Zero divergence indicates orientations with reorientation rate identity with the surrounding orientations which are not prone to form orientation gradients. Negative divergence indicates orientations with converging non-zero reorientation rates which are kinematically stable and not prone to form orientation gradients. Intrinsic results on orientation gradients obtained by use of a crystal plasticity finite element formulation are in very good agreement with the reorientation field divergence function derived by homogenization theory. The predictions are in good accord with experiments except for the fcc Goss and the fcc cube orientation which reveal a high dependence of grain neighbor interaction.

2. Grain neighborhood dependence of orientation gradients (extrinsic dependence)

Significant dependence of in-grain orientation gradients on the neighbor crystals (beyond their *intrinsic* tendency to form orientation gradients) was found in the bcc case for grains with high positive divergence and for the fcc case for grains with small and high positive divergence. The differences between bcc and fcc are due to the difference in slip selection (we used 12 systems for fcc and 48 for bcc). The formation of orientation gradients in crystals with close to zero or negative divergence depends less strongly on changes in the neighbor orientations. Exceptions occur

for the fcc case where the Goss and the cube orientation reveal a strong dependence on grain neighborhood.

References

- [1] Barrett CS, Levenson LH. Trans Metall Soc AIME 1940;137:112.
- [2] Beaudoin AJ, Mecking H, Kocks UF. Phil Mag A 1996;73:1503.
- [3] Raabe D. Phys Stat Sol (B) 1994;181:291.
- [4] Leffers T. Int J Plastic 2001;17:469.
- [5] Lee CS, Duggan DJ. Acta Metall 1993;41:2691.
- [6] Lee CS, Duggan DJ, Smallman RE. Acta Metall 1993;41:2265.
- [7] Ørsund R, Hjelen J, Nes E. Scripta Metall 1989;23:1193.
- [8] Nye JF. Acta Metall 1953;1:153.
- [9] Kröner E. Continuum theory of dislocations and internal stresses [in German]. New York: Springer Verlag, 1958.
- [10] Ashby MF. Phil Mag 1970;21:399.
- [11] Dillamore IL, Katoh H. Met Sci 1974;13:73.
- [12] Becker R, Panchanadeeswaran S. Acta Metall 1995;43:2701.
- [13] Becker R. Acta Mater 1998;46:1385.
- [14] Becker R, Butter JF, Hu H, Lalli L. Met Trans A 1991;22:45.
- [15] Becker R. Model Simul Mater Sci Eng 1995;3:417.
- [16] Mika DP, Dawson PR. Acta Mater 1999;47:1355.
- [17] Sarma GB, Dawson PR. Acta Mater 1937;1996:44.
- [18] Dawson PR, Boyce D, MacEwen S, Rogge R. In: Szpunar JA editor. Proceedings of the 12th International Conference on Textures of Materials ICOTOM 12, Aug. 9–13, 1999, vol. 1. Ottawa: NRC Research Press; 1999:505.
- [19] Raabe D, Becker R. Modelling Simul Mater Sci Eng 2000;8:445.
- [20] Buchheit TE, Bourcier RJ, Wellman GW, Neilsen MK. Model Simul Mater Sci Eng 1997;5:421.
- [21] Battaile CC, Buchheit TE, Holm EA, Wellman GW, Neilsen MK. In: Bulatov V, Diaz de la Rubia T, Ghoniem N, Kaxiras T, Phillips R, editors. Multiscale modeling of materials, MRS Symposium J, Boston, 1998.
- [22] Akef A, Driver JH. Mater Sci Eng A 1991;132:245.
- [23] Basson F, Driver JH. Acta Mater 2000;48:2101.
- [24] Hughes DA, Hansen N. Acta Mater 1997;45:3871.
- [25] Hjelen J, Weiland H, Butler J, Liu J, Hu WH, Nes E. Textures Microstruct 1991;14–18:983.
- [26] Hjelen J, Ørsund R, Nes E. Acta Metall 1991;39:1377.
- [27] Weiland H. Acta Metall 1992;40:1083.
- [28] Engler O, Gottstein G. Steel Res 1992;63:413.
- [29] Adams BL, Wright SI, Kunze K. Metall Trans A 1993;24:819.
- [30] Raabe D, Boeslau J. In: Andersen SI, Bilde-Sorensen JB, Lorentzen T, Pedersen OB, Sorensen NJ, editors. Proceedings of the 15th RISØ International Symposium on Materials Science: Numerical Predictions of Def. Proceed-

- ings and the Behaviour of Real Materials, Roskilde (Denmark): RISØ National Laboratory; 1994:481.
- [31] Boeslau J, Raabe D. Mater Sci Forum 1994;157–162:501.
- [32] Driver JH, Juul Jensen D, Hansen N. Acta Metall 1994;42:3105.
- [33] Raabe D. Steel Res 1995;66:222.
- [34] Bayer F, Fischer-Bühner J, Gottstein G. Intermetallics 1999;7:467.
- [35] Weiland H, Field DP, Adams DP. In: Liang Z, Zuo L, Chu Y, editors. Proceedings of the 11th International Conference on textures of materials, Xi'an (China). Beijing: International Academic Publishers; 1996. p. 141–4.
- [36] Liu Q, Maurice C, Driver JH, Hansen N. Metall Mater Trans A 1998;29:2333.
- [37] Weiland H. JOM 1994;46:37.
- [38] Weiland H, Becker R. In: Leffers T, Pederson OP, editors. Proceedings of the 20th RISØ International Symposium on Materials Science: Deformation-induced Microstructures: Analysis and Relation to Properties, Roskilde (Denmark): RISØ International Laboratory; 1999:213.
- [39] Krieger-Lassen NC, Jensen DJ. Mater Sci Forum 1993;113–115:679.
- [40] Schwarzer R, Weiland H. In: Proceedings of the 7th International Conference on Textures of Materials, Amsterdam (North Holland); 1984:839.
- [41] Hughes DA, Liu Q, Chrzan D, Hansen N. Acta Mater 1997;45:105.
- [42] Zaefferer S, Schwarzer R. Z Metallk 1994;85:585.
- [43] Zaefferer S. J Appl Cryst 2000;33:10.
- [44] Zaefferer S, Schwarzer R. Proceedings of the 10th International Conference on Textures of Materials. Mater Sci Forum 1994;157–162:247.
- [45] Zaefferer S. Proc Microsc Microanal 1999;99:202.
- [46] Field D, Weiland H. Mater Sci Forum 1994;157–162:1181.
- [47] Hughes DA. Proceedings 16th Int. RISØ Symposium on Materials Science, Roskilde (Dänemark), 1995, p. 63.
- [48] Hughes DA, Kumar A. In: Liang Z, Zuo L, Chu Y, editors. Proceedings of the 11th International Conference on textures of materials, Xi'an (China). Beijing: International Academic Publishers; 1996. p. 134–5.
- [49] Kocks UF, Embury JD, Cotton JD, Chen SR, Beaudoin AJ, Wright SI, Rollett AD. In: Advances in hot deformation textures and microstructures. Warrendale (PA): The Metallurgical Society of AIME; 1994:459.
- [50] Bunge HJ. In: Bunge HJ, Esling C, editors. Theoretical methods of texture analysis. Frankfurt: DGM Informationsgesellschaft, Deutsche Gesellschaft für Metallkunde, 1987, p. 407.
- [51] Klein H, Dahlem E, Esling C, Bunge HJ. In: Bunge HJ, Esling C, editors. Theoretical methods of texture analysis. Frankfurt: DGM Informationsgesellschaft, Deutsche Gesellschaft für Metallkunde, 1987, p. 259.
- [52] Seefeldt M, Delannay L, Peeters B, Aernoudt E, Van Houtte P. Acta Mater, in press.
- [53] Delannay L. Ph.D. dissertation, May 2001, Katholieke Universiteit Leuven, Belgium.
- [54] Roters F, Raabe D. In: Raabe D, Bunge HJ, editors. Proceedings of the Symposium Computer Simulation and Modelling in Texture Research, Aachen, October 13–14, 1995, Special Edition of Textures and Microstructures. London: Gordon and Breach; 1997:167.
- [55] Aernoudt E, van Houtte P, Leffers T. In: Mughrabi H editor. Deformation and textures of metals at large strains, materials science and technology—a comprehensive treatment, vol. 6. Weinheim: VCH; 1993:89.
- [56] Kocks UF, Tomé CN, Wenk H-R. Texture and anisotropy. Cambridge: Cambridge University Press, 1998.
- [57] Raabe D. Computational materials science. Weinheim: Wiley-VCH, 1998.
- [58] Raabe D, Schlenkert G, Weisshaupt H, Lücke K. Mater Sci Technol 1994;10:229.
- [59] ABAQUS/standard user's manual, vol. II, 14.1.4-1. Pawtucket (RI): Hibbit, Karlsson and Sorensen, 1999.
- [60] Kalidindi SR, Bronkhorst CA, Anand L. J Mech Phys Solids 1992;40:537.
- [61] Hölscher M, Raabe D, Lücke K. Acta Metall 1994;42:879.
- [62] Raabe D, Lücke K. Scripta Metall 1992;27:1533.
- [63] Dillamore IL, Morris PL, Smith CJE, Hutchinson WB. Proc R Soc A 1972;329:405.
- [64] Dillamore IL. In: Haessner F, editor. Recrystallization of metallic materials. Stuttgart: Dr Riederer Verlag GmbH; 1984:223.
- [65] Hu H. Trans AIME 1962;224:75.
- [66] Hu H. In: Himmel L, editor. Recovery and recrystallization of metals. New York: Wiley and Sons; 1963:311.
- [67] Dillamore IL, Smith CJE, Watson TW. Met Sci J 1967;1:49.
- [68] Hutchinson WB. Acta Metall 1989;37:1047.
- [69] Inokuti Y, Doherty R. Acta Metall 1978;26:61.
- [70] Ushioda K, Hutchinson WB, Agren J, von Schlippenbach U. Mater Sci Technol 1986;2:807.
- [71] Raabe D, Lücke K. Mater Sci Forum 1994;157–162:597.
- [72] Hölscher M, Raabe D, Lücke K. Steel Res 1991;62:567.
- [73] Wassermann G, Grewen J. Texturen metallischer Werkstoffe. Berlin: Springer Verlag, 1962.
- [74] Delannay L, Mishin OV, Juul Jensen D, Van Houtte P. Acta Mater 2001;49:2441.

Experimental investigation of plastic grain interaction

M. Sachtleber, Z. Zhao, D. Raabe *

Max-Planck-Institut für Eisenforschung, Max-Planck-Straße 1, D-40237 Düsseldorf, Germany

Received 20 June 2001; received in revised form 5 November 2001

Abstract

Aluminum polycrystals with columnar coarse grains are plastically compressed in a channel die. The spatial distribution of the accumulated plastic surface strains is determined by measuring the displacement fields using photogrammetry. For this purpose digital stereological image pairs of the sample surface are taken at the beginning and after each deformation step. The displacement field is derived from them by applying an image analysis method based on pattern recognition to the data before and after straining. The three components of the plastic displacement vector field are used to derive the surface portion of the plastic strain tensor field. The microtexture of the specimens is determined by the analysis of electron backscattering patterns obtained in a scanning electron microscope. The experiments are interpreted by comparing them to the corresponding crystal plasticity finite element simulations. © 2002 Elsevier Science B.V. All rights reserved.

Keywords: Grain interaction; Electron backscattering patterns; Texture; Strain heterogeneity; Strain mapping

1. Introduction

Deformed crystalline matter usually reveals a non-uniform distribution of the plastic strain. This can be attributed to the anisotropic nature of the crystal slip, to the non-isotropic interaction of the different lattice defects, and to the influence of macroscopic boundary conditions in terms of geometry and friction.

This article reports about a novel experimental approach for the investigation of such phenomena at the grain scale [1–7]. The technique is characterized by the joint application of photogrammetry and microtexture determination [1]. It aims at mapping both, mechanical and crystallographic changes during the plastic deformation of polycrystalline specimens. Photogrammetry is a method used in determining the spatial distribution of microstrains at the sample surface by measuring the changes in the three-dimensional plastic displacement field during a deformation experiment [1,8]. The technique employs a pattern recognition algorithm for the detection of changes in the gray scale distribution of surface patterns occurring during elastic–plastic strain-

ing. The microtexture of the specimens is determined by the analysis of electron backscattering patterns obtained in a scanning electron microscope.

The aim of this project is to understand better the plastic interaction of grains in polycrystalline specimens under loading. Scientific and technological spin-off from such investigations may be expected for the fields of microstructure mechanics of miniaturized crystalline devices; strain localization; failure; surface roughness mechanics; Taylor–Bishop–Hill type polycrystal homogenization theory; orientation dependence of nano-indentation; and phenomenological theories of nucleation for homo- and heterophase transformations in plastically strained crystalline matter.

2. Experimental

2.1. Basic procedure

The experiments aim at the determination of the accumulated non-uniform plastic strain field and the microtexture in the same sample. The data are taken between subsequent plastic deformation steps exerted in a plane strain channel die set-up.

Coarse-grained recrystallized polycrystalline aluminum samples of commercial purity (> 99.99 wt.%

* Corresponding author. Tel.: +49-211-6792-278; fax: +49-211-6792-333

E-mail address: raabe@mpie.de (D. Raabe).

Al) were used to prepare the specimens. A quasi-two-dimensional array of crystals with columnar morphology perpendicular to the transverse sample surface was prepared by heating samples into the grain growth and subsequent tertiary recrystallization regime. The final average grain size was about 3.5 mm. After annealing, each specimen was polished and finally etched. The sample shape was limited by the size of the chamber of the scanning electron microscope and by the 70° tilting angle required for obtaining Kikuchi backscatter diffraction patterns for the determination of the microtexture. Taking into account the elongation of the sample during plane strain deformation a maximum sample size of 17 mm × 10 mm and a thickness between 3 and 10 mm was chosen. These limitations in sample size were necessary to mount the elongated sample into the scanning microscope for microtexture analysis between the subsequent deformation steps.

Prior to the first deformation step, crystal orientation maps were taken at the sample surface. Orientation mapping is a technique for analyzing the topology of texture and grain boundaries in the crystalline material. Local lattice orientations are measured on a regular grid by the automated acquisition and processing of electron backscatter diffraction patterns in the scanning electron microscope. The microstructure can be reconstructed subsequently by coloring similar orientations on the measured grid with similar colors. In addition, the pattern quality of the Kikuchi patterns, which is a measure for the local perfection of the crystal lattice, is determined for each point. In the present investigation, the size of the measurement grid was chosen as a compromise between accuracy and measuring time. The grid step size was 100 µm which is well below the average grain size of 3500 µm.

Experiments were conducted after the determination of the starting texture using plane strain compression. For this purpose a servo-hydraulic mechanical testing machine equipped with a channel die set-up was used.

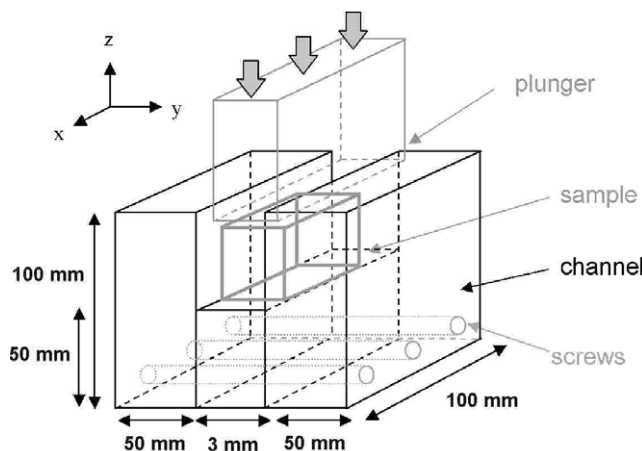


Fig. 1. Schematic drawing of the channel die plane strain set-up.

The tools were made from hardened steel and consisted of three parts that were bolted together during the test (Fig. 1). The rectangular samples matched the channel geometry exactly, which was open in the longitudinal direction. The sample was compressed by a punch device permitting its unconstrained elongation along the longitudinal direction. The channel walls prevented lateral expansion during compression, leading to a macroscopic plane strain state. Solid-state lubrication was obtained by placing a Teflon foil of 80 µm thickness around the sample. The Teflon also protected the gray scale pattern on the sample surface required for the photogrammetric determination of the displacement field. Experiments were carried out at a strain rate of $1.7 \times 10^{-5} \text{ s}^{-1}$ at room temperature. Plastic deformation proceeded in a series of subsequent steps each imposing a macroscopic engineering thickness reduction of about 3–5% per compression step.

Crystal orientation maps and digital image pairs of the sample surface were taken after each of the subsequent plane strain deformation steps. The images were used for the calculation of the three-dimensional plastic displacement fields employing photogrammetry. Details of the method are outlined in the ensuing section.

2.2. Determination of the plastic displacement and strain fields

The determination of the plastic displacement field and the subsequent calculation of some tensor components of the plastic strain field was after each deformation step conducted by a photogrammetric procedure. This is a digital image analysis method based on the recognition of geometrical changes in the gray scale distribution of surface patterns before and after straining [1,8]. Both, the natural characteristics of an unprepared sample surface or an artificial quasi-stochastic color spray applied to a polished surface (Fig. 2) may serve as an input pattern. In order to measure the three-dimensional surface coordinates digital stereo pair images of the sample were acquired using two high resolution CCD cameras as shown in Fig. 3.

Pattern recognition was carried out by a digital image processing procedure which maps a rectangular grid onto the image. The grid points are characterized by the three-dimensional coordinates and by the gray scale distribution in their proximity, Fig. 4. After straining, the pattern is again recognized based on the assumption that the gray scale distribution around a certain coordinate remains constant during straining. From the change in border coordinates containing the correct initial gray scale distribution around the grid point the three-dimensional displacement gradient tensor field is determined at each grid point. These data serve as input for deriving the surface components of the local strain tensor. The strain tensor is used in the

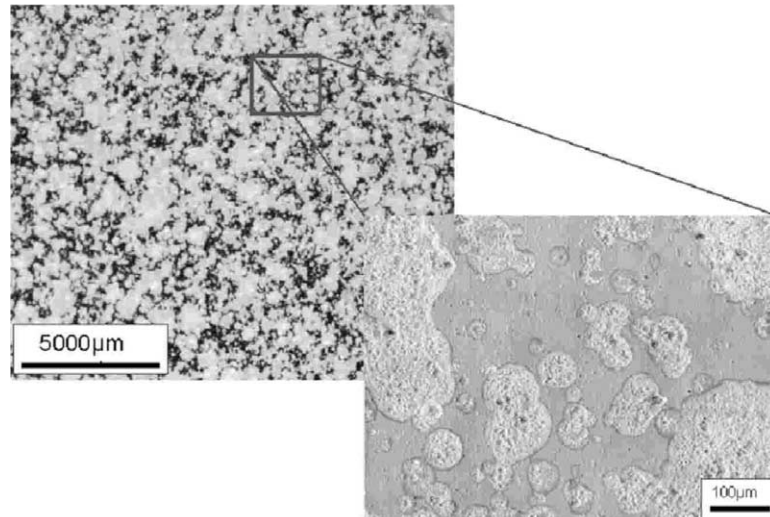


Fig. 2. Sprayed gray scale pattern on the surface of an undeformed polished and etched aluminum sample. The upper left picture was taken by digital optical microscopy. The lower right picture was taken in the scanning electron microscope. Images of this kind, taken before and after straining, were used for the photogrammetric calculation of the plastic displacement fields. For the spray, a color was chosen which did not affect the orientation measurement via electron backscattering diffraction.

definition as the first-order approximation of the standard polar decomposition of the displacement gradient tensor.

In this study, a fine white color spray was applied to the polished surface of the undeformed sample. The resulting gray scale pattern on the surface of the specimen was recorded and reference coordinates for the different experimental methods (microtexture, metallography, microstrain determination) were fixed on the sample surface. These surface markers allowed us to identify the same sample areas under the different experimental environments ensuring a one-to-one correspondence of the different results. The specimen was then plane strain compressed using the channel die set-up. After each deformation step the surface gray scale pattern was acquired and the displacement gradient field as well as the strain distribution were calculated.

It must be underlined in this context that the photogrammetric method works without any additional artificial regular grid on the sample surface. The displacement gradient field is derived exclusively from changes in the border coordinates for a gray scale distribution at each coordinate. The spatial resolution of the method is therefore independent of some external grid size but is of the order of the respective optical setup (12.5 μm in the present case). The strain resolution is below 1% since the method uses the match of the complete gray scale distribution before and after loading as a measure to determine the exact shift in border coordinates. This procedure provides a larger precision than the determination of the new border coordinates in the form of discrete pixel steps.

3. Results and discussion

Using the experimental procedures described above two sets of mappings were determined after each deformation step, namely, the microstrain distribution and the microtexture.

Fig. 5 shows the microtexture of the undeformed polycrystalline sample. The upper diagram shows the orientation angles with respect to the crystal direction normal to the compression plane. The lower diagram shows the angles with respect to the extension direction.

Fig. 6(a) shows the in-plane distribution of the accumulated shear at the sample surface after 3% thickness reduction along the compression direction. The shear is given in the reference system of the sample formed by the compression and longitudinal directions. The displacement fields were determined by use of the photogrammetric method explained in the preceding section. The grain structure determined experimentally (electron backscattering diffraction) is additionally mapped in the same diagram (Fig. 5). The superimposed lines indicate orientation changes above 15°. Fig. 6(b) shows the corresponding distribution of the accumulated von Mises strain together with the grain boundaries. The figures show that the grain scale deformation already is non-uniform at a very early stage of plastic straining. Pronounced localization of the strain is initiated at some of the triple points and along some of the grain boundaries.

This tendency to accommodate the imposed strain in a heterogeneous fashion becomes even more obvious after 8% sample thickness reduction. Fig. 7 reveals that some grains show much higher accumulated plastic strain than others. While some crystals carry as little as

1% von Mises strain within their borders (Fig. 7(b)), others show a maximum deformation above 16%, particularly close to the grain boundaries.

Some of the grains reveal a relatively homogeneous strain field inside their borders. This observation indi-

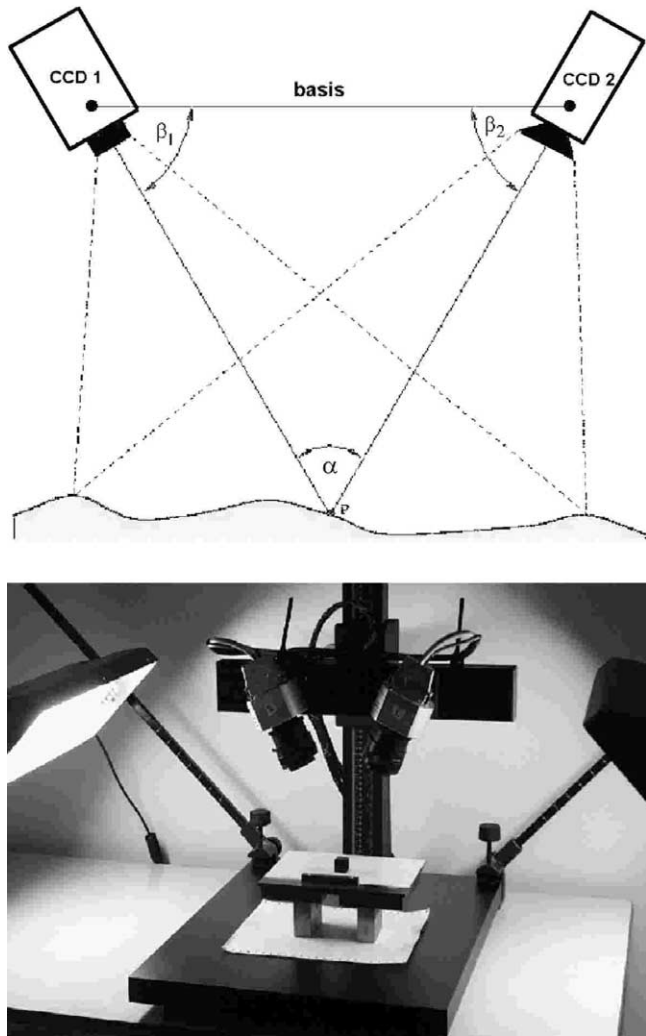


Fig. 3. Schematic drawing and photo of the experimental set-up of the CCD camera system.

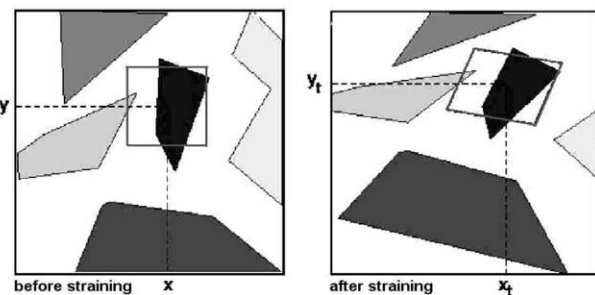


Fig. 4. Schematic drawing indicating the initial array (before straining) and the distorted array (after straining) containing a matching gray scale distribution.

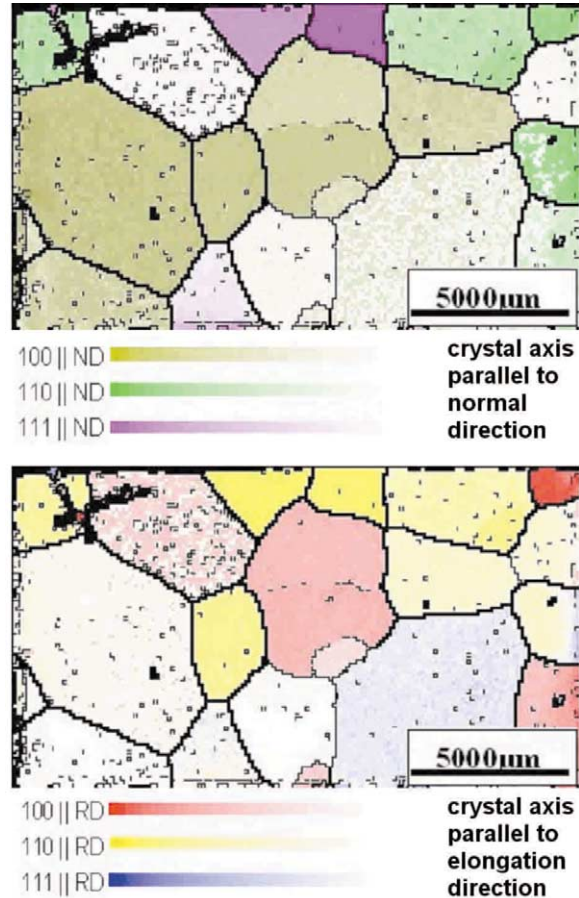


Fig. 5. Crystallographic microtexture of the sample before plastic deformation using separate color scales for the crystallographic axes parallel to the direction normal to the compression axis (ND) and parallel to the extension direction (RD). The grain boundaries with orientation changes above 15° were superimposed in Fig. 6.

cates that they respond as mechanical entities to the externally imposed load. Finding such homogeneous in-grain behavior is even more surprising if one considers that the non-zero friction conditions always entail macroscopic strain gradients within the specimen [9]. As will be discussed below in more detail by use of crystal plasticity simulations we attribute this mechanically uniform response of some grains to the dominance of their orientation factors for the overall percolation path of the strain. It must be noted though that the homogenization theory suggests smaller variations than the variations observed here in the strain distribution. The deviation between the standard Taylor–Bishop–Hill-type polycrystal homogenization theory and the present observations can be readily attributed to the large grain size encountered in the present work. This means that a small set of large grains cannot be theoretically investigated using the classical polycrystal models but must be treated using methods which more suited to treat the micromechanics of crystal clusters.

It is further remarkable that strain gradients between 2 and 16% occur within some of the grains. The strain maximum occurs in such cases in front of large angle grain boundaries the plane of which has an inclination close to 45° relative to the reference sample system. Other pairs of grains reveal practically no change in strain across their common grain boundary. This applies particularly for boundaries with relatively small misorientation (below 15°). Consequently, these grains seem to co-deform in a cluster-type fashion. However, due to the limited number of grains and grain boundaries involved in the present experiment it is not reasonable to draw general conclusions about the grain cluster mechanics at this stage.

Similar tendencies are found after 15% total sample thickness reduction (Fig. 8). The changes in the accumulated strains from grain to grain are even more pronounced than at a lower deformation. About half of the grains still behave as relatively homogenous mechanical units (Fig. 8(b)). This indicates that the grain scale strain hardening has not yet led to an equilibration of the flow stress in all parts of the specimen.

These continuing differences in grain hardness entail further amplification of grain-scale strain patterning. It is noteworthy that non-crystallographic strain localization effects do not dominate the appearance of strain heterogeneity in the sample. This observation underlines the strong importance of the initial crystal orientation distribution and the resulting profile in kinematic hardness for the overall strain heterogeneity.

Fig. 8(a) reveals another interesting detail, namely, the strong influence of the free surface on deformation. For instance, the large grain in the center of the sample (see arrows) is separated into two areas: one revealing the forward shear and the other the backward shear. This orientation of shear in the direction of the closest free surface leads to an additional source of strain heterogeneity.

Owing to the complexity of the experimental observations it is useful to inspect the situation under investigation by corresponding simulations. For this purpose, we used a crystal plasticity finite element method. This technique accounts for the discrete crystallographic nature of in-grain and grain-to-grain polycrystal kinemat-

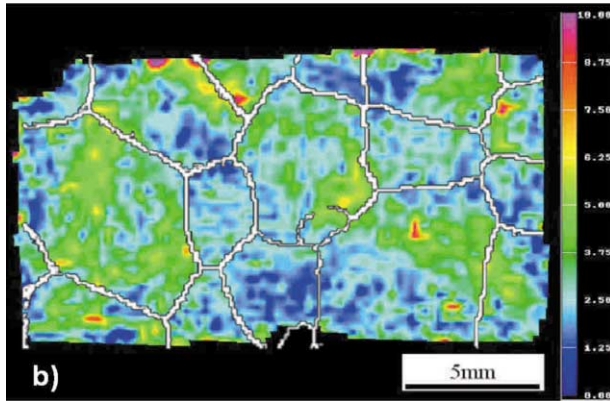
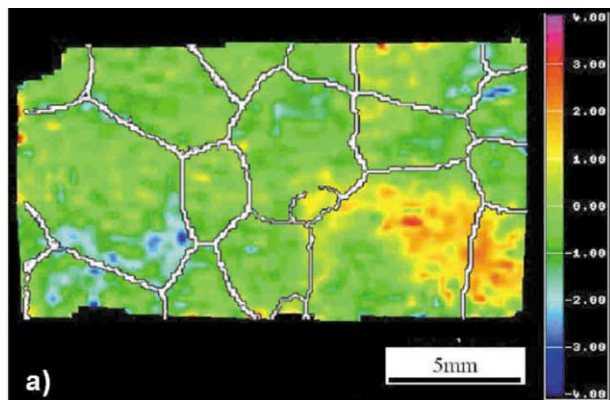


Fig. 6

Fig. 6. Distribution of the (a) accumulated engineering plastic shear and (b) von Mises strain in the specimen after 3% sample thickness reduction ($\Delta d/d$, where d is the sample extension along the compression direction). The strains were determined using photogrammetry. The grain boundaries indicated by white lines were taken from microtexture measurements.

Fig. 7. Distribution of the (a) accumulated engineering plastic shear and (b) von Mises strain in the specimen after 8% sample thickness reduction ($\Delta d/d$, where d is the sample extension along the compression direction). The strains were determined using photogrammetry. The grain boundaries indicated by white lines were taken from microtexture measurements.

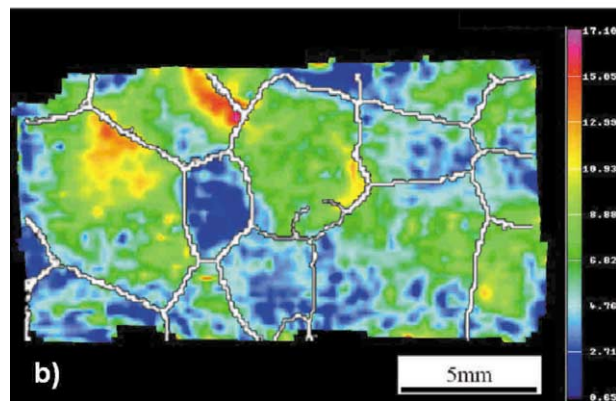
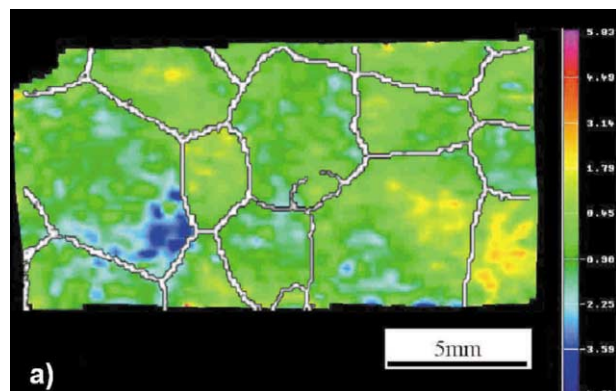


Fig. 7

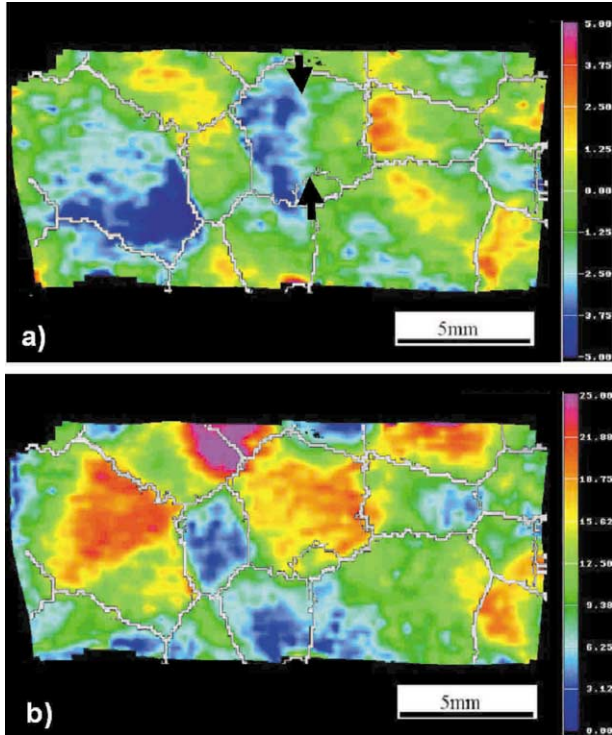


Fig. 8

Fig. 8. Distribution of the (a) accumulated engineering plastic shear and (b) von Mises strain in the specimen after 15% sample thickness reduction ($\Delta d/d$, where d is the sample extension along compression direction). The strains were determined using photogrammetry. The grain boundaries indicated by white lines were taken from microtexture measurements.

Fig. 9. (a) The microstructure of the initial sample was mapped onto a finite element mesh. Grid configuration was conducted along the grain boundaries using a bilinear element with four nodes and four integration points (5705 elements). (b) and (c) Accumulated von Mises strain as predicted from the crystal plasticity finite simulation for 3% (b), 8% (c), and 15% (d) sample thickness reduction. The finite element calculations were conducted using plane strain boundary conditions and a friction coefficient of $\mu = 0.2$. The constitutive crystal plasticity law was implemented using 12 $\{111\}\langle 110 \rangle$ slip systems and viscoplastic hardening. Finite element simulations were conducted using the finite element program ABAQUS in conjunction with the user defined material subroutine UMAT [14].

ics and allows one to conduct forming simulations with boundary conditions that approximate those of the real experiment.

For implementing crystal plasticity into a non-linear finite element scheme we used the fully implicit time-integration method suggested by Kalidindi et al. [10]. This model provides a direct means for updating the material state via integration of the evolution equations for the crystal lattice orientation and the critical resolved shear stress. The deformation behavior of the grains is at each integration point determined by a crystal plasticity model, which accounts for the plastic deformation by crystallographic slip and the rotation of the crystal lattice during deformation. The crystal kinematics follow those described by Asaro [11] and the rate-dependent formulation follows that developed by Peirce and co-workers [12,13]. In this concept of the

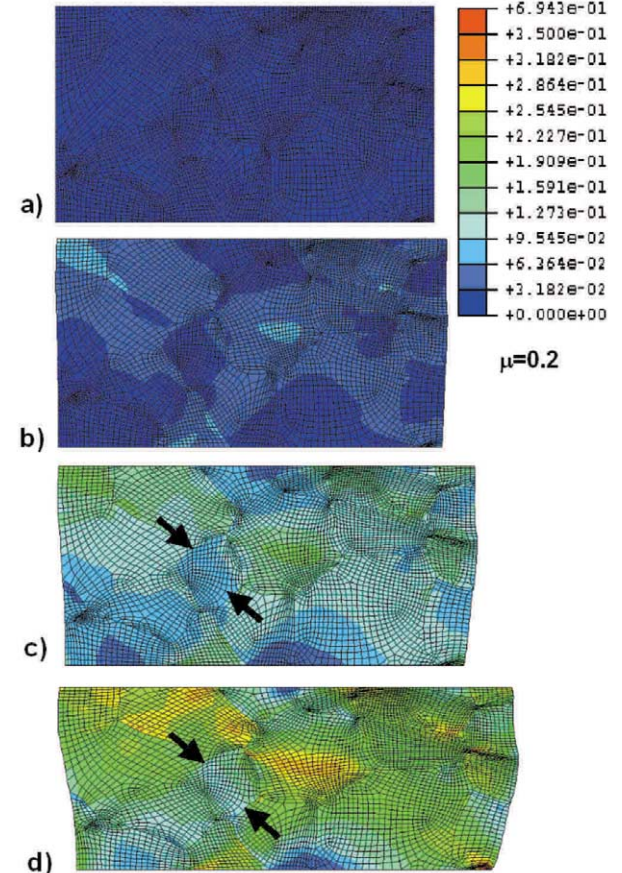


Fig. 9

constitutive description the slip rate on a slip system is assumed to be related to the resolved shear stress on this system through a power law relation which is equipped with a scalar scaling parameter for the stress as a phenomenological measure for the slip system strength or resistance to shear and a strain rate sensitivity exponent of 0.002. The value of the strain rate sensitivity exponent is low so that the material response is practically rate-independent.

With the slip rates given as an explicit function of the known resolved shear stresses, the rate-dependent method avoids the ambiguity in the selection of active slip systems which is encountered in many rate-independent formulations where it must be solved using an additional selection criterion. For the present simulations, the strengths of all the slip systems at a material point are taken to be equal, i.e. we adopt the Taylor

hardening assumption. The hardening as a function of accumulated slip is assumed to follow the macroscopic strain hardening behavior obtained from a mechanical test by fitting the experimental data to a Voce equation. The fit was adjusted by the average Taylor factor, using an approximate value of 3, to give the slip system resistance to shear as a function of the accumulated shear. When applied in a polycrystal simulation of a tensile test, this treatment of the slip system hardening will approximately reproduce the hardening behavior that was measured originally. The cubic elastic constants used in the simulation are typical for aluminum: $C_{11} = 108$ GPa, $C_{12} = 62$ GPa and $C_{44} = 28.3$ GPa. Further details on the simulations are given in [1].

The microstructure of the initial sample was mapped onto an appropriate finite element mesh, Fig. 9(a) [13]. Grid configuration was conducted along the grain boundaries employing a bilinear element with four nodes and four integration points using 5705 elements. The finite element calculations were conducted under external plane strain boundary conditions using a friction coefficient of $\mu = 0.2$. The constitutive crystal plasticity law was implemented with 12 $\{111\}\langle 110 \rangle$ slip systems. Finite element simulations were conducted using the finite element program ABAQUS in conjunction with the user defined material subroutine UMAT [14].

Fig. 9(b)–(d) show the accumulated von Mises strain as predicted from the crystal plasticity finite simulation for 3, 8, and 15% sample thickness reduction. The simulations show a very heterogeneous distribution of strain, similar to as observed experimentally. In some areas, they show a strain pattern that reproduces the topology given by the large angle grain boundaries. This is in accord with the experimental observations (e.g. for 8% thickness reduction see Figs. 6(b) and 9(c)). Pronounced strain localization occurs along the upper left and lower right parts of the deformed shape diagonals as well as within the center grains (e.g. Fig. 9(c)). Areas with small plastic strain can be found in the vicinity of the middle of the top and bottom edges. Some grains reveal very small overall strains within their borders (see arrows in Fig. 9(c) and (d)).

The simulations reveal a good agreement with the experiments. Deviations can be attributed essentially to the friction conditions and their change during forming (the simulations assumed constant friction conditions). The major correspondence of the simulations and the experiments is that grain scale heterogeneity is mainly determined by two factors. First, by the external friction conditions and second, by the orientation factors that occur and their influence on strain accommodation.

4. Conclusions

The paper presented a novel experimental approach for the investigation of grain-scale strain heterogeneity during plastic deformation. The main results are as follows: Quantitative experimental grain- and sub-grain scale strain analysis can be conducted using photogrammetry in conjunction with microtexture experimentation. Strain patterning in aluminum during plane strain compression is strongly determined by the orientation dependence of the kinematic hardness of the individual grains. This effect was interpreted in terms of the respective orientation factors. Two forms of grain deformation were observed. The first kind was characterized by the individual and homogeneous deformation of single grains at individual strain levels (corresponding to their orientation factors) which were significantly different from those of their neighboring grains. The second kind was characterized by the co- or cluster-type deformation of areas comprising more than one grain, revealing a common fairly homogeneous strain level. At sample thickness reductions up to 3% strain localization was in some cases initiated at grain triple points (the specimen had a quasi-2D columnar grain structure) and along some grain boundaries which had an angle close to 45° with respect to the sample coordinates. The experimental results were in good accord with the corresponding crystal plasticity finite element simulations.

References

- [1] D. Raabe, M. Sachtleber, Z. Zhao, F. Roters, S. Zaefferer, *Acta Mater.* 49 (2001) 3433.
- [2] F. Delaire, J.L. Raphanel, C. Rey, *Acta Mater.* 48 (2000) 1075.
- [3] C. Lineau, C. Rey, P. Viaris, *Mater. Sci. Eng.* A234–236 (1997) 853.
- [4] S.V. Harren, R.J. Asaro, *J. Mech. Phys. Solids* 37 (1989) 191.
- [5] A.J. Beaudoin, H. Mecking, U.F. Kocks, *Philos. Mag.* A73 (1996) 1503.
- [6] R.C. Becker, S. Panchanadeeswaran, *Acta Metall.* 43 (1995) 2701.
- [7] K.K. Mathur, P.R. Dawson, *Int. J. Plast.* 8 (1998) 67.
- [8] Handbook for the Aramis System by GOM mbh, Gesellschaft für Optische Meßtechnik, Version September 2000, Braunschweig, Germany.
- [9] D. Raabe, Z. Zhao, S.-J. Park, F. Roters, *Acta Mater.* 50 (2002) 421.
- [10] S.R. Kalidindi, C.A. Bronkhorst, L. Anand, *J. Mech. Phys. Solids* 40 (1992) 537.
- [11] R.J. Asaro, *Adv. Appl. Mech.* 23 (1983) 1.
- [12] D. Peirce, R.J. Asaro, A. Needleman, *Acta Metall.* 31 (1983) 1951.
- [13] H. Weiland, R.C. Becker, in: T. Leffers, O.P. Pederson (Eds.), *Proceedings of the 20th RISØ International Symposium on Materials Science*, RISØ National Laboratory, Roskilde, Denmark, 1999, p. 213.
- [14] ABAQUS/Standard User's Manual, vol. II, 14.1.4-1, Hibbitt, Karlsson and Sorensen, Pawtucket, RI, USA, 1999.